Order Number 9108124

Electrochemical morphogenesis of zinc and silver metals

Kahanda, Galathara Lekamge Mahendra Kumara Samarakone, Ph.D.

City University of New York, 1990

U·M·I
300 N. Zeeb Rd.
Ann Arbor, MI 48106

Electrochemical Morphogenesis of Zinc and Silver metals

by

Galathara Lekamge Mahendra Kumara Samarakone Kahanda

A dissertation submitted to the Graduate faculty in Physics in partial fulfillment of the requirements for the degree of Doctor of Philosophy, The City University of New York.

1990

This manuscript has been read and accepted for the Graduate Faculty in Physics in satisfaction of the dissertation requirement for the degree of Doctor of Philosophy.

9/14/90
Date

Micha Tomkiewicz
Chair of Examining Committee

9/17/90
Date

Joseph B. Krieger
Executive Officer.

Pedro A. Montano

George Skorinko

Herman Z. Cummins

Michael Kramer
Supervisory Committee

The City University of New York

Abstract

Electrochemical Morphogenesis of Zinc and Silver metals

by

Galathara Lekamge Mahendra Kumara Samarakone Kahanda

Advisor: Professor Micha Tomkiewicz

The morphological evolution of zinc and silver metals in a pseudo two dimensional, thin layer, three electrode electrochemical cell was studied. Detailed growth patterns were obtained with varying applied potential and the concentration of the active and supporting electrolytes. We found a correlation between the kinetics of the deposition and the fractal dimension of the deposit. The general trend of the growth structures is similar for all the systems as the potential varies from the activation to the mass transfer limited region. Near the activation region, deposits resemble the mossy type structures while in the mass transfer limit it follows the DLA type growth, depending upon the active electrolyte concentration and diffusion-migration ratio. The frequency dispersions of the impedance of smooth and the ramified silver deposits, in their oxidized and unoxidized state, were measured. We sought to correlate the constant phase angle exponent (CPA) with surface fractal dimension of the deposits and compare the results with present theories. A monotonic relation between the two parameters was found. The functional relationship is insensitive to the dielectric properties of the interface.

This thesis is dedicated

in memory of my father

and

to my mother

for their life long devotion to education

and

to my late sister

who deserved this more than me.

Acknowledgements

I would like to express my gratitude to my advisor professor Micha Tomkiewicz for choosing me to pursue this work and his guidance and encouragement during the course of this study. I wish to thank my committee members, Professors: Pedro Montano, George Skorinko, Herman Cummins and Dr. Michael Kramer for their help and suggestion for this work. I also wish to thank to Dr. Pabitra Sen for giving me his invaluable support and encouragement at the right time for the right place without hesitating. I thank Dr. Jim Kauffman for his collaboration and suggestion on drift diffusion simulation and Dr. Bernard Sapoval for the important comment on the impedance work. I thank Dr. Marcia Fantini for her constant support, discussion and useful ideas throughout her stay at our department. I thank my fellow graduate student Wu-Mian Shen for his support from the beginning of this study and the interesting discussion on failing communism all over the world. The kind concern of Montford Naylor on my works and sharing his memories and experience of the second world war with us is specially remembered. I would also like to thank Liane Fu at the college writing center for her patient and kind concern on reading and correcting of the thesis. All the teachers who taught me science as well as non science subjects, especially Professor Kirthi Tennakone, Ruhuna University, Sri Lanka who gave me the initial thrust to come to the US for this study be remembered.

I would like to devote this work to my father, for his fifty one years, and my mother for her thirty seven years, of their life long devotion to

education as teachers. They have shown me the greatness of being a teacher. I appreciate my mothers strength and dedication in holding the family and our dreams together, especially after my fathers death. All my brothers and sisters are gratefully remembered. Without their moral support, advice and encouragement, this would not have been possible. I especially appreciate the sacrifice of my elder brother Srikantha, who gave up his higher studies at the death of our father. I gratefully remember my talented late sister Lalana, who we had hoped would one day pursue a career in higher education.

I wish to acknowledge with gratitude the department of Physics of Brooklyn college for providing me this opportunity and the United States office of Naval Research for the financial support during the course of this work.

Finally, I am grateful to my wife Chandrakanthi, for her constant support and love, not only through this study but also through our undergraduate studies, and my elder son Rahal Yugantha, who helped me to count the number of trees and suggest that I join the Forest department after this study and lastly the new addition to our family Milan Gimantha, who will one day understand the reasons for having less; attention, kissing and hugging during the period of this writing.

G. L. M. K. S. Kahanda

Brooklyn, New York

September 1990

Table of Contents.

List of Tables.

List of Figures:

1. Introduction.

The purpose of this work is to develop a better understanding of the pattern formation in an electrochemical system and possibly to narrow the gap between the recent advances in morphogenesis and the century old, mostly empirical, science of electrochemistry. The stochastic morphology was studied experimentally, using time-lapse microscopy for a quantitative evaluation of the time evolution of the deposits and with impedance measurement over a broad frequency range for the evaluation of electrical transport properties.

Recent interest in growth and aggregation phenomena that results in fractal clusters[1] with power-law correlations over the extended range of length scales was triggered by the success of relatively simple computer simulations of diffusion-limited aggregation (DLA) introduced by Witten and Sander[2,3]. It was shown that the methodology of DLA simulation and the resulting scale invariant properties can be extended to apparently unrelated phenomena such as dielectric breakdown[4] and viscous fingers[5] through pattern formation in various fields that satisfy Laplace equation.

The electrodeposition of metals from electrolytes poses many interesting problems in the field of pattern formation, especially as the morphology of the deposits obtained appears to depend dramatically upon the precise conditions of the deposition. Following the success of the DLA simulations, and the fractal concept of the irregular geometries, the electrochemical electrodeposition showed up as one of the best experimental testing grounds for the field of nonequilibrium growth and aggregation, since it gives the experimentalist a direct

control over the kinetics of the competition between the stochastic (diffusion) and the deterministic (activation) processes.

However, the dendritic and similar growth patterns in the electrochemical system[6] has been known for many years and has important technological ramifications in the performance of electrochemical power conversion devices such as batteries. In the period of 1954 to 1955, Wranglen[7] studied the electrochemical deposition of Silver, Cadmium and Lead, shown in figure 1.1. The morphology of these structures shows a remarkable similarity to the recently observed noise reduced DLA[8] patterns. These were the first observations of DLA type patterns. Although, these observations were very impressive at that time, without proper tools (Fractal, DLA etc.) and techniques (image analyzer, PC's etc.), the in-depth analysis of the morphology was left unfinished.

Shortly after computer simulation work started to appear, experimental work on pattern formation in electrodeposition of Copper[9], Zinc[10] and conducting organic polymers[11] electrodes followed. Attempts were also made to change the patterns by varying electrochemical parameters such as voltage and the concentration of active material[12-14] with attempts at establishing a nomenclature for patterns such as dendritic, string-like, open split, mossy etc. A general description of these experimental works could be found in section 2.4.

Voss and Tomkiewicz[15,16] introduced the multiparticle diffusion limited deposition (MPDLD) model, as a generalization to the single particle DLA process to describe the diffusion limited electrodeposition. By introducing the concept of sticking probability, they were able to generate mossy to dendritic structures, similar to those expected in real electrodeposition. Construction of our deposition cell is based on the

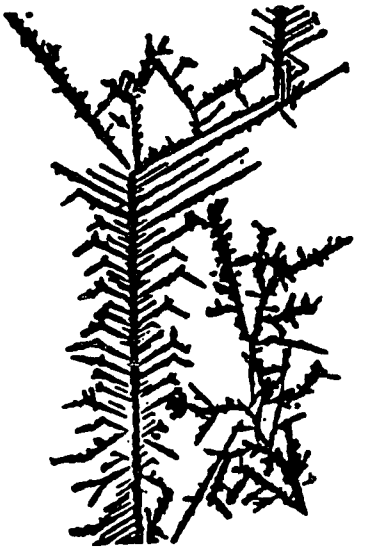

(a)

(b)

Figure 1.1: (a). Two dimensional Silver dendrite with three dimensional dendrite on right.[Wranglen:8]
(b). Three dimensional dendrite of Cadmium.[8]

MPDLD model, so that one could compare the experimental and simulated observations.

It is important to note that as the fractal dimension emerges to take a prominent place in the field of growth and aggregation, theoretical [17-20] and experimental [21,22] attempts to correlate the irregular morphologies (as characterized through their scaling properties by using fractal geometry) with the impedance of their interface with an electrolyte produces some degree of confusion and disagreement. Most of the work was based on an "ideally polarizable" or blocking interface in which the purely capacitive interface linearly scales with the surface area and thus offers the correlation between the impedance and the fractal geometry.

We will focus our studies on Zinc and Silver metals because of their importance as electrode materials for rechargeable batteries [26] and advanced energy storage [27] devices. Problems that limit the commercial application such as: short cycle life associated with the growth of nodules and dendrites, formation of non adherent mossy deposits [26-30] during the charging and the electrode shape (morphology) change [27,30] with cycling, are directly related to the proposed study.

2. Background.

2.1. Simulation Models for Electrochemical Deposition.

A very simple model for cellular growth has been proposed by Eden in 1961[31]. It was mainly introduced to explain the evolution of tumors. But this model has been invoked in many other physical situations and, even if it does not lead to fractal structures it is now considered as a fundamental basic model for aggregation.

In its simplest version, this model builds a connected cluster on a lattice, i.e. particles can only be placed on the sites of a periodical lattice in d-dimension and two particles are connected if they occupy nearest-neighbor sites on the lattice. The aggregation mechanism follows an iterative rule in which, starting from a seed particle at the origin, particles are added one after another to the aggregate.

This process produces a relatively compact cluster whose density correlations are independent of distance in the limit of large size. By contrast the smoke-particle aggregates, which were studied by Forrest and Witten[32], reported to have correlations which fall off as a fractional power of distance. Thus, they resemble random walks, percolating clusters and other density profiles associated with critical phenomena. Motivated by these experimental observations Witten and Sander[2] introduced a simple kinetic model of diffusion limited aggregation (DLA), which is a variant of the Eden model. This model has been the subject of a great amount of either analytical, numerical or experimental investigations.

The DLA model is more general than expected, has been used to described processes which apparently have nothing to do with

aggregation. The spirit of this generalization is as follows:

Let us define in the DLA model, the probability **u**, of finding a diffusing particle at some point before it reaches the aggregate. In steady state (over a long time), the mean flux of the incoming particles is proportional to the gradient of **u**, and, since particles are only absorbed at the surface of the aggregate, this flux has no divergence, i.e. **u** obeys the Laplace equation,

$$\nabla^2 \mathbf{u} = 0 \tag{2.1}$$

with limiting condition **u** = 0 on the aggregate and **u** = constant far from the aggregate, where the particles are released. Thus, in the DLA model, the growing rate is controlled by a "field" which is derived from a given "potential", whose Laplacian is zero.

2.1.1 Diffusion Limited Aggregation Model (DLA).

We shall described here the DLA model in its original version on a two dimensional lattice: Let us consider a simple square lattice on a plane, as shown in Figure 2.1. One first chooses a particular site, O, on which one places a particle, which will be the seed of our aggregate. Then one consider a large circle of radius R, centered on the seed site. The first particle is released from the randomly selected perimeter site; the particle jumps from one site to any of the nearest neighboring sites, the new position being chosen at random among the four possibilities. If during its random walk, the particle reaches a site nearest neighbor to the seed site, it stops and stays stuck to the seed, then another (second) particle starts a random walk from randomly selected perimeter site, whose motion is stops, when it comes to nearest neighbor site to seed particle or the other particle on the aggregate. If a random walker

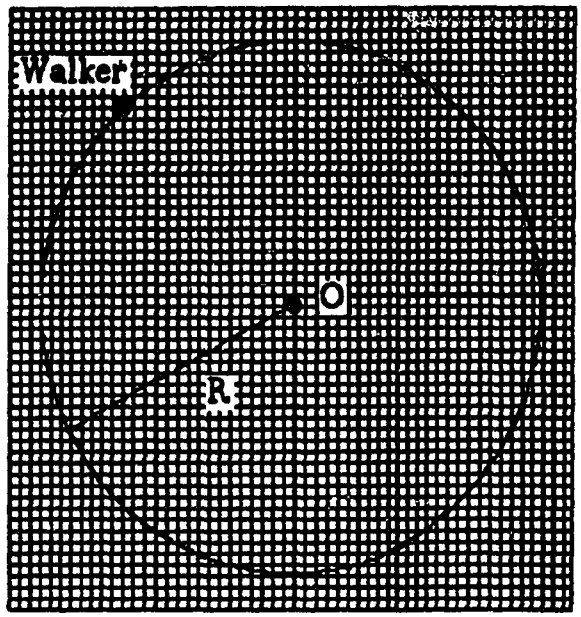

(a)

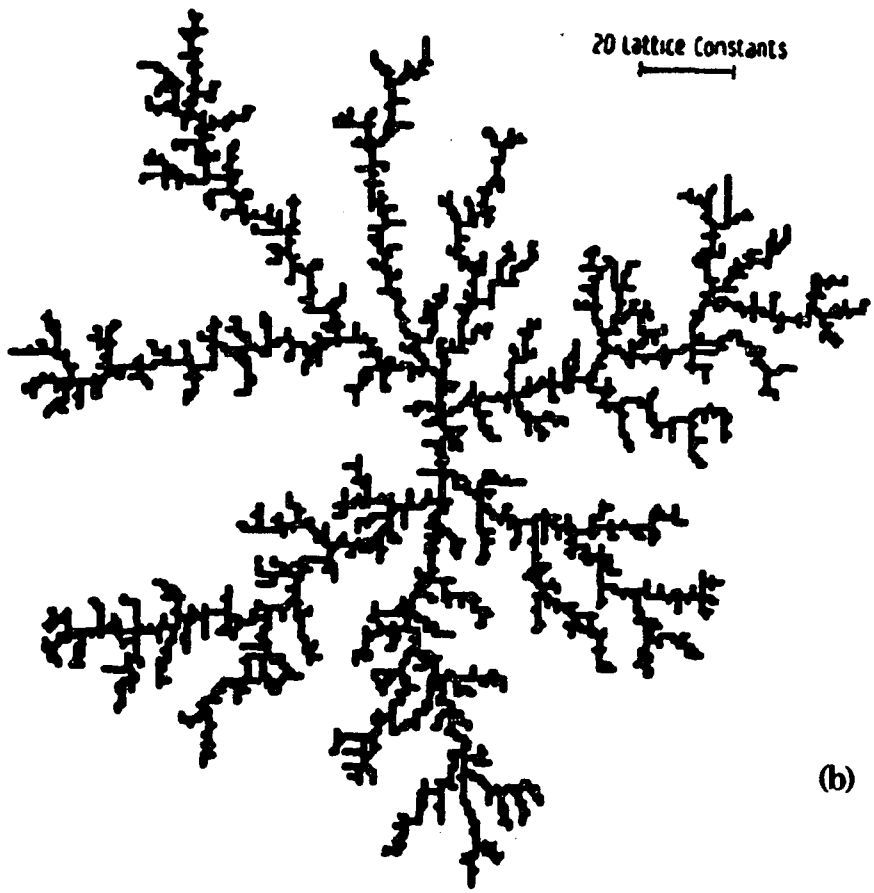

(b)

Figure 2.1: (a) Two dimensional lattice for DLA process. (b) Aggregate of 3600 particles.

diffuses too far from the aggregate, it will be discarded and then another particle will be released from the perimeter of the circle. In practice, to reduce the computer time, the distance allowed to walk away from the seed site for any walker is limited to three times the radius of the large circle. This procedure is iterated until one reaches the desired number of particles. A typical DLA aggregate containing 3600 particles[2] is shown in Figure 2.1.

2.1.2 Multiparticle Diffusion Limited Deposition Model (MPDLD).

The simulation is carried out on a two dimensional square lattice (LxL), where a fraction **f**, of the sites are initially occupied with mobile particles. The bottom edge (h=0), is the initial active area for growth while the top edge (h=L) is held at fixed concentration (see Figure 2.2). The mobile particles undergo simultaneous diffusion under the constraint that no two particles can occupy the same site at the same time. During a time step, each of the mobile particles is examined in random order. One of its four neighbor sites is selected by chance as a possible next position. If unoccupied, the particle moves to this new site. If occupied, the particle remains fixed. Periodic boundary conditions are used in the the horizontal direction, i.e. particles that leave to the right enter from the left and vice versa. If the new site borders a growth site, it becomes a part of the aggregate with a sticking probability, **s**. Once part of the aggregate, the particle is immobile and is itself a new growth site. The procedure is repeated until an either fixed number of particles have aggregated or until a fixed number of time steps have elapsed.

One can study the variation of the morphology with different **s** and **f**. Figure 2.2 shows an example of **f** = 0.05 for different values of **s**. In an electrochemical deposition under constant potential, **s** mimics the

(a)

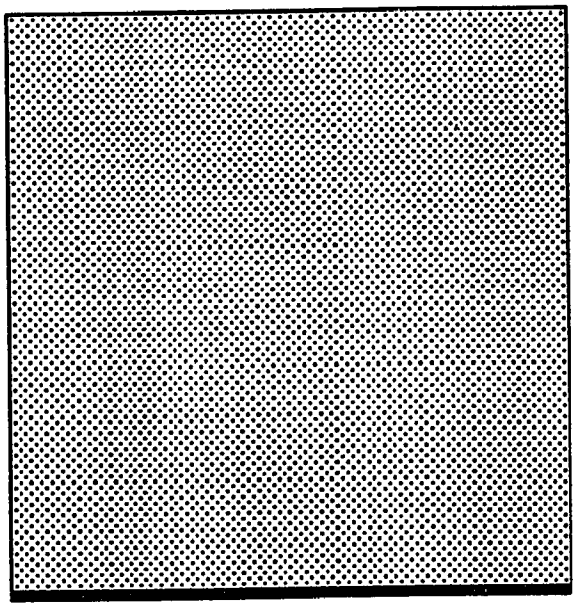

(b)

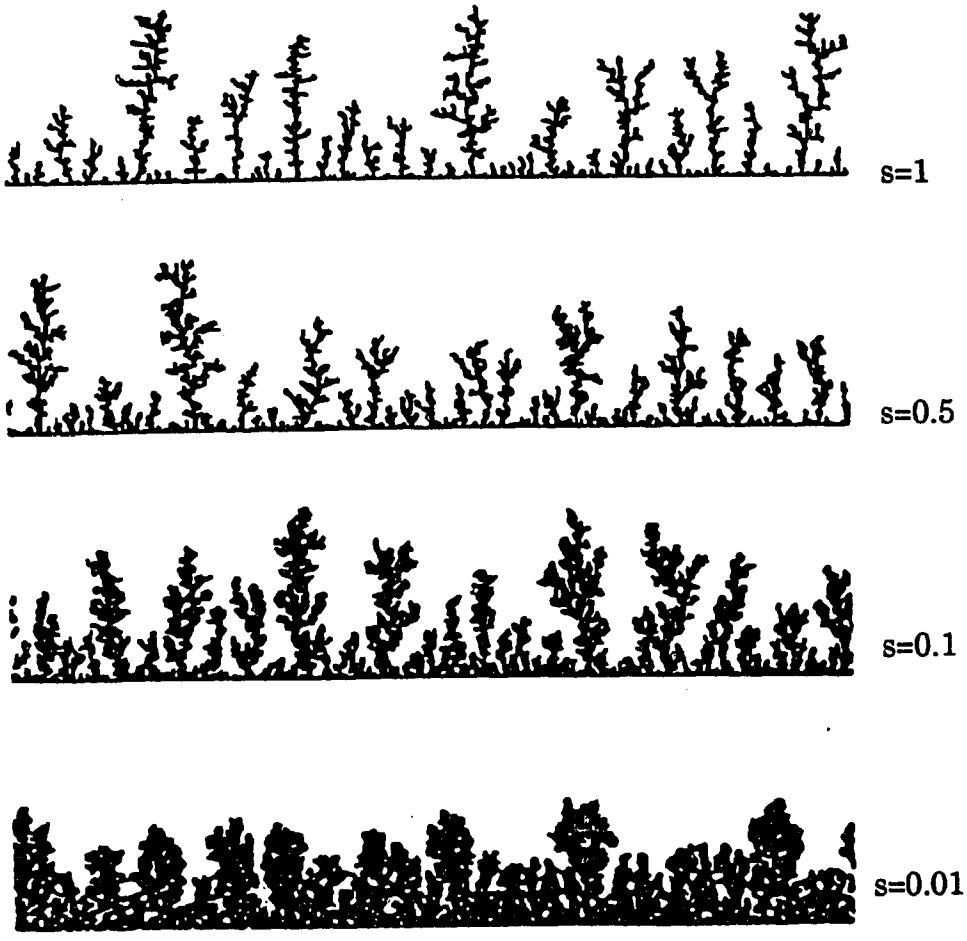

Figure 2.2: (a) 2D lattice for MPDLD. (b) Structures for f=0.05 [16].

applied potential while **f** is the concentration of the active electrolyte.

2.2. Characterization of the Morphology.

2.2.1 Fractal Dimension:

The concept of fractal was introduced in the seventies by Benoit Mandelbrot[1]. By inventing the word **"fractal"**, he permitted the unification and application of many older works by Cantor, Poincare, Van Koch, Julia, et.al., on special functions which do not admit derivatives at any point. This approach, essentially based on geometry, quickly became very popular and is now successfully used in many areas of science.

Fractals are the natural way of representing many of the shapes in nature. Thus, just as Euclidian geometry is the natural way of describing man-made shapes such as squares, triangles or cubes, so fractals are the natural language for describing clouds, trees, leaves and other natural objects.

In the general theory of fractal, one defines a number, the fractal dimension, $\mathbf{d_f}$, which has no special reason to be an integer and which quantitatively measures the more or less rogues aspect of the object.

Suppose we divide a line segment of unit length, shown in figure 2.3(a)[32], into smaller segment of length ℓ. Then the resulting number of segment, $N(\ell)$, is given by,

$$N(\ell) = 1/\ell \sim \ell^{-1} \tag{2.2}$$

Similarly a unit square can be divided (figure 2.3(b)[32]) into smaller squares of side ℓ, then the resulting number of smaller squares, $N(\ell)$ is given by,

$$N(\ell) = 1/\ell^{2} \sim \ell^{-2} \tag{2.3}$$

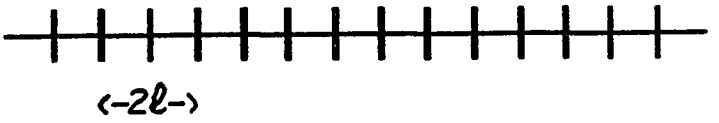

$$N(\ell) \sim \ell^{-1}$$

Figure 2.3(a) Line of unite length divide into smaller segments.

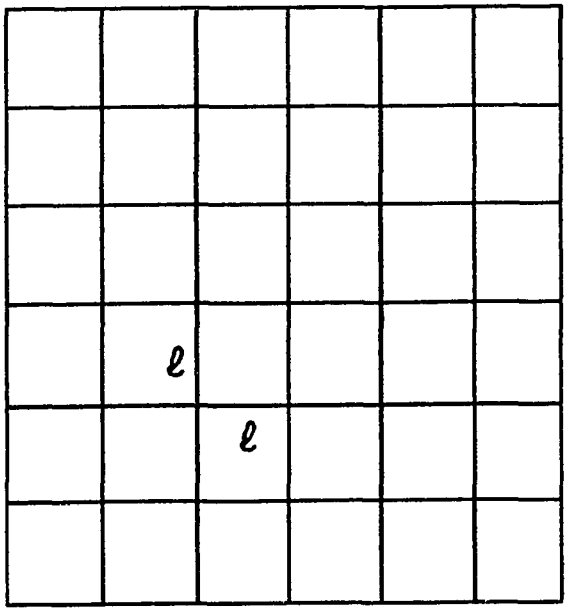

$$N(\ell) \sim \ell^{-2}$$

Figure 2.3(b) Square of unit area divide into smaller squares.

If we follow the same rule, then the number $N(\ell)$ of the smaller cubes of volume ℓ^3 to fill a cube of unit volume is given by the relation,

$$N(\ell) = 1/\ell^3 \sim \ell^{-3} \tag{2.4}$$

Therefore, in general one can write the number-length relation as,

$$N(\ell) \sim \ell^{-d_f} \tag{2.5}$$

where d_f is the fractal dimension of the object. For an object to be a fractal, it must satisfy the relation $d_f > d_T$[1], where d_T is the topological dimension of the object.

The triadic Koch curve is one of the standard examples used to illustrate the fractality of an object. The construction of the Koch curve starts with a line segment of unit length, L(1) = 1. This starting form is called the initiator and may be replaced by a polygon such as an equilateral triangle, a square or some other polygon. The construction proceeds by replacing each segment of the initiator by the generator as shown in figure 2.4, at n = 1. Thus, we obtain the first generation which is a curve of four line segments each of length 1/3. The length of the curve is now L(1/3) = 4/3. The next generation is obtained by replacing each line segment by a scaled-down version of the generator. Thus, in the second generation we have a curve consisting of $N = 4^2 = 16$ segments each having length $\ell = 3^{-2} = 1/9$, and the length of this curve is $L(1/9) = (4/3)^2$. By applying a reduced generator to all the segments of a generation of the curve, a new generation is observed. Therefore, the number of segments, $N(\ell)$ at n^{th} generation,

$$N(\ell) = 4^n \tag{2.6}$$

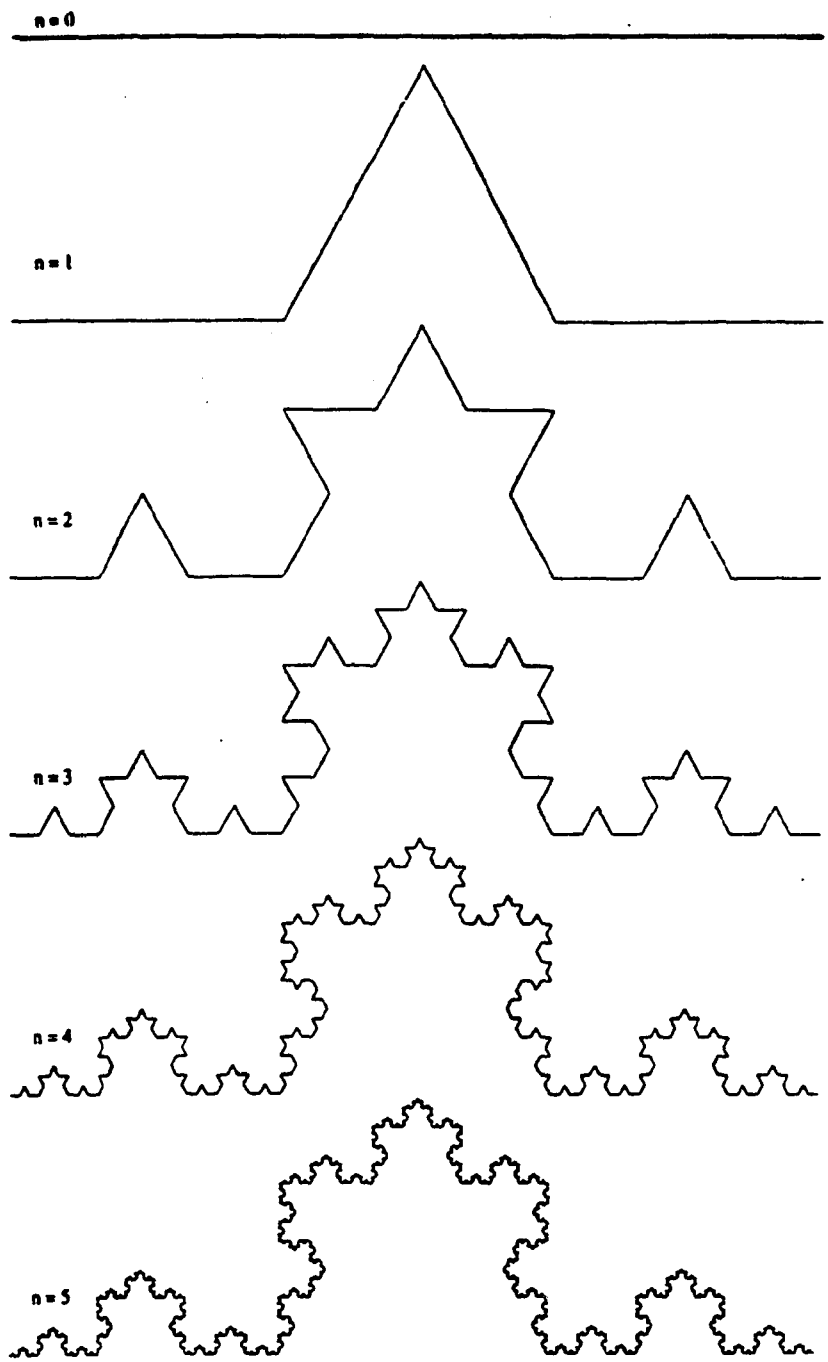

Figure 2.4: Construction of the Koch Curve.

and the length of the each smaller segment is $\ell = 3^{-n}$.

This can be rewritten as $n = -\ln(\ell)/\ln(3)$. Then the equation 2.6, can be rearranged as,

$$N(l) = 4^{-[\ln(\ell)/\ln(3)]}$$

$$= \ell^{-(\ln 4/\ln 3)}$$

$$= \ell^{-d_f}$$

where $d_f = \ln 4/\ln 3 = 1.26$ is the fractal dimension of the Koch curve.

This concept of fractal dimension should be properly defined when using an asymptotic limit to infinitely small lengths. Practically, when considering real physical objects, there always exists a lower limiting characteristic length below which the object cannot be described as a fractal. In particular, when considering digitized images, this natural lower cutoff is the size of a pixel.

2.2.2. Fractal Measures:

The three methods that we used to extract the fractal dimension from a digitized image of an object are:

(i) Density-Density Correlation function [2].

To measure the density-density correlation within a deposits, we computed the C(r) defined by,

$$C(r) = 1/N \sum \rho(r+r') \rho(r) \qquad (2.7)$$

where N is the number of particles in the structure. For example, in a digitized image, N is the number of pixels, those occupied by the structure.

The relation to the fractal dimension is given by [2],

$$C(r) \sim r^{d_f - d} \tag{2.8}$$

where d is the dimension of the space, on which the object is embedded. For the digitized images, d = 2.

The digitized image of a deposit is converted to a binary mode in which black(structure) and white(empty space), using a thresholding routines. Then the equation 2.7 is calculated for all the occupied(black) pixels for a given r and the resulting C(r) is averaged over the all the structure points, in such a way that the density $\rho(r)$ of a pixel (r is the position vector) is 1 for occupied pixel and 0 for unoccupied pixel. The fractal dimension is obtained taking the best-fit slope of ln[C(r)] vs. ln(r).

(ii). Sandbox Method [33].

This method is due to the earlier work of Forrest and Witten on Smoke-particle aggregates.

The relation of the procedure is given by,

$$N(\ell) \sim \ell^{d_f} \tag{2.9}$$

where $N(\ell)$ is number of points within an imaginary box of side ℓ.

For our purpose, we implement this method as follows. As shown in figure 2.5., about every occupied pixel of the image, we forms an imaginary square box of side ℓ. The number $N(\ell)$, of occupied(black) pixels within the box is counted and averaged over all the occupied pixels as centers. A log-log plot of $N(\ell)$ vs. ℓ has slope d_f.

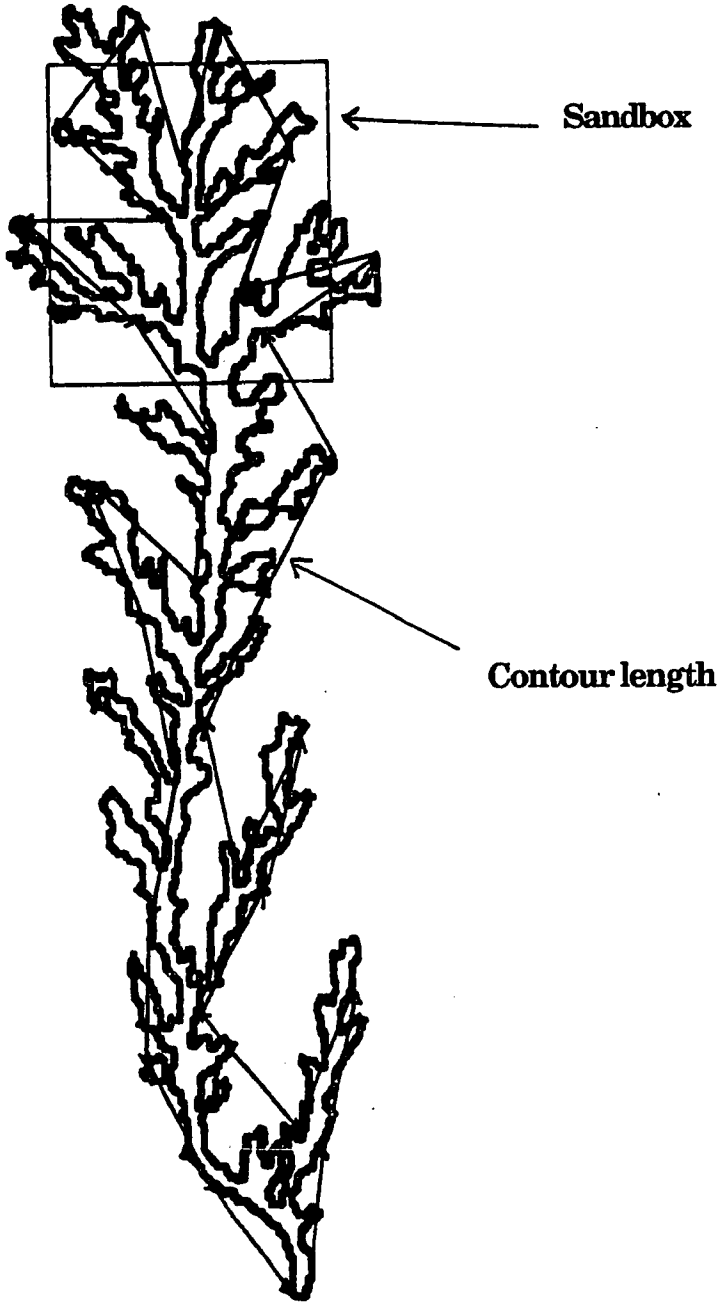

Figure 2.5: Boundary of a tree, the Sandbox and the Contour length methods.

(iii). Counter Length Method [5].

This method uses the relation given in equation 2.5, by directly measuring the length of a boundary with rulers of different lengths.

The boundary, represented by single pixel thick line, of a binary threshold image is printed on a printer, as shown in figure 2.5. The number $N(\ell)$ needed to cover the boundary with a ruler of length $\ell=1$, measured in units of a pixel, is counted. Then we repeat the same operation for a range of increasing ℓ values. The log-log plot of $N(\ell)$ vs. ℓ has slope $-d_f$.

2.3. Kinetics of charge transfer of electrochemical system.

2.3.1. From Activation, Diffusion to Migration in metal deposition.

The overall reaction of cathodic deposition can be represented by [34];

$$M_{sol}^{2+} + ze^- \text{ ---> } M_{Lattice} + \text{Solvent} \qquad (2.10)$$

where M_{sol}^{2+} represents the solvated metal ion in the bulk of the solution and $M_{Lattice}$ is the metal atom in the bulk of the metal phase. Such reaction may consist of the following successive or simultaneous steps.

1. Transport of the solvated ion from the bulk of the solution to a position at the outer Helmholtz layer from which it can be transferred in to the electrode surface.
2. Charge transfer between the electrode and the ion and its partial dehydration.
3. Lateral motion to a position of incorporation into the lattice or encounter with other particles to form a crystal nucleus.
4. Incorporation of the particle into a "fixed" lattice position.
5. Continuation of the process until the atom is incorporated underneath the new surface.

The experimental parameters that are under control in an electrochemical experiment are the electrode potential that to a large degree will determine the rate of step 2., and concentration of the electrolyte that will largely effect step 1.

For a mixed activation and diffusion controlled electrochemical reaction under steady-state conditions and under conditions in which the surface area does not charge in the course of the reaction the

current density varies with the electrode potential (see Appendix A) according to [35].

$$i = i_0 \left(\frac{i_{l,c} - i}{i_{l,c}} f_c(\eta) - \frac{i_{l,a} - i}{i_{l,a}} f_a(\eta) \right) \tag{2.11}$$

where

$$f_c(\eta) = \exp\left(\frac{\alpha_c n F \eta}{R T}\right) \tag{2.12}$$

$$f_a(\eta) = \exp\left(\frac{\alpha_a n F \eta}{R T}\right) \tag{2.13}$$

$$\eta = E - E_0 \tag{2.14}$$

Where i_0 is the exchange current, $i_{l,c}$ and $i_{l,a}$ are the diffusion limited current, α_a and α_c are the transfer coefficients of the anodic and cathodic reactions, F is the Faraday number, R is the gas constant, T is the absolute temperature, n is the number of electrons that participate in the rate determining step of the reaction, and η is the overpotential (the difference between the electrode potential E and the thermodynamic equilibrium potential E_0).

In this work, (cathodic deposition) the electrode potentials are negative enough to justify neglect of the anodic reactions, then we are left with cathodic term in equation (2.11):

$$i = i_0 \left(\frac{i_{l,c} - i}{i_{l,c}} f_c(\eta) \right) \tag{2.15}$$

Since the evolution of the morphology at the electrode makes it difficult to perform a steady state measurement, we used the linear sweep voltammetry (LSV) method to obtained the current-potential (i-E) curve.

By proper treatment of the linear potential sweep data, the voltammetric i-E curve can be transformed into forms, closely resembling the steady-state voltammetric curve, given by equation (2.15)[see Appendix B]. This transformation makes use of the convolution principle [35] by introducing semi-integral current I(t), given by:

$$I(t) = \frac{1}{\sqrt{\pi}} \int_0^t \frac{i(u)}{\sqrt{(t - u)}}\, du \qquad (2.16)$$

In terms of I(t), equation (2.15) takes the form:

$$i = i_0 c^{\alpha} \left[1 - \frac{I(t)}{I_l}\right] f(\eta) \qquad (2.17)$$

This is the convolutive, steady-state form for totally irreversible reaction, such as metal deposition.

After rearranging equation (2.17):

$$\ln\left(\frac{i(t)}{I_l - I(t)}\right) = -\frac{\alpha n F}{R T} E + \left(\ln\left(\frac{i_0 c^{\alpha}}{I_l}\right) + \frac{\alpha n F}{R T} E_0\right) \qquad (2.18)$$

By using the plot of $\ln\{i(t)/[I_l - I(t)]\}$ vs E, we can obtained the kinetic parameters such as exchange current (i_0), transfer coefficient (α) of the reaction and the semi-integral limiting current given by,

$$I_l = nFAD^{1/2}C \qquad (2.19)$$

where A is the area, D is the diffusion constant, and C is the concentration of the electrolyte.

One possibility of equation 2.19 is that by taking the diffusion constant and the concentration one can calculate an "effective area for the current limiting condition". (But, one should keep in mind that during the course of the experiment the area increases significantly and the applicability of equation 2.19 is questionable).

2.3.2. Impedance and Constant Phase Angle (CPA).

We define electrochemical systems in terms of charge transfer across an interface between a solid electrode and an electrolyte. The driving force for the charge transfer reaction is the potential drop across the interface (as discussed in previous section). This requires that the electric current between the electrode and the electrolyte will be a unique function of the voltage drop across the interface. As was seen in the previous section 2.3.1, all the mechanistic information about the rate limiting steps in such system is contained in the functional relation (2.11); we simply write I(E), where E is the voltage drop across the interface and I is the current.

If we introduce a small time dependent perturbation in the voltage ΔE, the resulting change in the current can be expand in Taylor series to yield

$$I\left(E + \Delta E\right) = I(E) + \left(\frac{\partial I}{\partial E}\right)_{E,I} \Delta E + \left(\frac{\partial^2 I}{\partial E^2}\right)_{E,I} \Delta^2 E + \ldots\ldots\ldots\ldots \qquad (2.20)$$

If the amplitude of the perturbation is small enough such that the second and higher derivatives can be neglected, the resulting charge in the current can be expressed as:

$$\Delta I = \left(\frac{\partial I}{\partial E}\right)_{E,I} \Delta E \tag{2.21}$$

We define

$$Y(\omega) = Z^{-1}(\omega) = \left(\frac{\partial I}{\partial E}\right)_{E,I}$$

as the admittance of the system and $Z(\omega)$ as its impedance ω is the angular frequency of the perturbation.

Considering the system with simplest electrochemical reaction, as in section 2.3.1, if we impose a small perturbation of potential defined by $\Delta E \exp(j\omega t)$, we can write the total impedance [see Appendix C], [36] of the system,

$$Z(\omega) = R_{ct}\left[1 + \frac{\lambda}{(j\omega)^{\frac{1}{2}}}\right] \tag{2.22}$$

where

$$\lambda = \frac{k_f}{\sqrt{D_O}} + \frac{k_b}{\sqrt{D_R}} \tag{2.23}$$

Here $R_{ct}\lambda/(j\omega)^{1/2}$ is called Wraburg [37] impedance and $j = \sqrt{-1}$.

Therefore, we can write real and imaginary parts of the equation (2.22) separately as,

$$\mathrm{Re}\,(Z_\omega) = R_{ct}\left(1 + \frac{\lambda}{(2\omega)^{\frac{1}{2}}}\right) \tag{2.24}$$

$$\mathrm{Im}\,(Z_\omega) = R_{ct}\frac{\lambda}{(2\omega)^{\frac{1}{2}}} \tag{2.25}$$

This shows that the real and the imaginary parts of the impedance should vary linearly with $\omega^{-1/2}$.

This is a special case of a more general case named often as constant phase angle (CPA) behavior [38-42], in which the real and imaginary parts are linear with ω^{-n}, where $0 \leq n \leq 1$. The importance of constant phase response was first emphasized by Fricke [38] and the CPA was explicitly mentioned by Cole and Cole [39].

Expressed in this way, impedance measurements do not provide direct information about the system. In order to gain useful information, one has to build a model for the mechanism of charge transfer in the system; express the model in terms of I(E) relation; superpose on E the small time dependent perturbation; calculate the resulting change in I, from which one can calculate the expected frequency dispersion of the impedance and then compare the expected results with the measured one; then determine the validity of the model and the values of the physical parameters that appears in the model. In many practical cases this procedure is very complicated and the equations very rarely can be solved in an analytical way and one needs to restore it to numerical solutions.

The alternative to this approach is to represent the system in electrical engineering terms. This implies utilizing electrical circuit element such as capacitors and resistors while correlating these elements with some physical processes and charge accumulation modes in the system and building the electrical network and comparing the response of this network with the measured response [36,42]. In general, when this approach is being used, capacitor (C) represents charge accumulation modes while resistors (R) represent charge transfer modes. We associate the product of a capacitance and a resistive elements, RC = τ, with the corresponding relaxation time of the charge accumulation mode.

In the past, different forms of CPA have been used to represent the experimental data. Among those, the simplest CPA term, which comes as a general form of equations (2.24) and (2.25) is,

$$Z_{CPA} = A\,(j\omega)^{-n} \tag{2.26}$$

Where $j = \sqrt{-1}$, and ω is the frequency of the signal and $0 \le n \le 1$ is the CPA exponent. This Z_{CPA} describes an ideal capacitor for n = 1 and an ideal resistor for n = 0.

A more generalized term to described the CPA type behavior was introduced by Davidson and Cole [43] in the form:

$$Z_{CPA} = N\,(1 + j\omega\tau)^{-n} \tag{2.27}$$

where j and ω has the same meaning as equation (2.26). At the low frequency limit N is related to the resistance of the storage mode and $n\tau/N$ to its capacitance. At the high frequency limit this element is identical to the CPA element given in equation (2.26).

Z_{CPA} in this form can include contribution from static disorder such as porosity [44-47], random mixture of conductor and insulator that can be described by the effective medium approximation at percolation [48], an interface that can be described by a fractal geometry.

Le Mehaute and Crepy [17] were first to propose a correlation between the two parameters in the form of,

$$n = \frac{1}{d_f} \tag{2.28}$$

where n is the CPA exponent and d_f is the fractal dimension of the interface of a two dimensional system ($1 \leq d_f \leq 2$). An analytical model for the a.c. response of a fractal interface has been proposed by Liu [18] and refined by Kaplan and Gray[49]. This model is based on the "Cantor bar" electrode (Figure 2.6(a)) and the electrical circuit analog of the interface is shown in figure 2.6(b). The resistance R in the electrolyte increases by the ratio **a** at every stage of branching because of the reduction in cross-sectional area. The capacitance C is assumed to be the same at every stage and represents the interfacial capacitance of the two lateral faces of the branch.

The resulting impedance of the network is as follows, when written in condensed form of writing the fraction [18]

$$Z(\omega) = R + \frac{1}{-j\omega C +} \frac{2}{aR +} \frac{1}{j\omega C +} \frac{2}{a^2R +} \ldots\ldots \tag{2.29}$$

It is shown by Liu in his original paper [18] $Z(\omega)$ satisfies the following frequency scaling.

$$Z\left(\frac{\omega}{a}\right) = R + \frac{a\,Z(\omega)}{-j\omega\,Z(\omega) + 2} \tag{2.30}$$

(a)

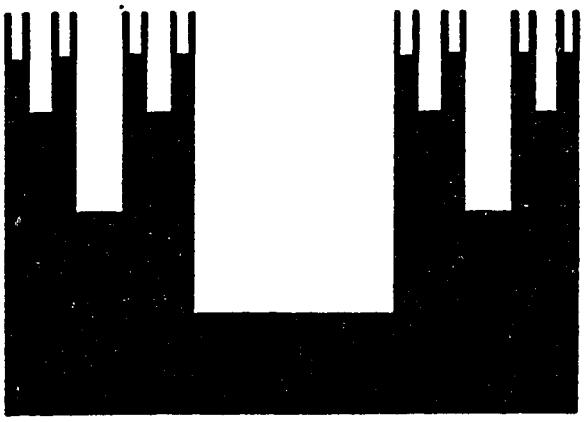

(b)

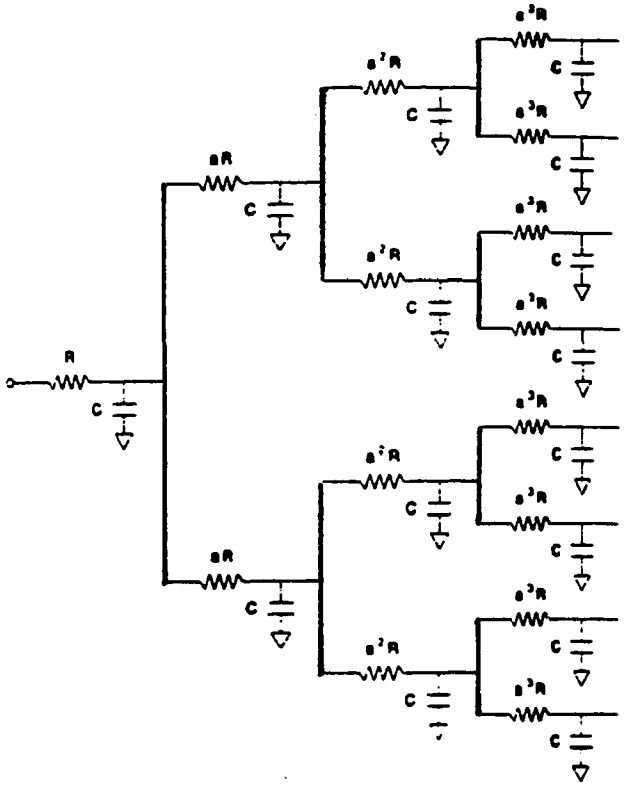

Figure 2.6: (a) Cantor bar electrode[18].
(b) Equivalent circuit of (a).

In the low frequency limit,

$$Z\left(\frac{\omega}{a}\right) \approx \frac{a}{2} Z(\omega) \tag{2.31}$$

The solution to equation (2.31) is

$$Z(\omega) = K R (j\omega)^{-n} \tag{2.32}$$

where K is a scale factor and $n = 1 - \ln 2 / \ln a = 1 - d$.

The length of the border of Cantor bar has the fractal dimension (interface fractal dimensions), $d_f = 1 + d$.

Thus the general relation between n and d_f is,

$$n = 2 - d_f \tag{2.33}$$

At the same period Pajkossy and Nyikos[19] made an attempt to derive a relation between n and d_f by arguing that the admittance (Y) of a blocking interface,

$$Y = \sum_i \frac{j\omega C_i}{1 + j\omega R_i C_i} \tag{2.34}$$

obey the scaling laws when the whole system is blown up spatially by a factor of r;

$$Y(r.1,\omega) = r^2 Y(1,\omega) \tag{2.35}$$

and similarly R_i and C_i, the resistance and the capacitance of the i^{th} element;

$$C_i(r.1) = r^d C_i(1) \tag{2.36}$$

$$R_i(r.1) = r^{-1} R_i(1) \tag{2.37}$$

where "1" and "r.1" stands for the original values and the new values after the blowup and d is the fractal dimension of the surface.

Comparing equations (2.34), (2.36) and (2.37) they obtained the

relation:

$$Y(r.1, \omega) = Y(1, r^{d-1}\omega) \tag{2.38}$$

and equations (2.35) and (2.38) yields;

$$\frac{Y(1, r^{d-1}\omega)}{Y(1, \omega)} = r \tag{2.39}$$

Since the variation of the admittance with ω can also be described by the CPA relation;

$$Y(\omega) \sim (j\omega)^n \tag{2.40}$$

They assume the relation;

$$\frac{Y(k\omega)}{Y(\omega)} = k^n \tag{2.41}$$

is holds for a blocking interface where k is a real scaler factor.

Comparing (2.39) and (2.41) with assuming $k=r^{d-1}$ they obtained;

$$n = \frac{1}{d-1} \tag{2.42}$$

This relation with the interface fractal dimension $d_f(=d-1)$ will reduced to the Le Mehaute relation (2.28).

All these correlations were derived on the basis of blocking nature of the solid/electrolyte interface.

Recently, Sapoval et.al.[50] used scaling arguments on a modified sierpinski (non-blocking) electrode to show that the correlation between the CPA exponent and the fractal dimension of the interface is independent of the dielectric properties of the interface and only the cutoff frequency varies with the dielectric properties. Their argument is based on analysis of a fractal size distribution of single pores using

de Levie's transmission line model[44-46]. This model predicts CPA exponent of 0.5 for a diffusion free interfacial impedance. However, the high frequency cutoff of the CPA is a function of almost all the dielectric components of the system and the diameter of the pore. The superposition of the individual pore's cutoffs produces a CPA exponent which is independent of the dielectric properties of the interface and n agreement with Liu's linear correlation.

Our objective in this work is to explore the correlation between n and d_f experimentally and to compare this with the two relations given by equations (2.28) and (2.33).

2.4. Earlier Experimental Work.

2.4.1. Experiments before the DLA:

Most of the early experimental work was aimed at problems that are related to the functionality of battery electrodes. As mentioned in the introduction, one of the interesting microphotography experiments performed by Wranglen [8] in the period of 1954-1955, shows a remarkable similarity in the deposits of Pb, Cd and Ag to the recent simulation of Noise reduce DLA [7] type structures. In addition to figure 1.1, here we see, from figure 2.7, two and three dimensional growth of Pb. Wranglen pointed out that by confirming the X-ray analysis of these structures, dendrites in the fcc lattice branches along [110] directions. At high current densities Pd develops dendrites branching along [100] while Sn grows along the [101] at low current densities.

2.4.2. Experiments after the DLA:

The first experimental attempts to explore fractal structures generated by electrodeposition under diffusion limited conditions were performed by Brady and Ball [9] and Matsushita et.al. [10].

In the Brady-Ball experiment, shown in figure 2.8, copper is deposited from aqueous $CuSO_4$ solution onto the exposed end of a copper wire. The solution is placed inside a hole drilled in a copper block, which acts as the anode. A water soluble polymer (polyethylene glycol) is added to the solution to avoid fluid convection and an excess of Na_2SO_4 is used to screen the electric field.

The cluster radius R, of a deposit, is proportional to the diffusion

Figure 2.7: (a) Pb dendrite; deposited at I=0.3A/cm^2[8].

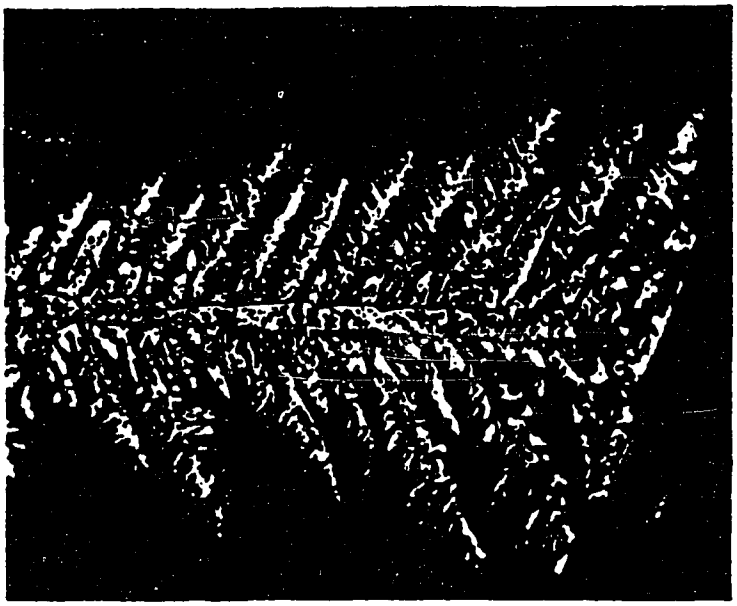

Figure 2.7: (b) Pb dendrite; deposited at I= 0.05 A/cm^2[8].

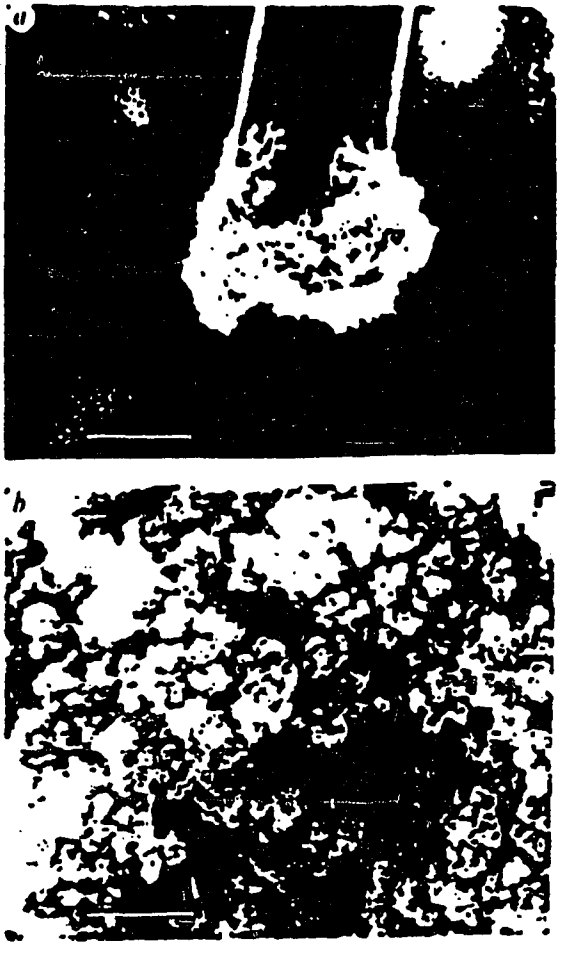

Figure 2.8: Electron micrograph of a deposit grown for only 1min. in 0.01M $CuSO_4$/ 0.05M Na_2SO_4 at 6V in two different magnifications[9].

limited current, I [51-53],

$$R \sim I \tag{2.43}$$

The effective density of the deposit, $\rho \sim R^{-2}\, dM/dR$, where M is the deposit mass, and with the Faraday law $M \sim \int I\, dt$, can be written as,

$$\rho \sim (I\, dI/dt)^{-1} \tag{2.44}$$

If the deposit is self-similar, the effective density given by equation 2.8, $\rho \sim R^{d_f - d}$ with d=3 for three dimensional configuration of the experiment. Using equations 2.8 and 2.44, the slope of a log-log plot of $(I\ dI/dt)^{-1}$ vs. I gives the d_f. Brady and Ball found that the copper deposits have self-similar structures with fractal dimension $d_f = 2.43 \pm 0.03$, which is in good agreement with that of three dimensional DLA [2,3], clusters [54].

In the Matsushita et.al. [10] experiment, metallic zinc in the form known as zinc metal-leaves is grown two-dimensionally. The experimental procedure used to grow Zinc metal-leaves is as follows: A glass vat of diameter 20cm and depth 10cm filled with 2M $ZnSO_4$ solution (depth 4mm), on to which butyl acetate $[CH_3COO(CH_2)_3CH_3]$ is floated to make an interface. A tip of a Carbon cathode (0.5mm) is set at the center of the vat, so that the flat tip is placed just at the interface. The electrodeposition is initiated by applying a d.c. voltage between the carbon cathode and a zinc ring-plate anode of diameter 17 cm, width 2.5 cm and thickness 3mm placed in the vat. A zinc metal leaf grows two dimensionally at the interface between the two liquids from edge of the flat tip of the cathode towards the outside anode with an intricately branched random pattern (Figure 2.9). They also observed that, when the cathode is rounded or is immersed in the $ZnSO_4$ solution, the

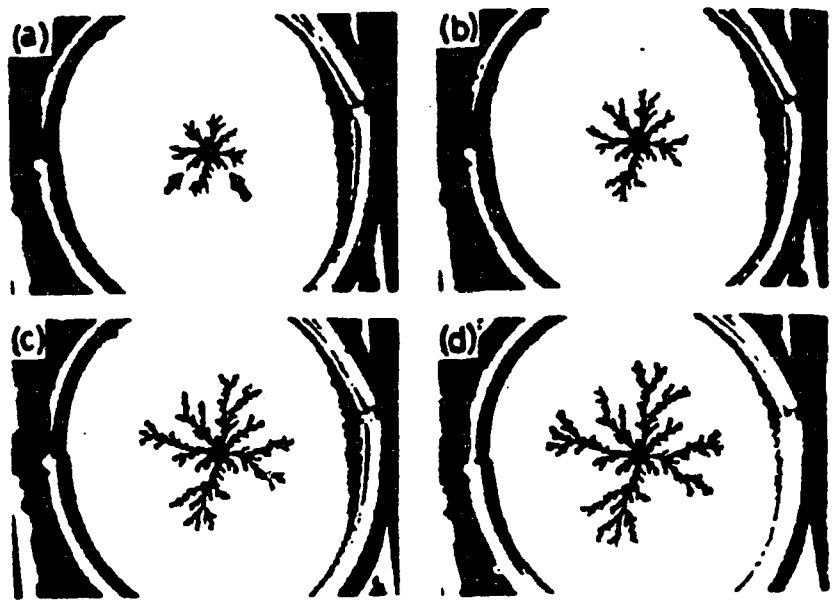

Figure 2.9: Electrodeposits from 2M $ZnSO_4$
(a)-(d): taken at 3, 5, 9, and 15 min.[10].

deposit grows three dimensionally into the solution.

The growth of the deposits was recorded on a camera and then processed by image analysis techniques to obtain a density-density correlation function C(r) of the two dimensional deposit patterns and obtained a fractal dimension $d_f = 1.66 \pm 0.03$ when the applied d.c. voltage is less than some threshold value. This is in excellent agreement with that of two dimensional DLA patterns [2,3].

If the applied voltage is increased above the threshold value, the value of the fractal dimension changes drastically. In order to elucidate the morphological change involved, more extensive studies of the electrodeposition were performed by Sawada et.al.[12] and Grier et.al.[13]. Both groups deposited zinc on a cathode from two plexiglass plates. They observed not only structures similar to DLA patterns but also regular dendritic or "homogeneous", (Figure 2.10), "dense radial" and "needle-like" or "stringy", (Figure 2.11) patterns. Both groups presented their results in a phase diagram shown in Figure 2.12, showing the dependence of the morphology on the applied d.c. voltage and on $ZnSO_4$ concentration. In spite of the similar experiments, the phase diagrams seemed very different from each other. Later Grier et.al. [14] investigated, in particular, the stability of the "dense radial" morphology both experimentally and theoretically and attributed it to the non-negligible resistivity of growth channels of the dense radial electrodeposition.

Matsushita et.al.[55] also performed experiments on the electrodeposition of zinc on a line cathode in a two dimensional system. A typical example of time evolution of the deposits is shown in figure 2.13. A fractal dimension of $d_f = 1.70 \pm 0.06$ was obtained from the dependence of the r.m.s. deposit thickness (or height of trees), T, and the

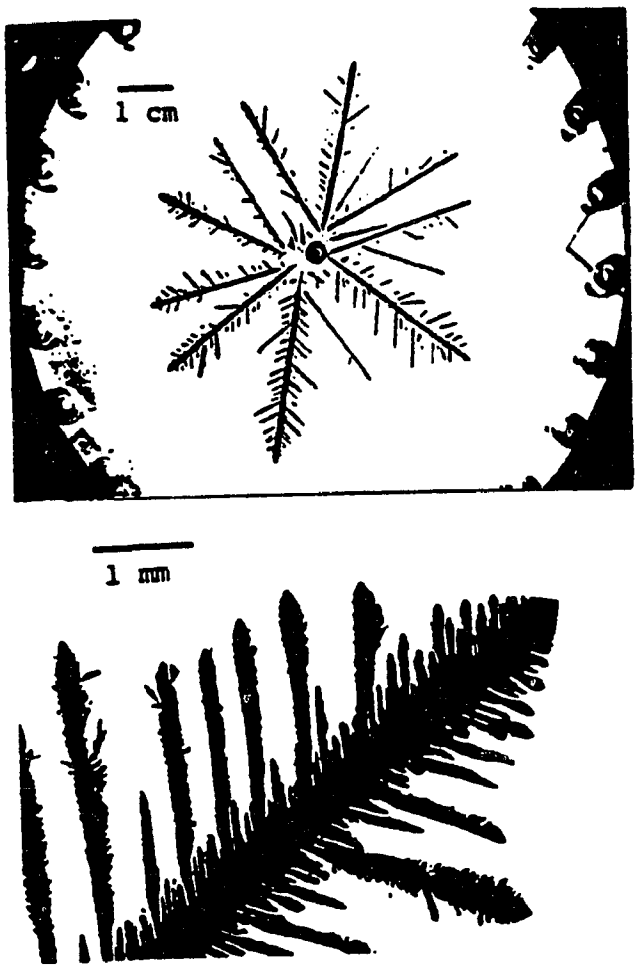

Figure 2.10: Dendritic pattern found in 0.03M $ZnSO_4$ at 6V[12].

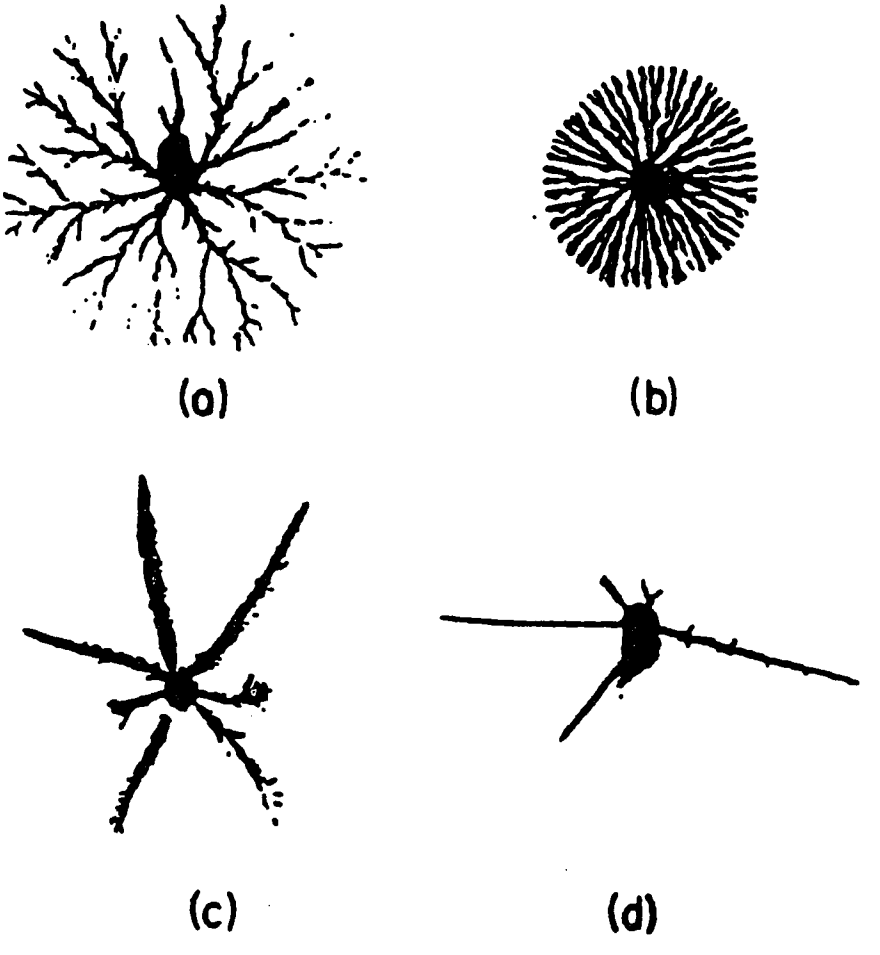

Figure 2.11: Patterns in electrochemical deposition of zinc[13]: (a) - (d) are grown under the condition indicated by points a - d in Fig. 2.12(b).

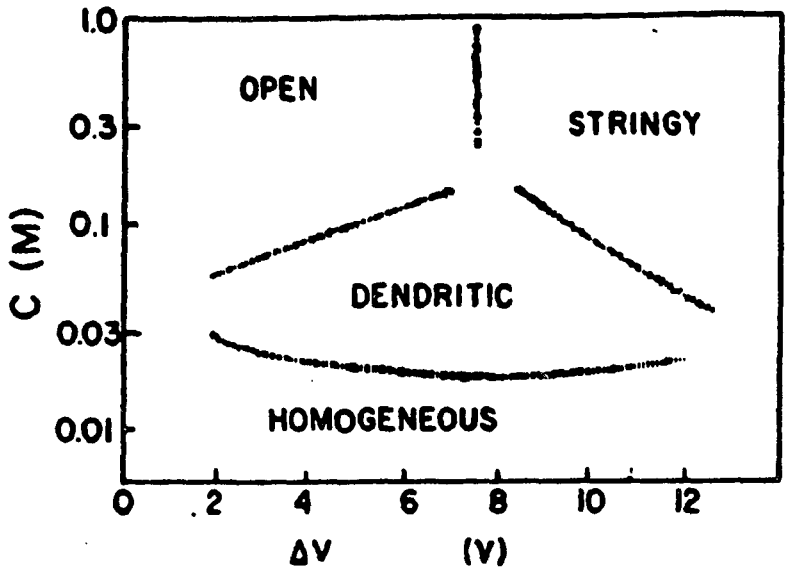

Figure 2.12: (a) Phase diagram due to Sawada et.al.[12].

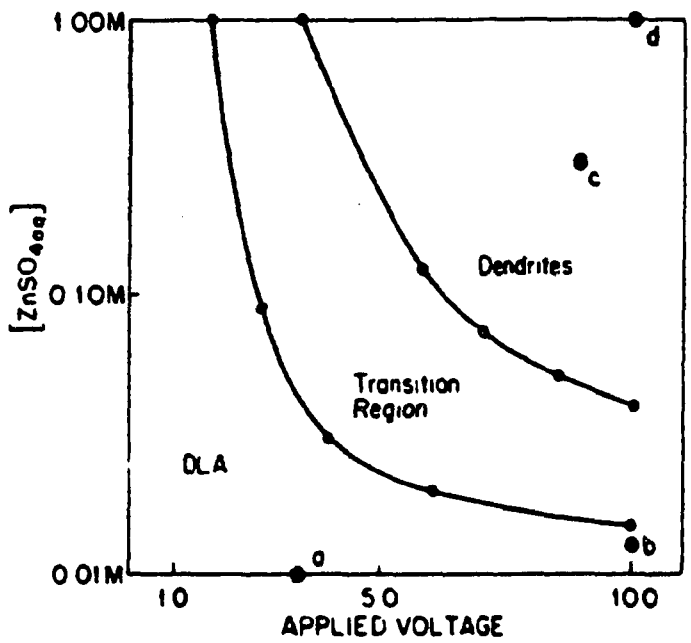

Figure 2.12: (b) Phase diagram due to Grier et.al.[13].

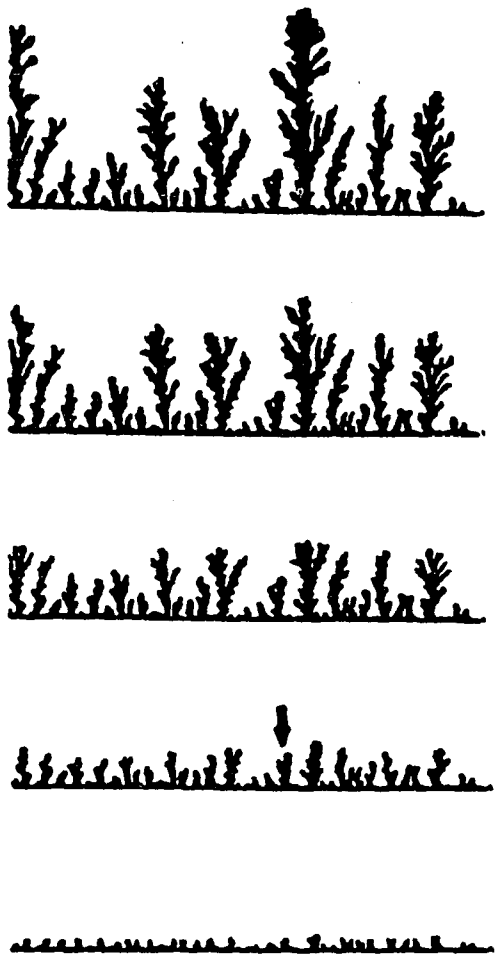

Figure 2.13: Time evolution of zinc deposition on a linear cathode from 2M $ZnSO_4$ at 20V[55].

deposit area per unit cathode length N, through the relation,

$$N \sim T^{d_f - 1} \tag{2.45}$$

This is in good agreement with theory [56] and with computer simulations for single particle diffusion limited deposition [57] and multi-particle diffusion limited [15,16,58] deposition at high sticking coefficient probability. These results are in good agreement with large-scale computer simulation [59] and with the scaling ideas of Racz and Vicsek [60].

Kaufman and co-workers [11,61,62], performed diffusion limited, two dimensional polymerization, of pyrrole in a thin-layer electro-chemical cell consisting of two glass plates, similar to that used by Sawada et.al. [12] and Garier et.al. [13]. The solution in the cell was 0.1M pyrrole/0.1M AgO toluene sulphonate/acetonitrile. The growth of ploypyrrole involved electrochemical oxidation of neutral pyrrole monomers. Above some threshold applied voltage, diffusion-limited conditions were obtained and two dimensional DLA-like clusters, shown in figure 2.14, with fractal dimension of 1.70 ± 0.03 were obtained.

Since the polypyrrole clusters obtained were durable enough to be handled for electrical measurement, they were able to carry out conductivity measurement. The resistivity ρ between two points at a distance r apart on a deposit with no loops such as DLA patterns is proportional to the minimum path length ℓ on the deposit, while ℓ scale as,

$$\ell \sim r^{D_{min}} \tag{2.46}$$

Hence, the conductivity is a direct measure of the minimum path dimension D_{min}. They determined D_{min} of 0.96 ± 0.04 by scale

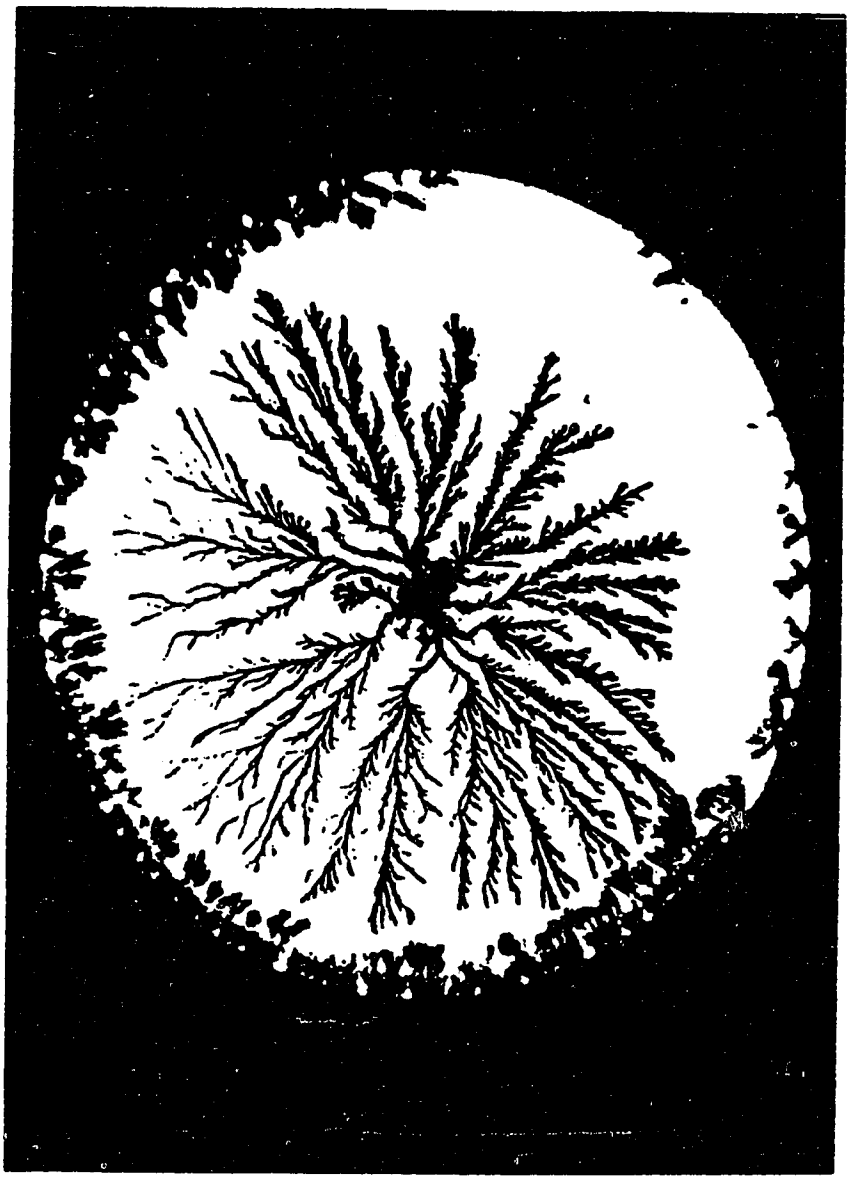

Figure 2.14: Polypyrrole aggregate grown through diffusion limited polymerization at 6V[11].

dependent conductivity measurement and found it to be in good agreement with simulation result [63].

2.5 Motivation

So far we have seen little analytical progress in this field that has been dominated by computer simulation models and sophisticated numerical studies with few experimental observations, which have been led by non-equilibrium statistical physicists.

It is obvious that many of the features which are observed experimentally (section 2.4) appear in the computer simulation (section 2.1). Yet, it is also obvious that the electrodeposition process is considerably richer morphologically than the computer simulation. Most of the classical electrochemical kinetics is based on deviations from equilibrium thermodynamics, and is controlled by the overpotential of the electrochemical reaction (section 2.3). Therefore, any experimental attempt to correlates input parameters in the simulations with the macroscopic parameters of the experimental system must be performed in a controlled electrochemical system.

The key to this kind of experiment is the construction of an electrochemical cell in which the growth is pseudo two dimensional and has to satisfy the following conditions:

1). The cell has to accommodate a reference electrode in a way in which the IR drop will be minimized and that the reference electrode will not interfere with the pattern formation.

2). To ensure conditions which are as close as possible to two dimensional, the cell thickness has to be at a possible minimum value. To ensure that results with such a cell can be compared with the three dimensional counterpart full control over the current distribution and the IR drop in the cell are required.

3). Typical volume of such a cell is very small (~ $4x10^{-3}$ cm^3). Even for 1M concentration of the electrolyte there will be fast depletion of the electrolyte as the pattern evolves. Since the patterns are very sensitive to the local concentration of the electrolyte, the patterns will change with time and therefore reproducible pattern formation will be impossible. To gain control over this effect we need to design the system in such a way that the electrolyte is being regenerated at the counter electrode.

4). The cell has to provide an option for changing electrolyte without disturbing the growth pattern. This is particularly important for experiments in which the image processing is followed by impedance measurements.

The objective is that the experiments and the simulation will "feed on each other" to help us understand these systems. To large extent the input parameters in these simulations are arbitrary. The first issue is to try to correlate the input parameters with the macroscopic parameters of the experimental system. Through a scale transformation to the simulation grid one can correlate the concentration and the diffusion coefficient. The next issue is transferring the interfacial charge transfer parameters such as given by equation 2.11. All the parameters in that equation can be determined by the complete evaluation of the experimental I-η curve in a particular system. The time evolution of the growth patterns will be recorded on the VCR, selected frames will be digitized and the resulting morphology will be characterized through the fractal dimension and compare with the simulation results. One of our objective here is to determine, for the first time, whether the pattern formation as determined by the fractality, follows the evolution of the macroscopic kinetics, as determined by the potential dependence of the

deposition current. In particular, we will try to determine whether the transition from activation controlled kinetics to mass transfer limited kinetics takes place at the same overpotential range as DLA pattern formation starts to dominate.

The electrodeposition of two systems will be investigated: zinc and silver. There is diverse electrochemical literature on the electrodeposition of these metals and an additional level of understanding of the conditions under which morphological patterns form can be of great technological importance. The study of silver is primarily motivated by our ability to control its interface with the electrolyte by selective oxidation which will provide us with the necessary control for meaningful impedance studies of various morphologies.

At the conclusion of this work we hope to be able to contribute to narrowing the gap between the on going theoretical work in non equilibrium statistical physics of growth process and electrochemistry which will undoubtedly serve to enrich both disciplines.

3. Experimental

3.1 Electrochemical cell.

We have constructed an electrochemical cell, which is thin enough for pattern analysis under the microscope, but in which we could place a reference electrode close enough to the working electrode such that we can work under potentiostatic condition with full control over the voltage drop in the electrolyte between the working and reference electrodes. A schematic description of our cell is shown in Fig 3.1. It is a split-level cell with working electrode compartment, (25μm thick, 13mm long and 13mm wide) and a counter electrode compartment on the lower plate of size 1.3x1.3x1 cm. A Pt foil of 2.5μm thick set near the anode between plates to get even thickness. The cathode for the Zn system is a high purity Cu foil and for the Ag system is a high purity Ag foil both of 25μm thick. The anode used for the Zinc system is a Zn rod of 7mm diameter and for the Silver system is a Ag rod of same diameter, placed in the counter electrode compartment.

As a comparison of our cell with a three dimensional cell, we performed the cyclic voltammetry of $6x10^{-3}$M $K_3Fe(CN)_6$ in 1M KNO_3 as the supporting electrolyte with Pt electrodes. Figure 3.2 shows a comparative CV of a conventional three dimensional cell[64] and in our pseudo two dimensional cell. The voltammograms are corrected for IR drop but are not corrected for double layer charging. Also, currents are normalized to the same scale and the sweep rate for both situations is 50mV/sec.

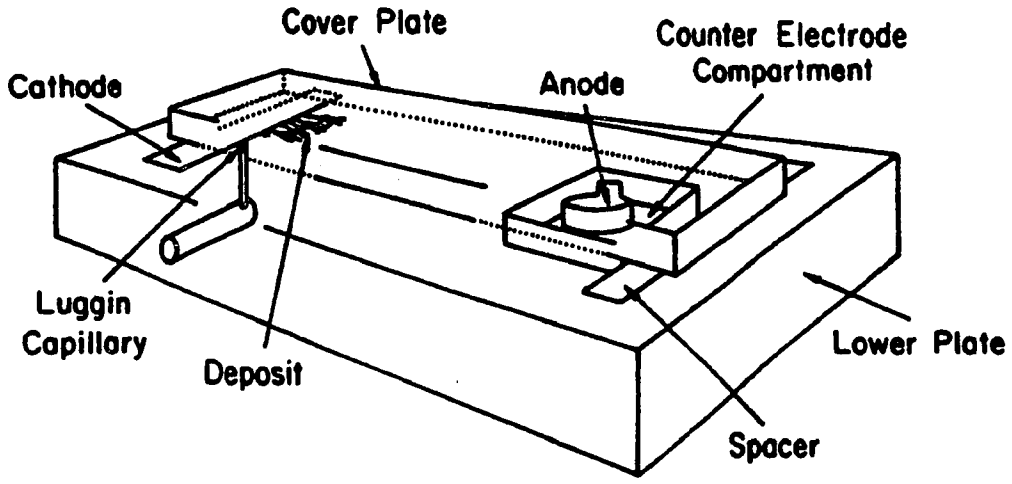

Figure 3.1: Schematic of the electrochemical cell.

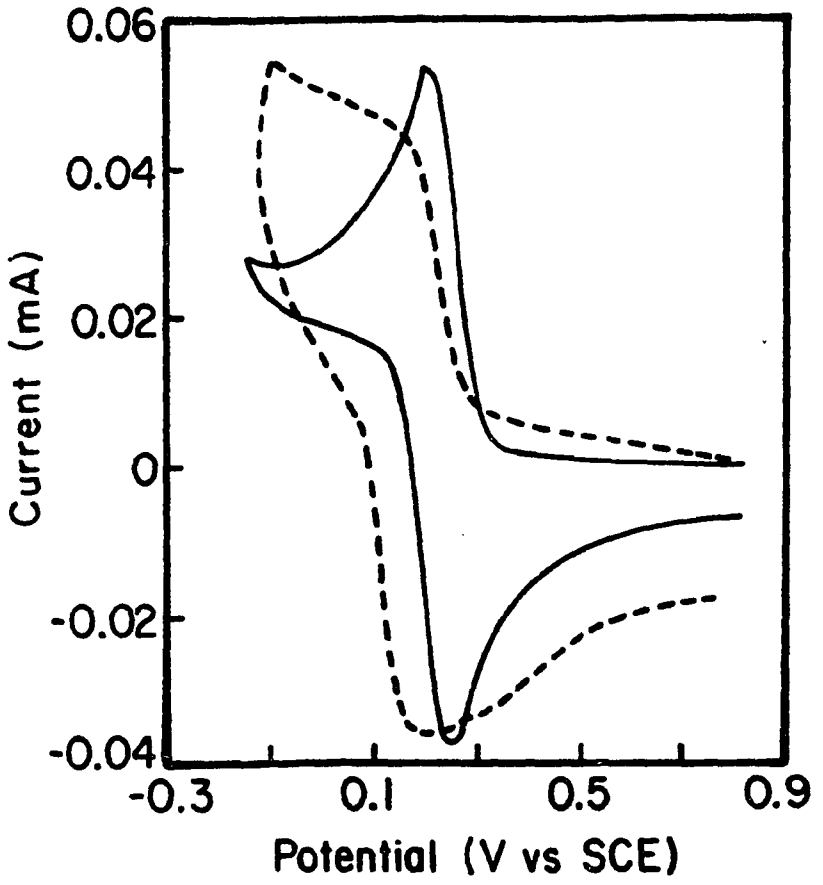

Figure 3.2: Linear Sweep Voltammetry of $6x10^{-5}M$ $K_3Fe(CN)_6$ in 1M KNO_3 supporting electrolyte with Pt. electrodes in a conventional three dimensional cell (solid line)[64] and in our pseudo two dimensional cell (dash line).

3.2. Experimental Technique.

3.2.1. Time-lapse Video Microscopy:

The overall set-up of the apparatus used in the study of morphology is schematically shown in figure 3.3. The time evolution of the growth is observed under Olympus BH2 metallurgical microscope. A Sony XC-37 miniature type video camera attached to the microscope is used to record the real time growth patterns on a video tape, using transmission light source. The growth patterns are recorded as a function of overpotential, applied through the EG&G model 173 potentiostat to the electrochemical cell (Section 3.1) in three electrode configurations. The current-time curves for selected runs were recorded on a chart recorder. A selected video frame is digitized by using the ITI-PCVISION frame grabber with 512x512 resolution (due to the vertical video interlacing the actual resolution is 512x480) onto a IBM PC/XT 286 computer for fractal analysis.

3.2.2 Cyclic Voltammetry (CV):

Cyclic voltammetry is the most versatile electroanalytical technique for the study of electro active species [35,64]. This is often the first experiment performed in the electrochemical study of a system because of its capability for rapidly observing the redox behavior over a wide potential range.

CV consist of cycling the potential of an electrode which is immersed in an unstirred solution and measuring the resulting current. The potential of the working electrode is controlled versus a reference electrode such as a saturated calomel electrode (SCE) or a Silver/Silver Chloride electrode (Ag/AgCl). The controlling potential which is applied across these two electrodes can be considered an

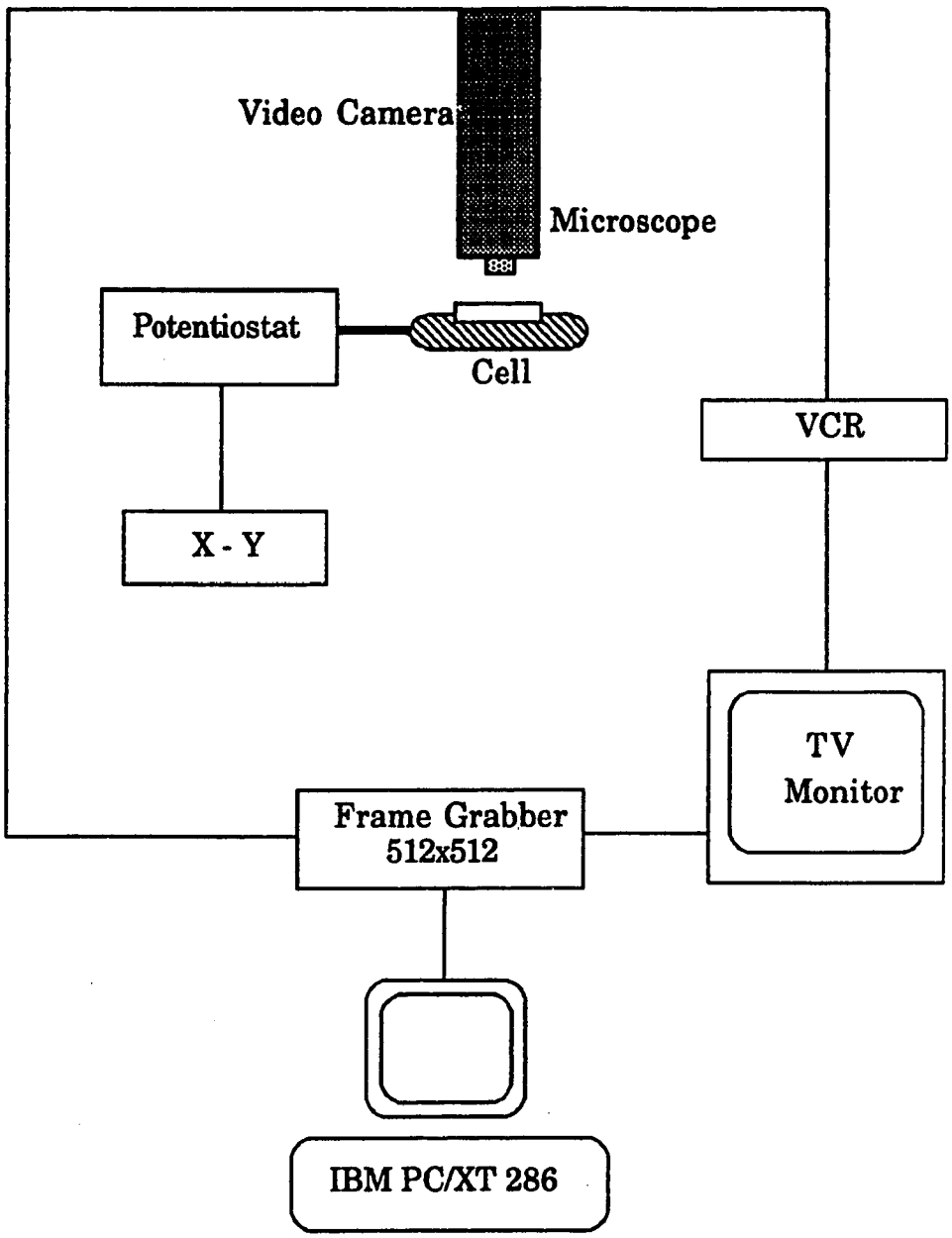

Figure 3.3: Time lapse Video Microscopy Experimental Setup.

excitation signal. The excitation signal for CV is a linear potential scan with a triangular wave form as shown in Figure 3.4. This triangular potential excitation signal sweeps the potential of the electrode between two values, some times called the switching potentials.

A cyclic voltammogram is obtained by measuring the current at the working electrode during the potential scan. The current can be considered the response signal to the potential excitation signal.

For our purpose, it is sufficient to use only the forward scan of the cyclic voltammetry called linear sweep voltammetry (LSV) because we are expecting to obtained the limiting range of the reaction and to transform by convolution. The speed of 50 mv/sec to 200 mv/sec was used to obtained the LSV curves, recorded on a chart recorder then digitized to performed the convolution integral. The EG&G model 173 potentiostat combined with the universal programmer model 175 is used in this study.

3.2.3 Potentiostat (Constant Potential) Method:

By applying constant potential to the cell, we obtained the current-time behavior of the deposit on the working electrode. This is the condition that we used to keep constant sticking coefficient in an experimental situation.

3.2.4. Impedance Spectrum (IS) Analysis:

This is one of the most powerful tools for studying interfacial process such as solid-liquid interfaces [42,65,66].

Figure 3.5 shows schematically the experimental setup employed for the impedance spectrum analysis technique [65]. The Solartron model 1250 frequency response analyzer is used in the low frequency

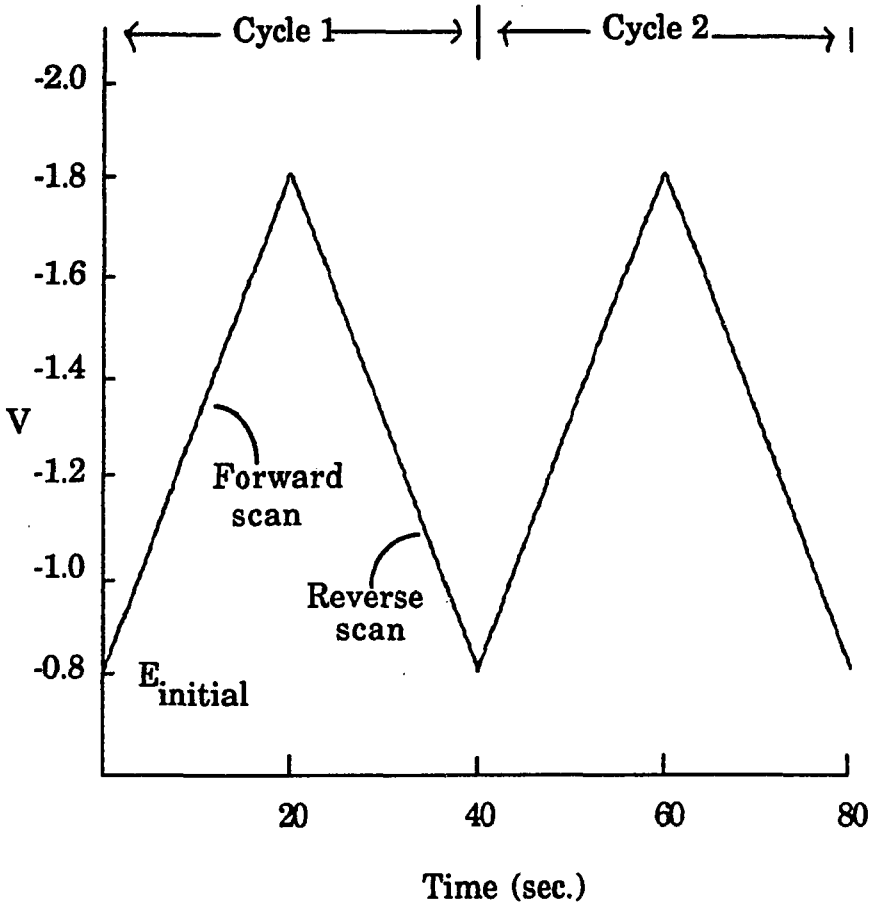

Figure 3.4: Excitation signal for cyclic voltammetry.

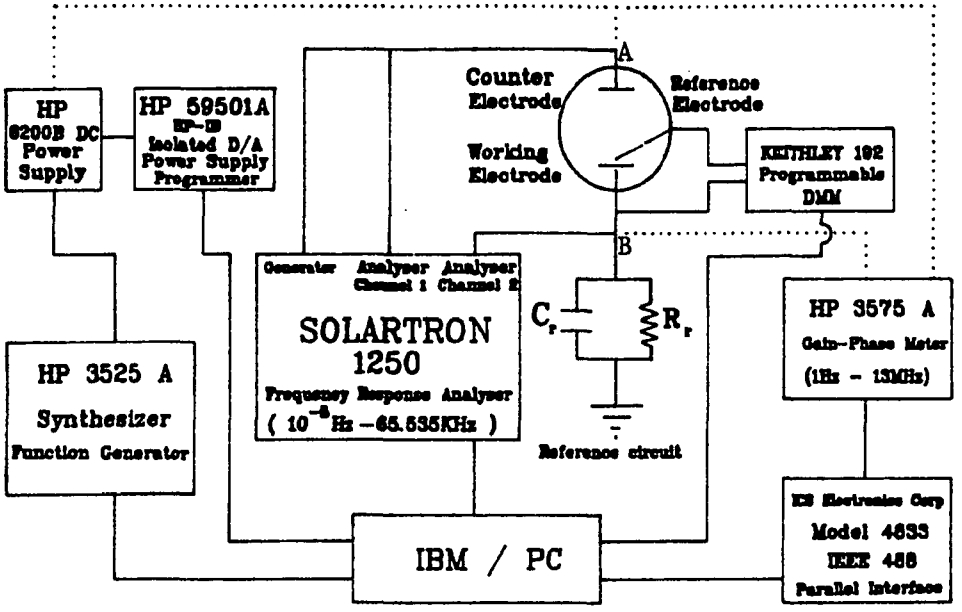

Figure 3.5: Impedance measurement setup.

range, 10^{-5} Hz - 65 kHz. For the high frequency range, a combination of HP 3525A frequency synthesizer and HP 3575A gain phase meter were used and required d.c. bias applied through the HP 6200B power supply. The capable high frequency range is 1 Hz to 13 MHz. In both cases, KEITHLEY 192 programmable digital multi meter was connected to the cell between reference and working electrode to monitor the potential drop. All the instruments are controlled by a IBM PC through the IEEE-488 interface.The two signals originating at A and B (Figure 3.5) are separately fed into two channels of the Solartron (or gain phase meter) which measure their relative magnitudes, M, and the phase difference Θ. This measurement is equivalent to the complex voltage ratio between the two signals at A (E_A) and at B (E_B), which can be expressed as [65]:

$$E_B / E_A = Z_r / (Z + Z_r) \tag{3.1}$$

where Z and Z_r are the impedance of the electrochemical cell and the reference circuit, respectively. We can write:

$$Z = R + jX \tag{3.2}$$

and

$$1/Z_r = 1/R_r - j\,\omega\, C_r \tag{3.3}$$

and then from equation (3.1):

$$R = \{R_r/[1+(\omega\tau_r)^2]\}\ \{\mathrm{Cos}\Theta/M - \omega\tau_r\, \mathrm{Sin}\Theta/M - 1\} \tag{3.4}$$

and

$$X = \{R_r/[1+(\omega\tau_r)^2]\}\ \{\omega\tau_r - \mathrm{Sin}\Theta/M - \omega\tau_r\, \mathrm{Cos}\Theta/M\} \tag{3.5}$$

where ω is the angular frequency, and Θ is the phase angle, M is the

relative magnitude, and $\tau_r = C_r R_r$ is the relaxation time of the reference circuit.

Experimentally, we can determine R and X as function of ω, following the procedure given in the original paper by Tomkiewicz [65]. The plot of log(R) and log(2πX) vs. log(f), must show a region where the two curves are parallel, if there is a CPA element in the system.

4. Results.

4.1. Zinc System:

4.1.1 Preparation:

A copper foil of 25μm thick, one edge polished with emery polishing paper, is used as a working electrode (cathode). The counter electrode is a zinc rod of 7mm diameter set in the counter electrode compartment. The reference electrode is a standard calomel electrode (SCE), connected through the lugging capillary. The electrolyte is made of $ZnSO_4$ which was cleaned by immersing metallic zinc overnight and filtering before use. The Cu cathode and Zn anode were cleaned by etching in dilute HNO_3 and then rinsing with deionized water.

4.1.2. Without Supporting electrolyte:

A detailed comparison of the kinetics with the evolving morphology was performed in 1M and 0.1M $ZnSO_4$ solutions without any supporting electrolyte.

Figure 4.1 shows the time evolution of growth from the 0.1M solution at -1.08V vs. SCE and Figure 4.2 for the 1M solution at -1.05V vs. SCE. The applied potential in both systems is near the equilibrium potential of Zn, hence the growth is in the activation region. As is evident from the two figures, the growth is mossy type and similar to the multiparticle simulation with small sticking coefficient. The overall conclusion is that at low potentials (< -1.1 V vs. SCE) the growth from both concentrations are mossy, initiated by separated nucleation sites with frontal growth.

At potentials just negative of the mossy deposition ($-1.1 < V < -1.13$)

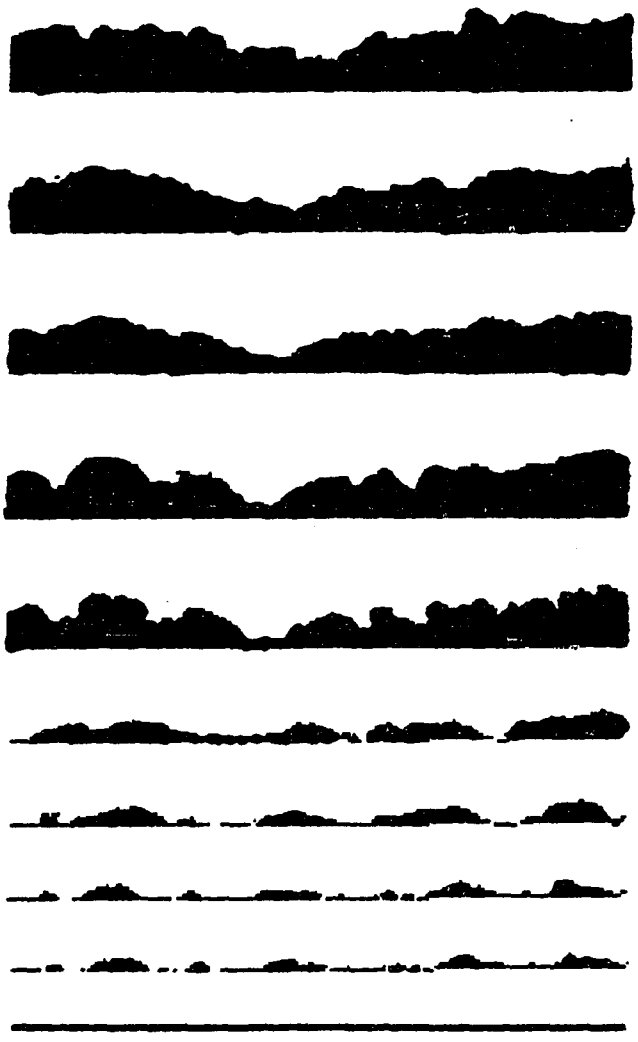

Figure 4.1: Time evolution of the growth pattern from 0.1M $ZnSO_4$ at -1.08V vs SCE. Time=30, 28, 26, 24, 22, 16, 14, 12, 10, and 0 hrs. (Top to Bottom).

Figure 4.2: Time evolution of the growth pattern from 1M $ZnSO_4$ at -1.05V vs SCE. Time=12, 11, 10, 9, 8, 7, 6, 5, 4, 3, 2, 1, and 0 hrs. (Top *to* Bottom).

for both concentrations, the initiation is similar to the mossy deposits but then the patterns grow in the form of trees with thick bark of metallic ash color. An example of the time evolution of this region from 1M solution at -1.12V vs. SCE is shown in figure 4.3. At somewhat more negative potentials, the patterns start to diverge between the two concentrations: initiating with island formation similar to the reported patterns of the computer simulation of dissolution precipitation[67], and then to thick finger type growth. A typical pattern from 1M electrolyte is shown in figure 4.4 at the applied potential -1.14V vs. SCE. The growth using 0.1M solution is well separated trees with thick stems.

The growth from both solution at -1.2V vs. SCE shown in figure 4.5 and 4.6. These structures are similar to that of Sawada et.al.[12] and are named as a homogeneous type.

At potential around -1.25V vs. SCE, patterns which are similar to the DLA patterns start to appear from both electrolytes. Figure 4.7 and 4.8 from 1M solution at -1.4V and -2.2V vs. SCE respectively, shows that the growth is DLA and remains unchanged at more negative potentials. For the 0.1M electrolyte, the patterns change dramatically as we go to more negative potentials, approaching at -1.6V vs. SCE a much more ordered space filling columnar type growth. A typical time evolution of growth at -2.0V vs. SCE is shown in figure 4.9. One might say that this morphology is similar to that reported for simulation of azimuthal ballistic deposition by Ramanlal and Sander[68]. However, in the ballistic simulation the growth is propagated at an angle to the path of the trajectories of the particles. But, in our experiment this angle is zero, therefore the mechanism of this type of growth may be different from the ballistic.

As described in section 2.3.1, we performed the current-potential

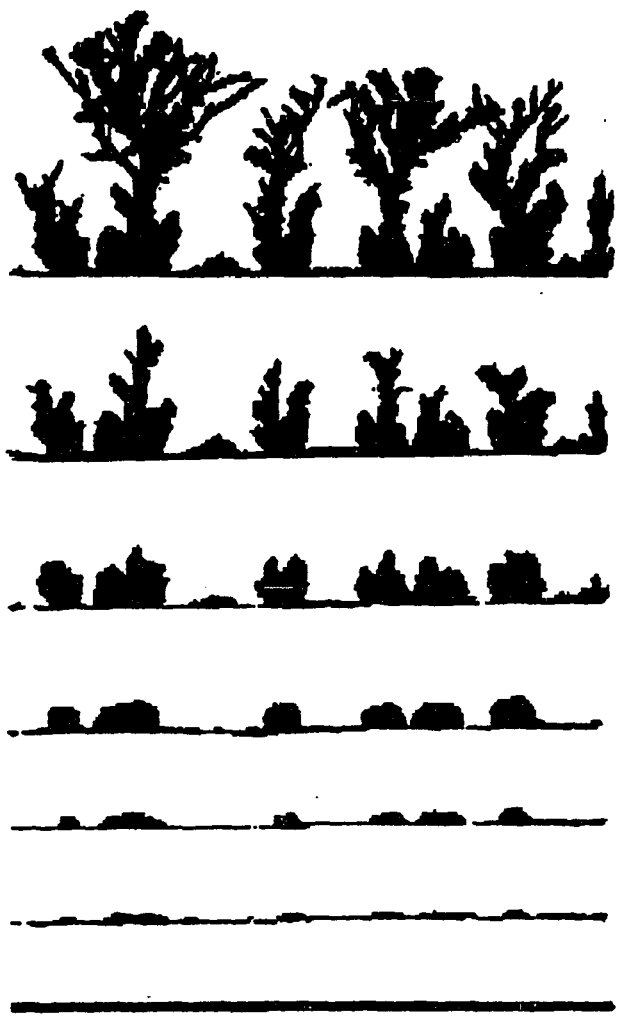

Figure 4.3: Time evolution of the growth pattern from 1M $ZnSO_4$ at -1.1V vs SCE. Time=60, 50, 40, 30, 20, 5, and 0 min. (Top to Bottom).

Figure 4.4: Time evolution of the growth pattern from 1M $ZnSO_4$ at -1.14V vs SCE. Time=7, 6, 5, 4, 3, and 0 min. (Top to Bottom).

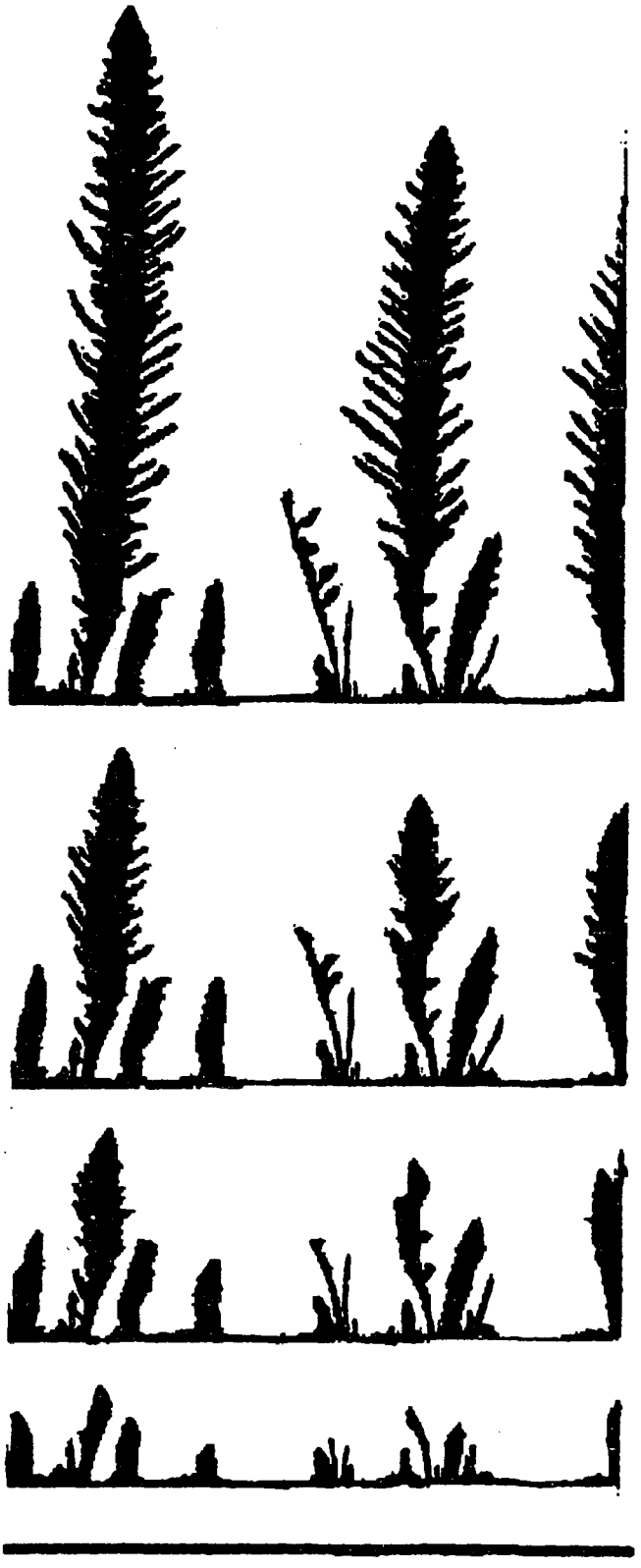

Figure 4.5: Time evolution of the growth pattern from 0.1M $ZnSO_4$ at -1.2V vs SCE. Time=20, 15, 10, 5, and 0 min.(Top to Bottom)

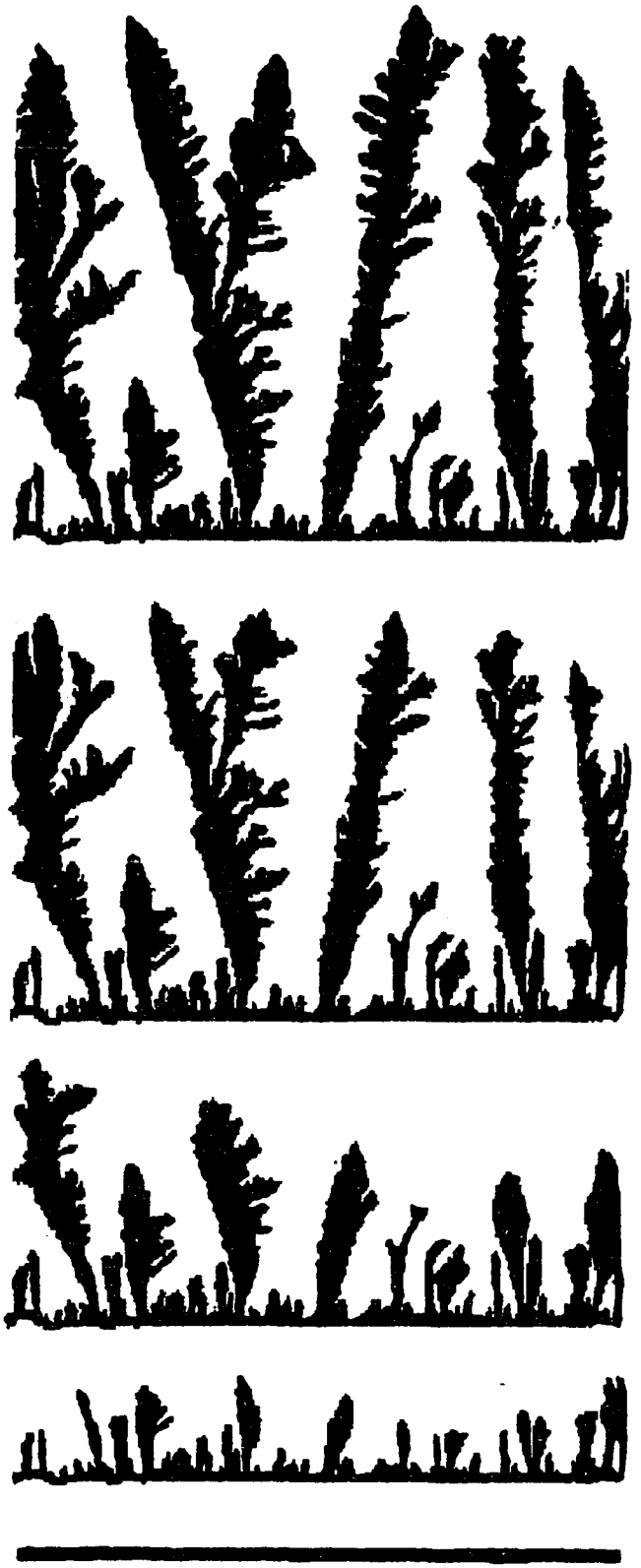

Figure 4.6: Time evolution of the growth pattern from 1M $ZnSO_4$ at -1.2V vs SCE. Time=35, 25, 15, 5, and 0 sec.(Top to Bottom).

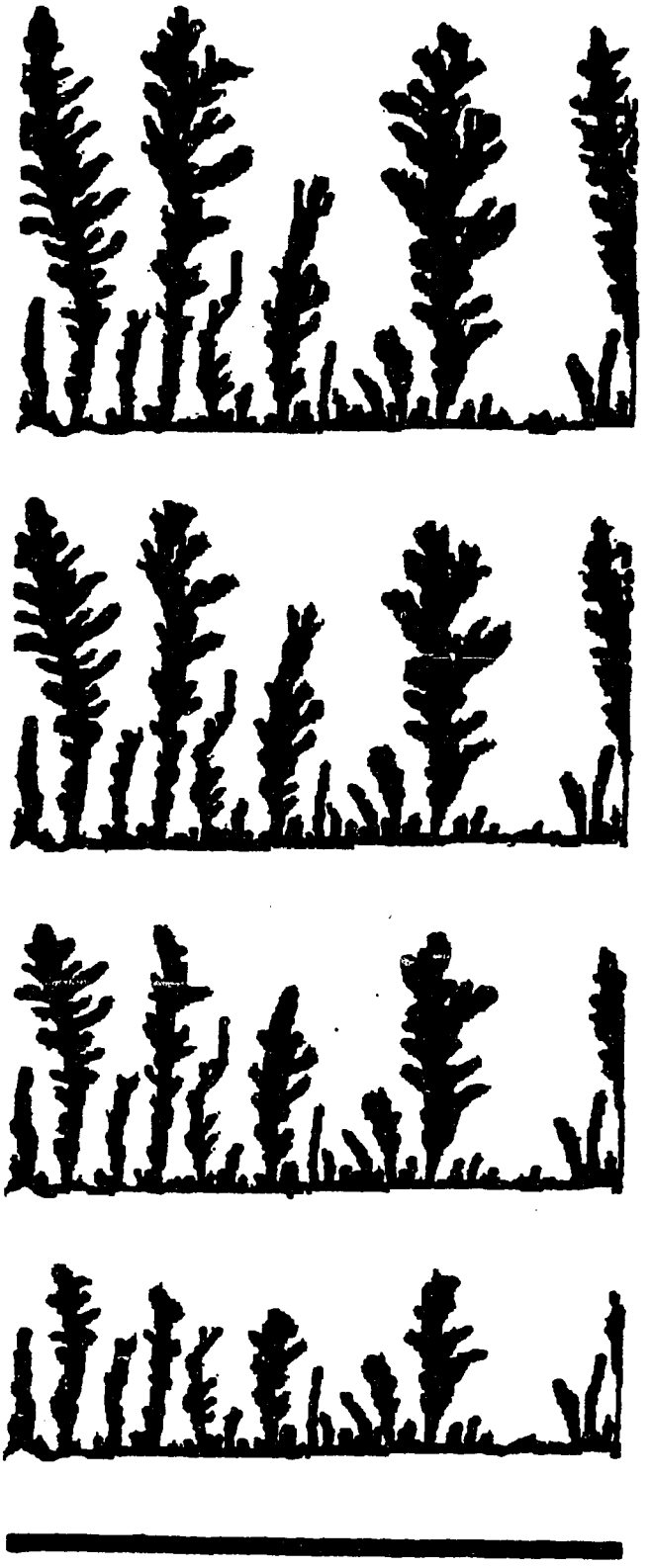

Figure 4.7: Time evolution of the growth pattern from 1M $ZnSO_4$ at -1.4V vs SCE. Time=20, 15, 10, 5, and 0 sec.(Top to Bottom).

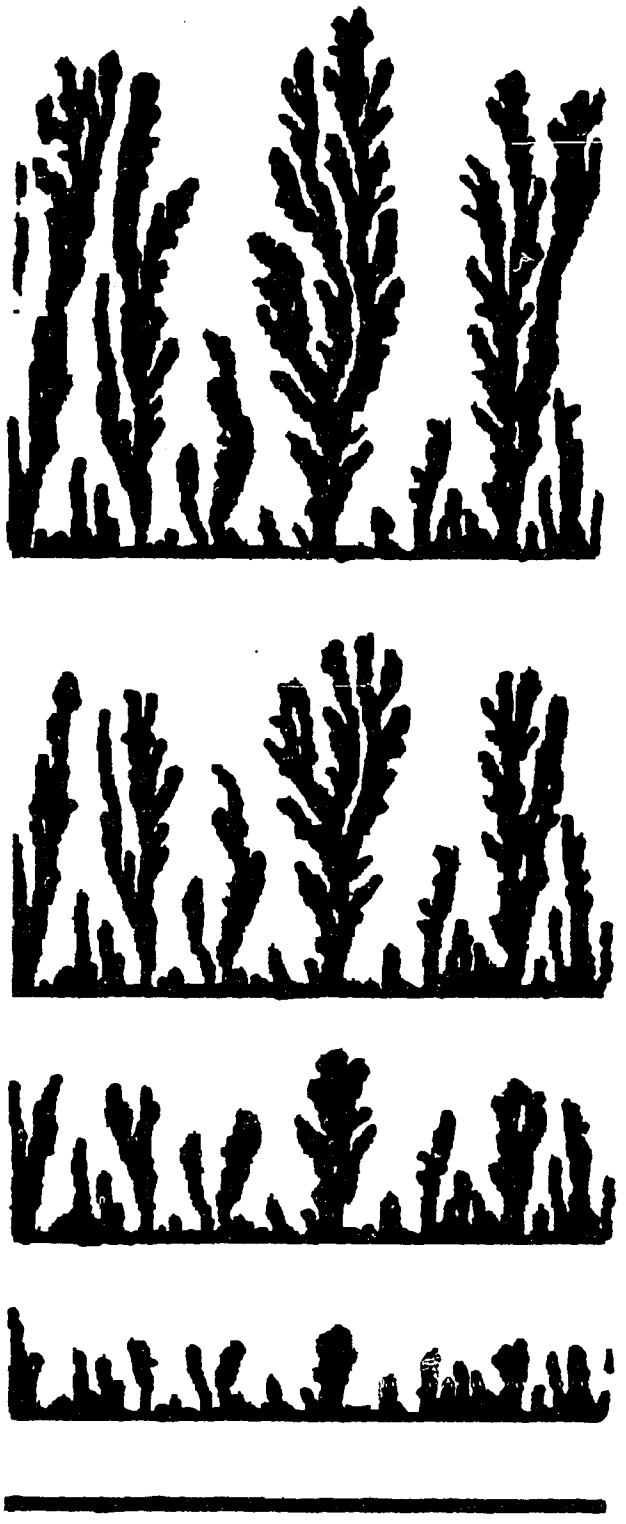

Figure 4.8: Time evolution of the growth pattern from 1M $ZnSO_4$ at -2.2V vs SCE. Time=4, 3, 2, 1, and 0 sec.(Top to Bottom).

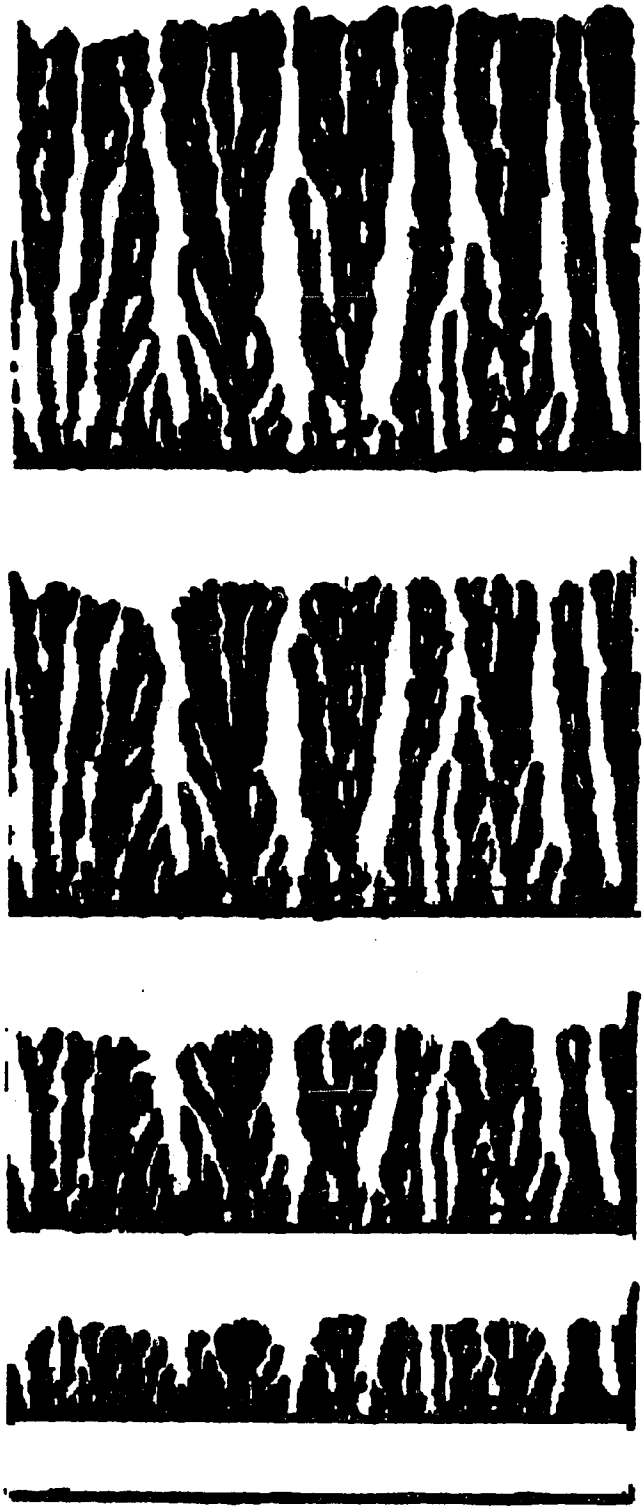

Figure 4.9: Time evolution of the growth pattern from 0.1M $ZnSO_4$ at -2.0V vs SCE. Time=4, 3, 2, 1, and 0 sec.(Top to Bottom).

measurement by linear sweep voltammetry at a sweep rate of 50 mV/sec. The results, both in terms of i and I, are shown in figure 4.10 and 4.11. The limiting current in the two solutions are I_l=5.2 mA/s$^{1/2}$ for the 1M solution and I_l=1.7 mA/s$^{1/2}$ for the 0.1M solution. The ratio of the limiting current is smaller than the ratio of their concentrations, but this can be accounted for by the difference in the corresponding activity coefficients. The application of the semi-integral current takes into account the time dependence of the electrode potential but not the evolution of the surface area. The geometric surface area of the substrate is measured as 0.003 cm^2. Taking the diffusion constant of the electrolyte as 5x10^{-6} cm^2/sec and using the concentrations, as we mentioned in the section 2.3.1 , we can calculate an "effective" area for the current limiting condition. These are 0.02cm^2 for the 1M solution and 0.08cm^2 for the 0.1M solution. The linear fit to equation 2.18 is shown in the inserts to figure 4.10 and 4.11, with the following parameters; taking n=1[69], α=0.58 in both solution and i_0=1.2mA/cm^2 for the 1M solution and one order of magnitude smaller for the 0.1M solution. The value of α strongly suggests that the current rise in this potential range is due to activation and not due to the increase in the surface area. The limiting currents also are in approximate agreement with the literature values for zinc deposition in a three dimensional cell[70]; although, the absence of a supporting electrolyte, for reasons that will be explained shortly, makes any comparison tenuous at best.

The kinetics approaches the diffusion limited current at potentials negative of -1.3V vs. SCE for both electrolytes.

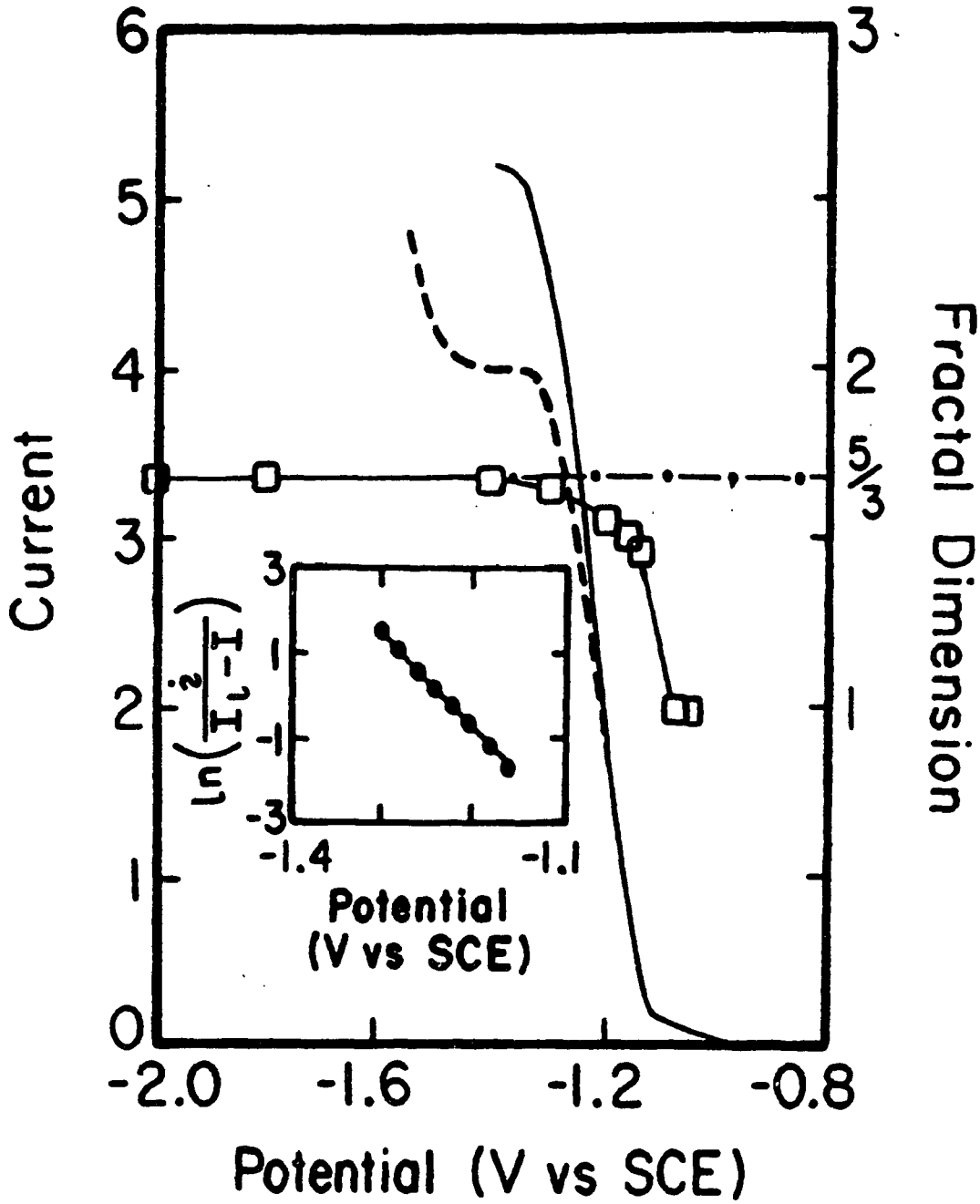

Figure 4.10: Dependence of the semi-integral current (solid line) and the current (dash line) (left scale) and the contour length fractal dimension (right scale) on the electrode potential. Insert - fit of Eq. 2.18 to the experimental results of 1M $ZnSO_4$.

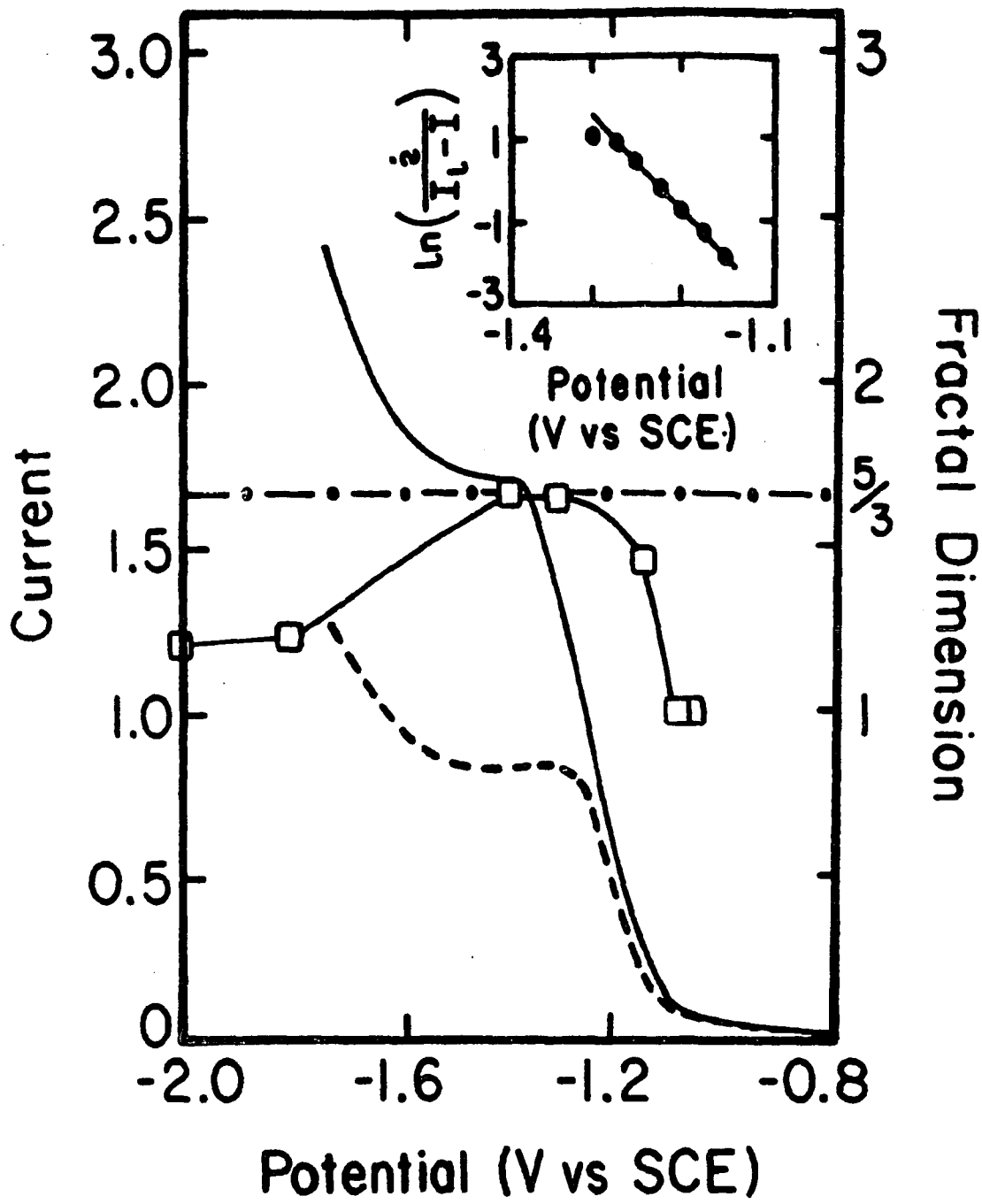

Figure 4.11: Dependence of the semi-integral current (solid line) and the current (dash line) (left scale) and the contour length fractal dimension (right scale) on the electrode potential. Insert - fit of Eq. 2.18 to the experimental results of 0.1M $ZnSO_4$.

The fractal dimension of the deposits is analyzed by using the three methods described in section 2.2. The plots in figures 4.12, 4.13, and 4.14 show a typical behavior from: correlation, sandbox and contour length method respectively. Typical cutoffs in which the fractal scaling is applicable are 10 pixels and the average height of the precipitate. The variation of the contour length dimension with potential is also shown in figure 4.10 and 4.11. At the potentials negative of -1.3V vs. SCE the fractal dimension converges to the DLA value 5/3. In this regime, the pattern is self-similar in the sense that the branch is similar to the tree. The contour length plot of a branch and a the tree is shown in figure 4.15. The contour length fractal dimension rises from 1 at low overpotentials which describes the approximate smooth interface of the mossy deposit to the DLA value at the higher overpotentials.

The behavior of the 0.1M electrolyte is similar to that of the 1M solution for potentials positive to -1.4V vs. SCE. At more negative potentials growth is columnar, probably due to the expected increase in the contribution of electromigration to the conduction processes in the electrolyte. This will be discussed in the next chapter with the studies of the silver system.

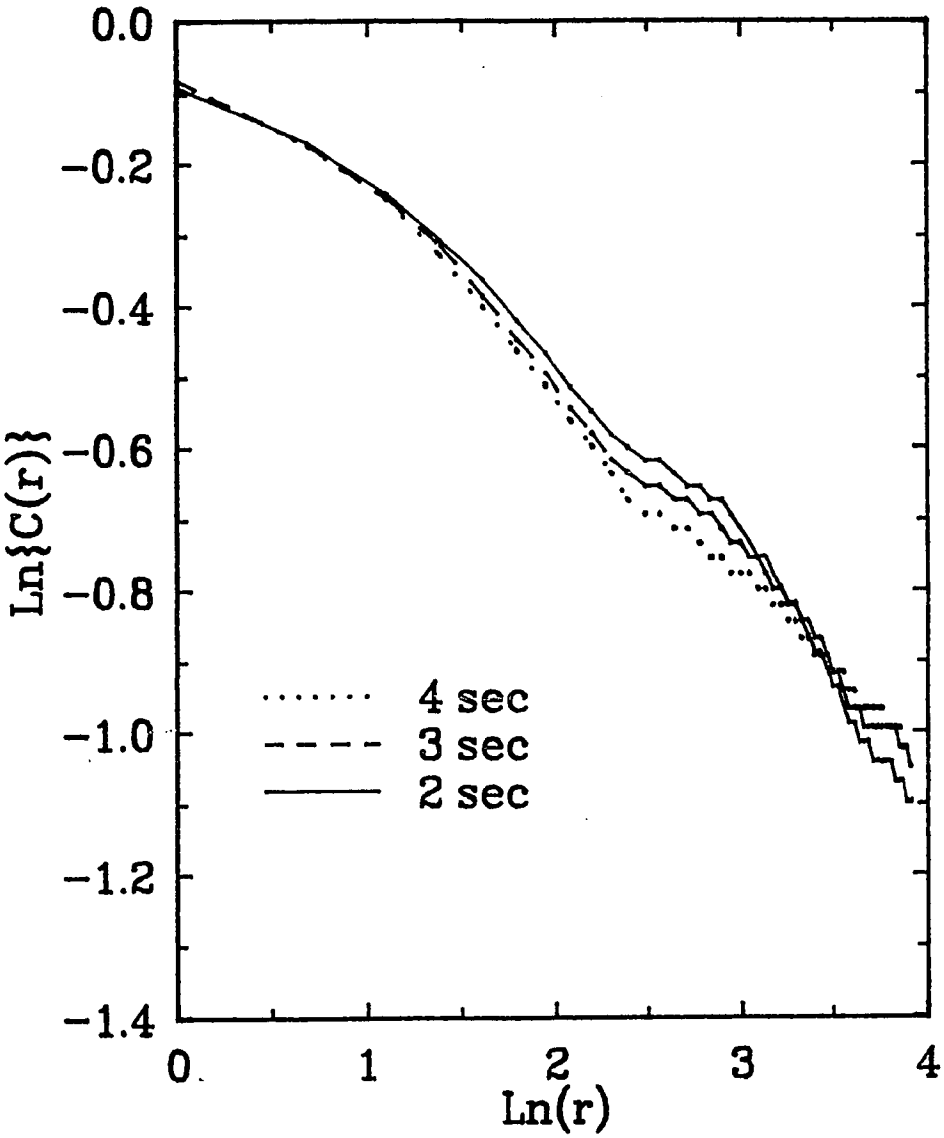

Figure 4.12: Pair-correlation plot of the growth shown in Fig. 4.8.

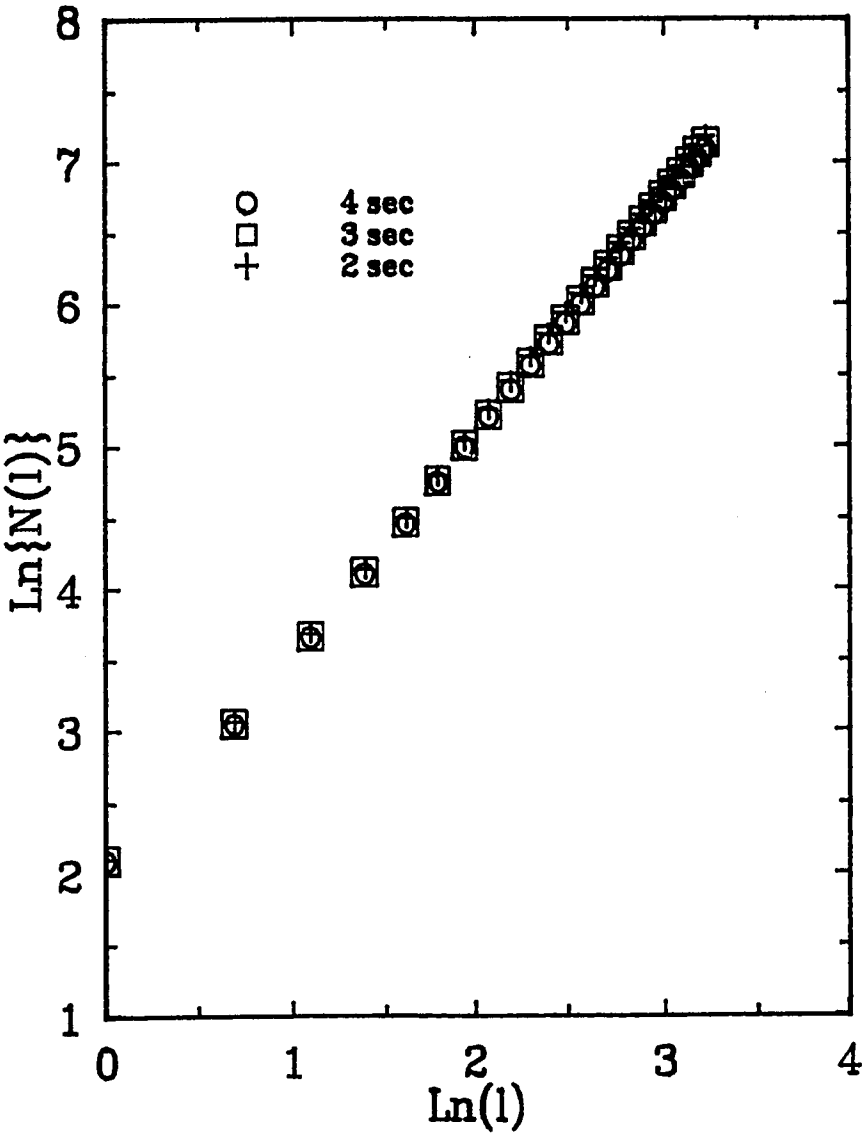

Figure 4.13: Sandbox plot of the growth shown in Fig. 4.8.

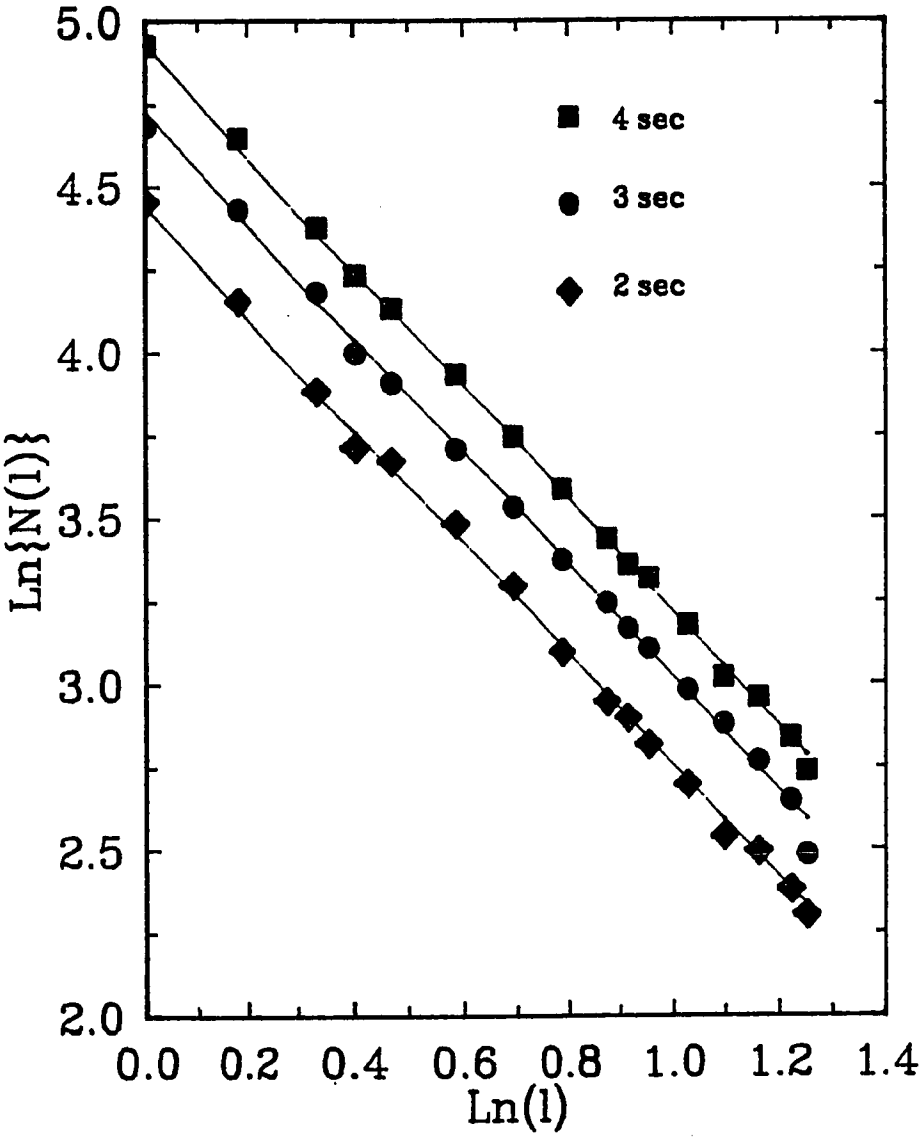

Figure 4.14: Contour length plot of the growth shown in Fig. 4.8.

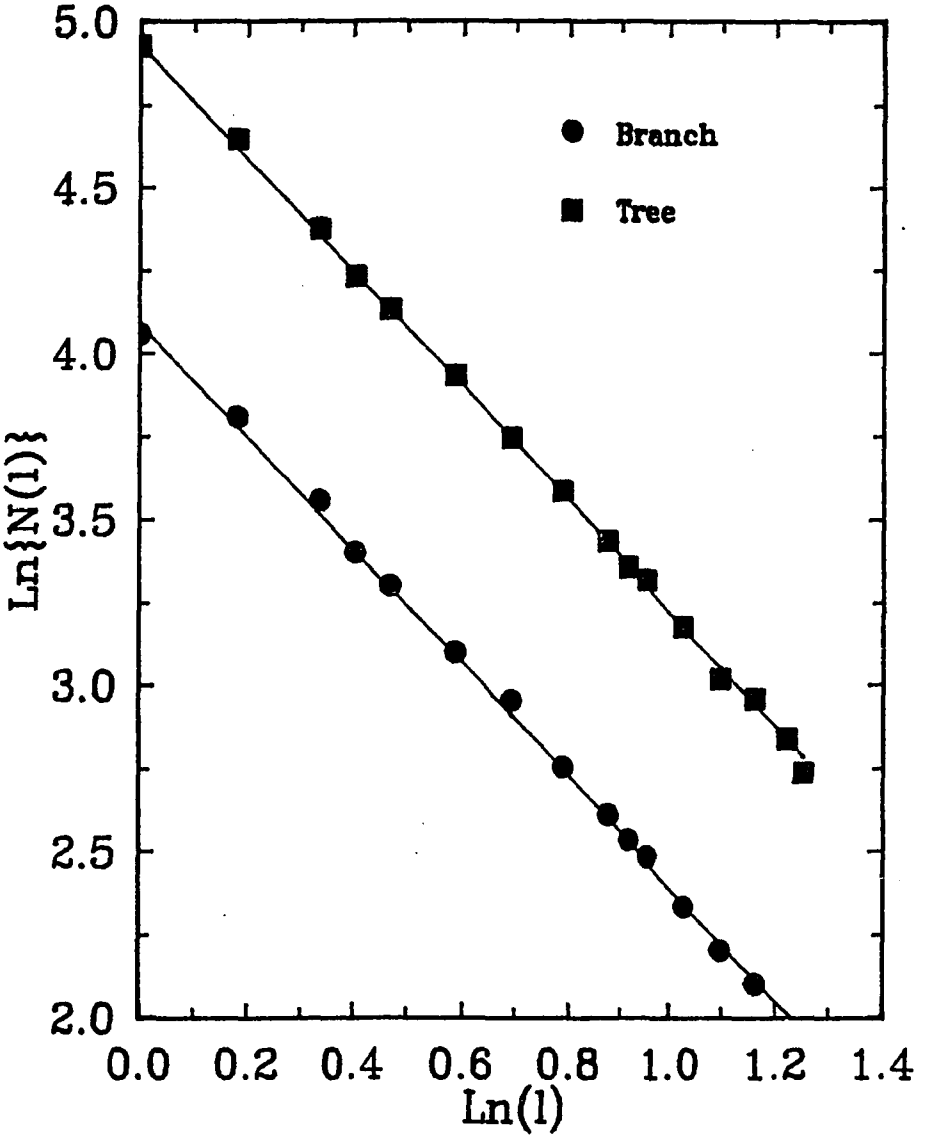

Figure 4.15: Self-similarity of a branch and a tree of a tree taken from Fig. 4.8 at 4 sec.

One can show that for compact, smooth and uniform deposits, the current should be linear with $t^{-1/2}$ and the height of the deposit is linear with $t^{1/2}$[71]. Figure 4.16 shows the time variation of the average thickness of the deposit as a function of potential for the 1M electrolyte. Within the time limits shown here the velocity is constant. The variation of the velocity with potential is shown in the figure 4.17. The velocity saturates as we reach the mass transfer limiting conditions.

An example of the current time behavior at the potential of -1.8V vs. SCE is shown in figure 4.18. The general shape is reminiscent of the Abyaneh and Fleischmann treatment for nucleation growth[72]. The initial growth was treated in terms of "instantaneous", two dimensional, nucleation given by

$$I = \left(\frac{2zF\pi hMN_0k_{2c}^2t}{\rho}\right) \exp\left(\frac{-\pi M^2N_0k_{2c}^2t^2}{\rho^2}\right) \qquad (4.1)$$

where z is the charge number of the electrode reaction, F is the Faraday constant, h is the height of a monolayer, M is the molar mass, N_0 is the number of nuclei formed instantaneously, k_{2c} is the two dimensional growth rate constant parallel to the surface. Figure 4.18 shows that this equation fits the initial growth up to about 1 sec., with the following parameters: $N_0 k_{2c}=0.008$ $mol^2cm^{-6}s^{-2}$ and $h=0.43A^o$. After about 2 sec., the growth shifts to three dimensional "progressive" nucleation and growth given by

$$I = zFk_{3c}'\left\{1 - \exp\left[\left(\frac{-\pi M^2k_{3c}^2A_3}{3\rho^2}\right)(t-\tau)^3\right]\right\} \qquad (4.2)$$

where k'_{3c} is the three dimensional growth rate perpendicular to

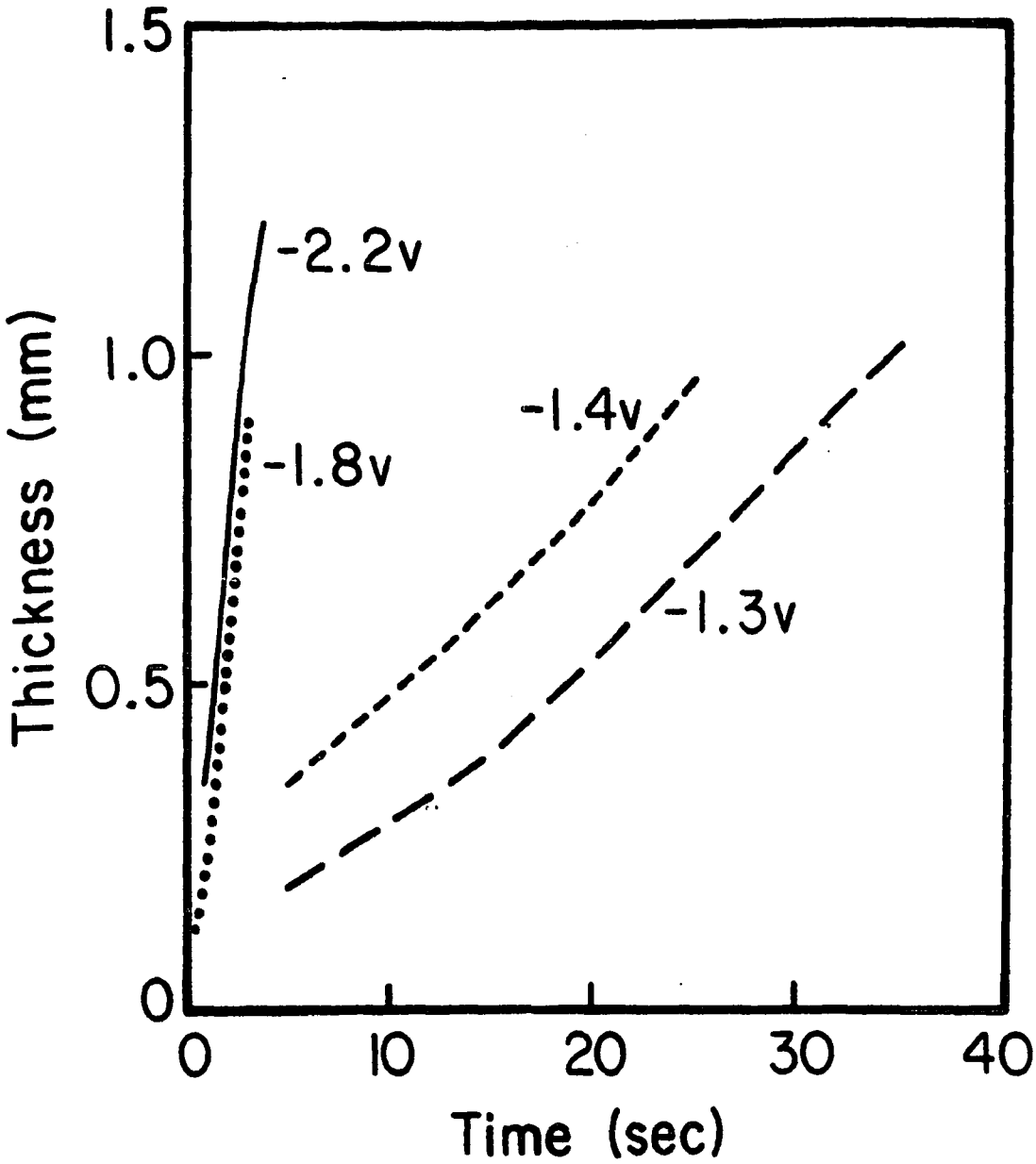

Figure 4.16: Time evolution of the average thickness of the deposit from 1M $ZnSO_4$ solution. Deposition potentials are given in the figure.

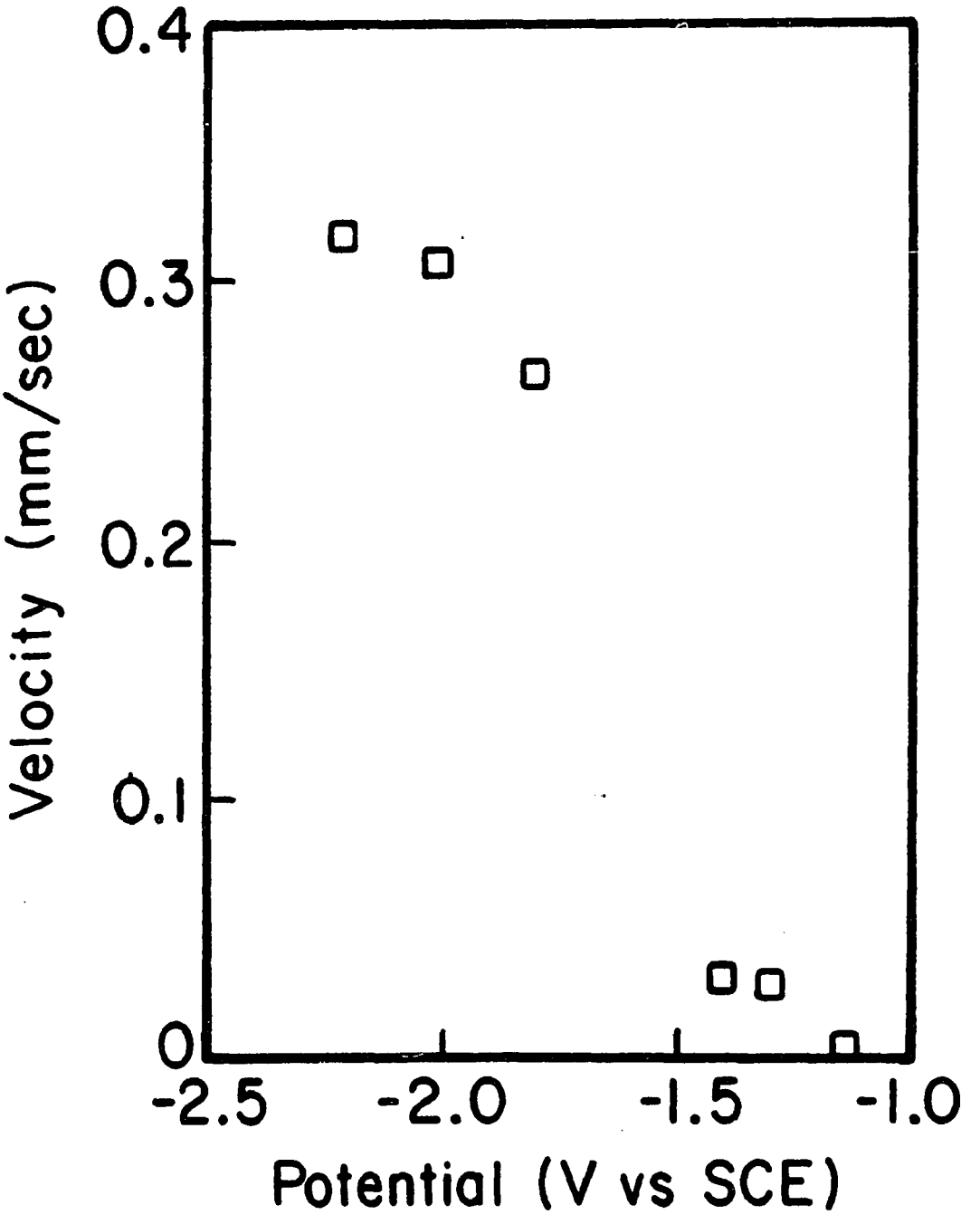

Figure 4.17: Variation of the growth velocity with potential for the 1M $ZnSO_4$ solution.

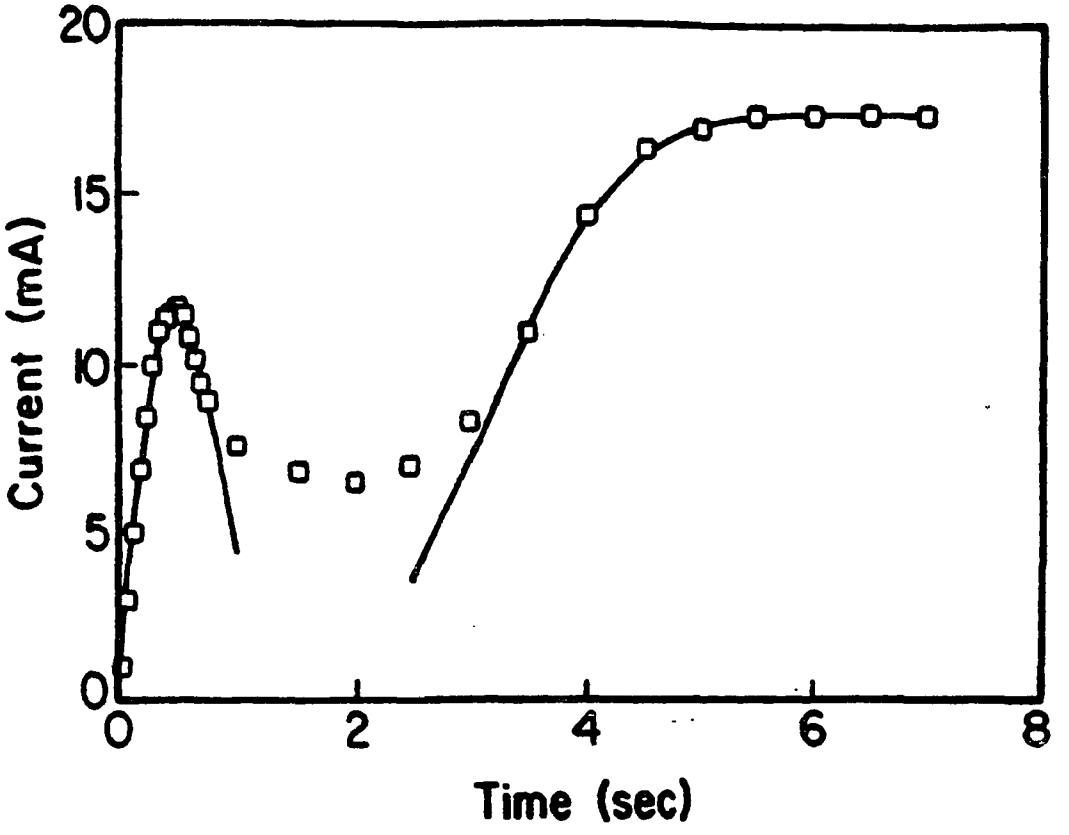

Figure 4.18: The current-time behavior at the potential of -1.8V vs SCE for deposition from 1M $ZnSO_4$. Squares = Experiment, Solid line = Theoretical fit to Eqn. 4.1 and 4.2.

the surface, k_{3c} is the three dimensional growth rate parallel to the surface, A_3 is the three dimensional nucleation rate constant, and τ is the induction period for the start of the three dimensional growth. Figure 4.18 shows the fit of equation 4.2 to the experimental data with the following parameters: $zFk'_{3c}=5.8Acm^{-2}$ (taking the area as the geometric area of the substrate), $k_{3c}A_3=4.6x10^{-5}mol^2cm^{-6}s^{-3}$, and $\tau=0.95sec$. The rate constants are different from those reported by McBreen and Gannon[69] for the nucleation of zinc from 3M $ZnCl_3$ solutions but so are the growth conditions. These constants should be taken only as an empirical fit. The theory is based on the evolution of the surface area of hemispherical nuclei which is obviously different from the present morphology. A development of a similar theory, that will take into account a more realistic description of the morphology is urgently needed.

At an electrode potential closer to the equilibrium potential, a region in which the morphology is dominated by the mossy deposit, the current-time behavior shows an oscillatory structure superimposed on the d.c. behavior. This is shown in figure 4.19 with the oscillations shown on an expanded scale in the insert. The Fourier transformation of these oscillations is analyzed to yield a frequency spectrum with a maximum at 2Hz. These oscillations can be explained in terms of the competition between the zinc deposition and the hydrogen evolution of the reaction[73]. This issue takes much grater importance with the addition of a supporting electrolyte that will be discussed next.

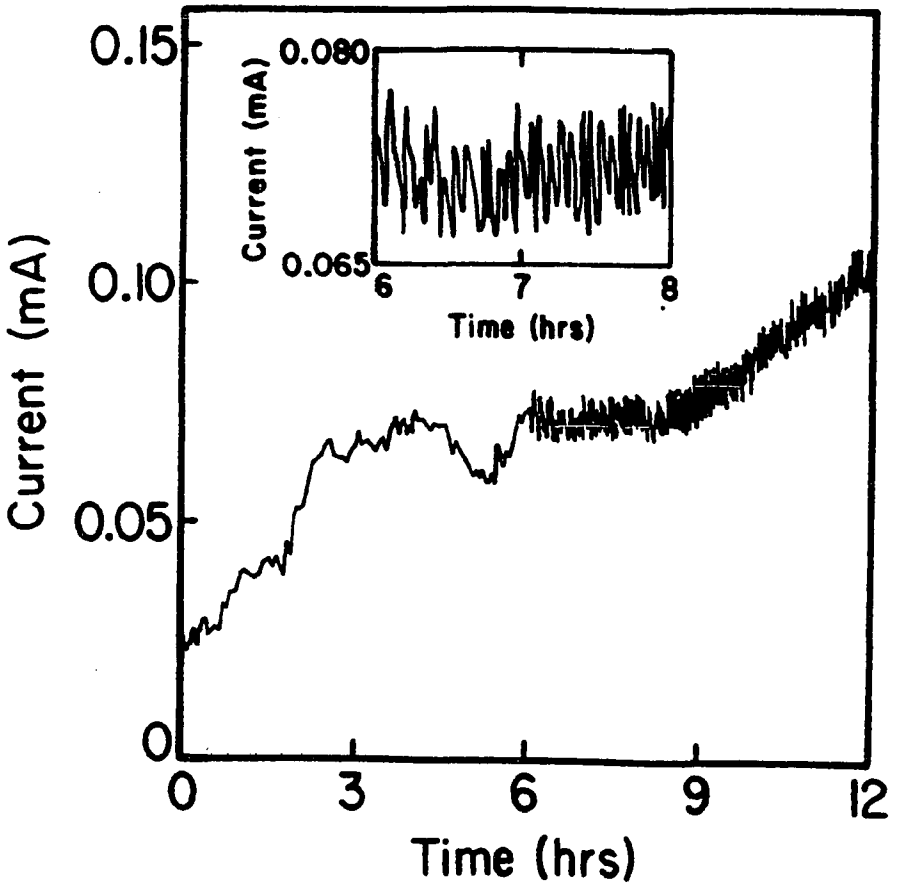

Figure 4.19: The current-time behavior at the potential of -1.05V vs SCE for deposition from 1M $ZnSO_4$. Inset is magnification of the oscillations.

4.1.3. With Supporting Electrolytes.

The evolution of the morphology with applied potential was analyzed in the following systems:

1. 0.1M $ZnSO_4$ in 1M Na_2SO_4
2. 0.1M $ZnSO_4$ in 1M H_2SO_4
3. 0.1M $ZnCl_2$ in 1M KCl
4. 0.1M $ZnCl_2$ in 1M HCl
5. 0.1M ZnO in 3M KOH

Typical results of the time evolution of the growth morphologies at three different potentials are shown in figure 4.20, for the system 0.1M $ZnSO_4$ in 1M Na_2SO_4. At longer times and/or more negative potentials, hydrogen evolution takes over in the interior of the pores and the bubbles destroy the growth. These observations are independent of the system tested and independent of the substrate on which the growth takes place. The hydrogen evolution with the supporting electrolyte can be explained as follows: as the growth front propagates the interior of the growth suffer a lack of active (Zn^{+2}) ions, however, the supporting electrolyte ions play the role of keeping the potential at the interior region at the applied value. The only reaction that can takes place to counter balance this potential is the hydrogen evolution.

The growth patterns are different from those observed without the supporting electrolyte. After the mossy initiation which is common, we observed that the pattern grows with a highly correlated front. We could not reach the DLA regime with any of the systems that are tested under these conditions. As an example, the thickness-time behavior of 0.1M $ZnSO_4$ in 1M Na_2SO_4 is shown in figure 4.21. It shows a power law

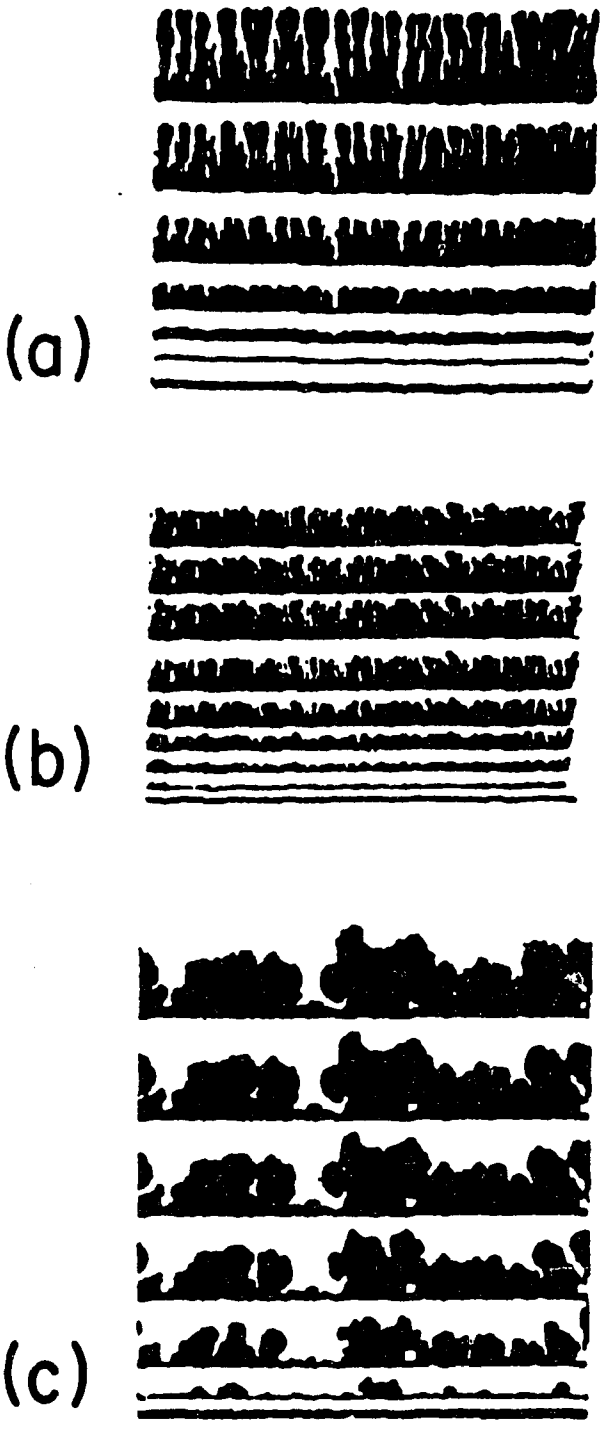

Figure 4.20: Typical examples of time evolution of the growth patterns of zinc deposited from 0.1M $ZnSO_4$ in 1M Na_2SO_4 solution at various electrode potentials. a). -1.3V vs SCE b). -1.2V vs SCE c). -1.1V vs SCE.

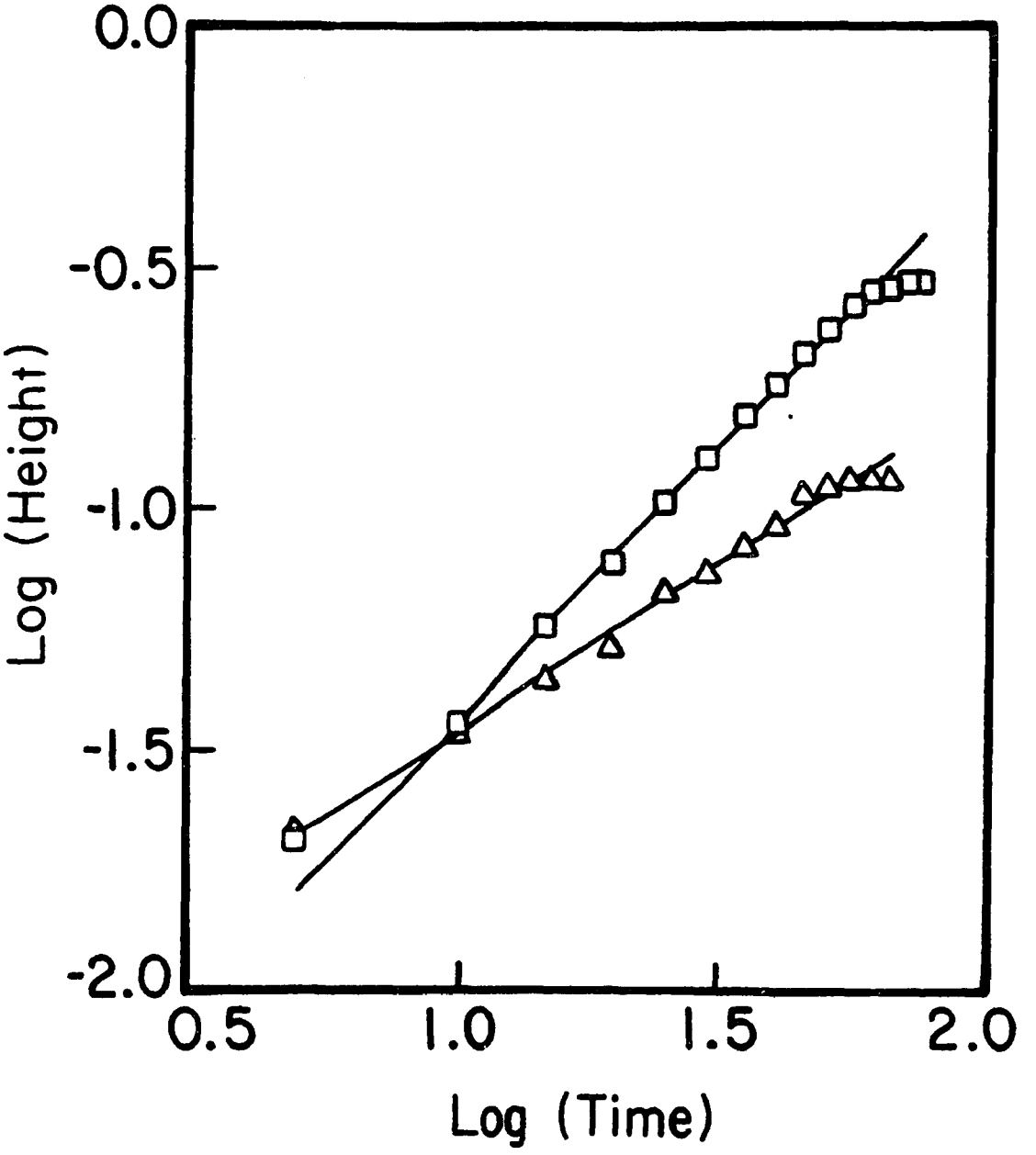

Figure 4.21: Time evolution of the height for deposits from the same solution as Fig. 4.20. Squares = -1.3V vs SCE, Triangles = -1.2V vs SCE, height in mm and time in sec.

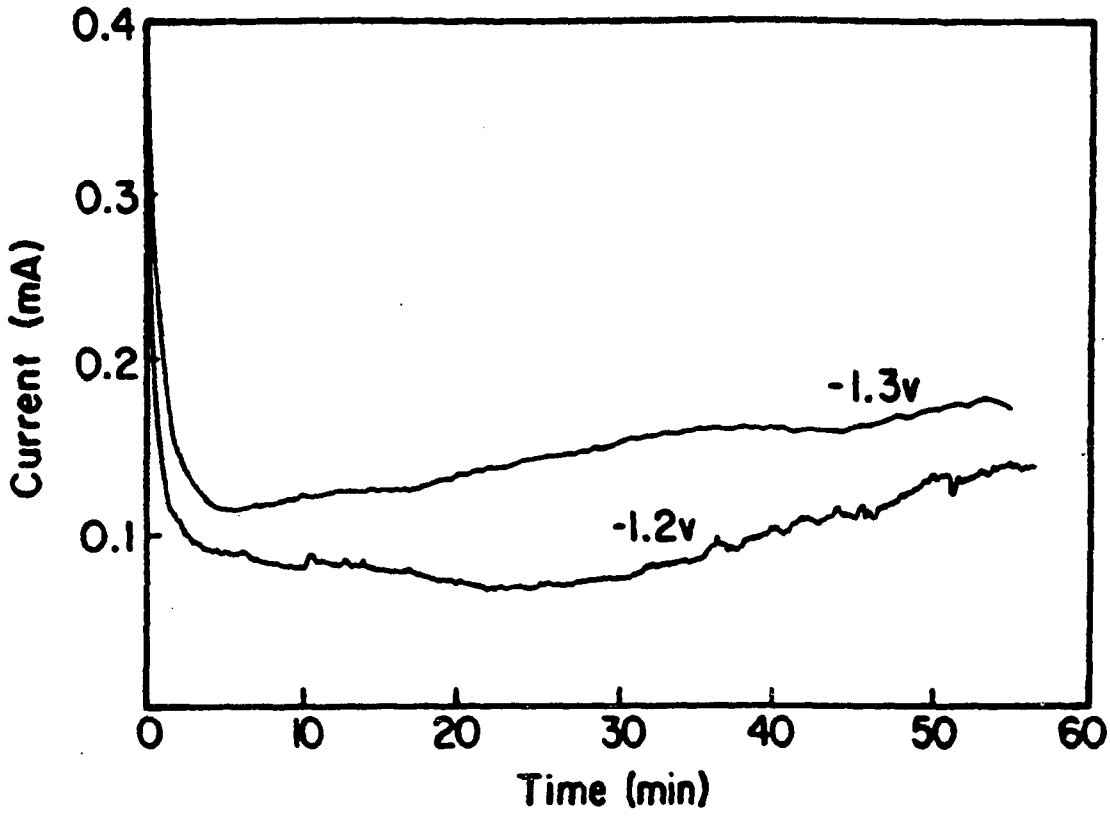

Figure 4.22: Current-time behavior for deposition from the same solution as in Fig. 4.20. Potentials specified in the figure.

behavior with a potential dependent exponent. The current-time behavior is shown in figure 4.22. Within the measured range, the current is approximately constant and roughly resembles the d.c. component of the current-time behavior of the 1M Zn electrolyte shown in figure 4.19.

The hydrogen evolution in the zinc system is largely due to the fact that the equilibrium potential of zinc, -1.0083V vs. SCE, and the hydrogen over potential in aqueous solution, -1.0638V vs. SCE, is much closer to each other. To overcome the hydrogen evolution problem, one can search for another system in which the equilibrium potential should be far away from the H_2 potential. The silver, which has E_0 at +0.603V vs. SCE (+0.5584V vs. Ag/AgCl) might be the best system to explore in this study.

In the next chapter, we will present our observation of the silver system in the presence of a supporting electrolyte. We will also discuss the effect of the diffusion-migration ratio on the growing interface.

4.2. Silver System

The main premise in this section is to study the effect of the supporting electrolyte and hence to see the effect of diffusion-migration ratio on growing structures. One of the major observations we see with the zinc system is that new kinds of thick, columnar type structure arise from the non-supporting, low ionic solution.

We can estimate the migration component of any system in two different ways. The first method, by assuming the equal conductivity throughout the cell for each ion, one can calculate[35] the transference number, t_j, of the j^{th} ion,

$$t_j = \frac{|z_j| c_j \lambda_j}{\sum_k |z_k| c_k \lambda_k} \tag{4.3}$$

which is related to the migration current I_m by,

$$I_m = \pm \frac{n}{z_j} t_j i \tag{4.4}$$

where λ_j is the conduction of the j^{th} ion, c_j is the concentration of the j^{th} ion, n is the number electron represents in the single charge transfer process and i is the total current of the system.

The second method is more general than the first method. Here we solve the diffusion equation including the migration part as proposed by Hsuses and Newman[74]. We write the diffusion equation for three ions

in our system as,

$$N_1 = - z_1 u_1 F c_1 \frac{d\Phi}{dx} - D_1 \frac{dc_1}{dx} = \frac{i}{z_1 F} \tag{4.5}$$

$$0 = - z_2 u_2 F c_2 \frac{d\Phi}{dx} - D_2 \frac{dc_2}{dx} \tag{4.6}$$

$$0 = - z_3 u_3 F c_3 \frac{d\Phi}{dx} - D_3 \frac{dc_3}{dx} \tag{4.7}$$

and the electroneutrality condition,

$$z_1 c_1 + z_2 c_2 + z_3 c_3 = 0 \tag{4.8}$$

where i=1,2,3 stands for Ag^+, NH_4^+, NO_3^- respectively and D_i, c_i, u_i, z_i are the diffusion coefficient, concentration, mobility and charge of the i^{th} ion.

Using the boundary condition,

$$c_2 = c_2^\infty \ , \ c_3 = c_3^\infty \ , \ \phi = 0 \quad \text{at } x = \delta \tag{4.9}$$

where δ is the diffusion layer thickness, we arrived at,

$$\frac{I_m}{I_l} = 1 - \left[\frac{(1 - r)}{2(1 - \sqrt{r})}\right] \tag{4.10}$$

where I_l is the limiting current and $r = c^\infty(NH_4^+)/c^\infty(NO_3^-)$.

4.2.1. Preparation:

The working electrode used in this study is a microstop painted, one edge open, silver foil of 25μm thick with $0.003cm^2$ area exposed to the solution. The counter electrode is a silver rod of 7mm diameter immersed into the solution in the counter electrode compartment. A

microstop painted Platinum foil of same thickness as the silver foil saved as a spacer.

A double junction Silver/Silver chloride electrode with internal saturated KCl solution and external 1M KNO_3 solution was used as a reference electrode.

The electrolyte solutions are prepared with deionized water and analytical grade $AgNO_3$, NH_4NO_3 and KNO_3.

4.2.2. Results and Discussion:

We have investigated the following systems:

a). 1M $AgNO_3$

b). 0.1M $AgNO_3$ / 0.5M NH_4NO_3

c). 0.01M $AgNO_3$ / 0.5M NH_4NO_3

d). 0.05M $AgNO_3$ / 1M KNO_3

Figure 4.23 shows the variation of the contour length fractal dimension with the applied potential for these systems. As in the zinc system, at the activation region the growth is mossy type. Then the growth from 1M solution goes through the DLA-like structures around the potential 0.45V vs. Ag/AgCl with d_f=1.60, to well separated, columnar type structures at high potentials, thus, reducing the contour length dimension. The second system, 0.1M $AgNO_3$/NH_4NO_3 also goes through the DLA type region with d_f=1.64, and then to more dense type growth at higher potentials as shown in figure 4.24. Also in figure 4.24, we present a collection of time evolution of growth from (b) at potentials 0.4, 0.3, 0.2, 0.1, 0.0V vs. Ag/AgCl. Figure 4.25 shows how the LSV and CLSV curves behave for the system (b). The DLA like patterns appears at the potential around 0.2V vs. Ag/AgCl, where the convolution currents start to saturate. The behavior of the systems (c) and (d) are

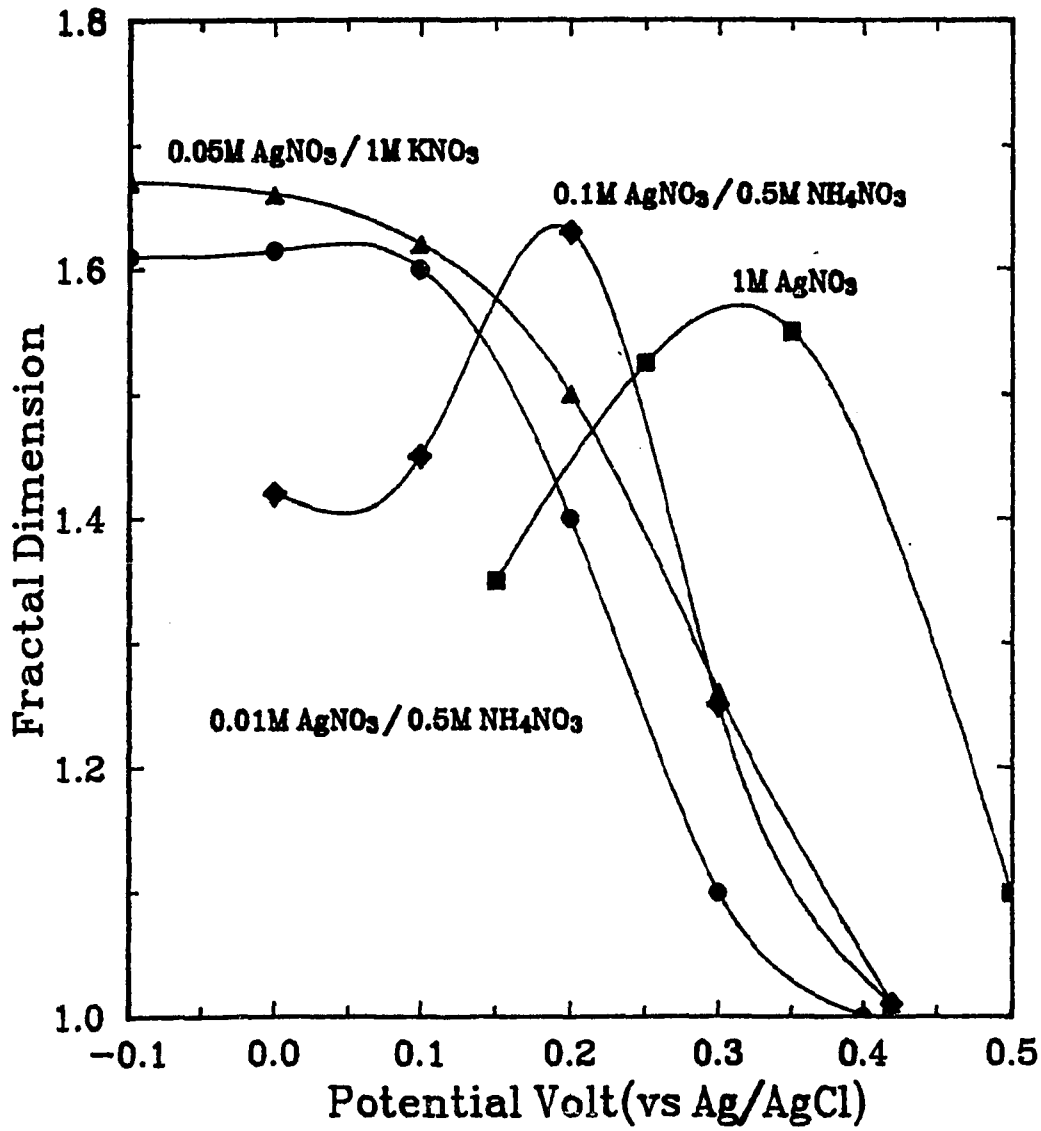

Figure 4.23: Variation of the surface fractal dimension with potential for the silver systems specified in the figure.

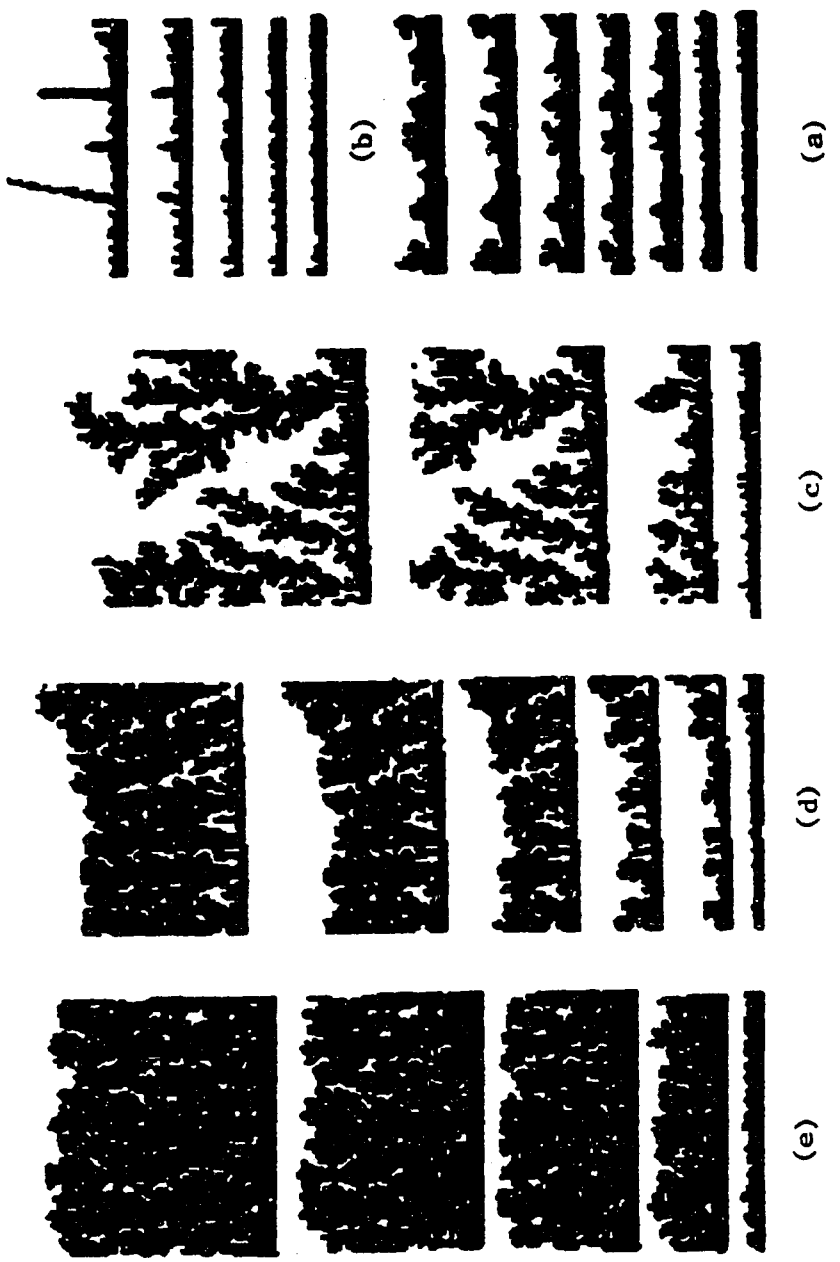

Figure 4.24: Time evolution of the growth patterns of silver deposited from 0.1M $AgNO_3$ in 0.5M NH_4NO_3 solution at various electrode potentials: (a). 0.4V (b). 0.3V (c). 0.2V (d). 0.1V (e). 0.0V vs Ag/AgCl.

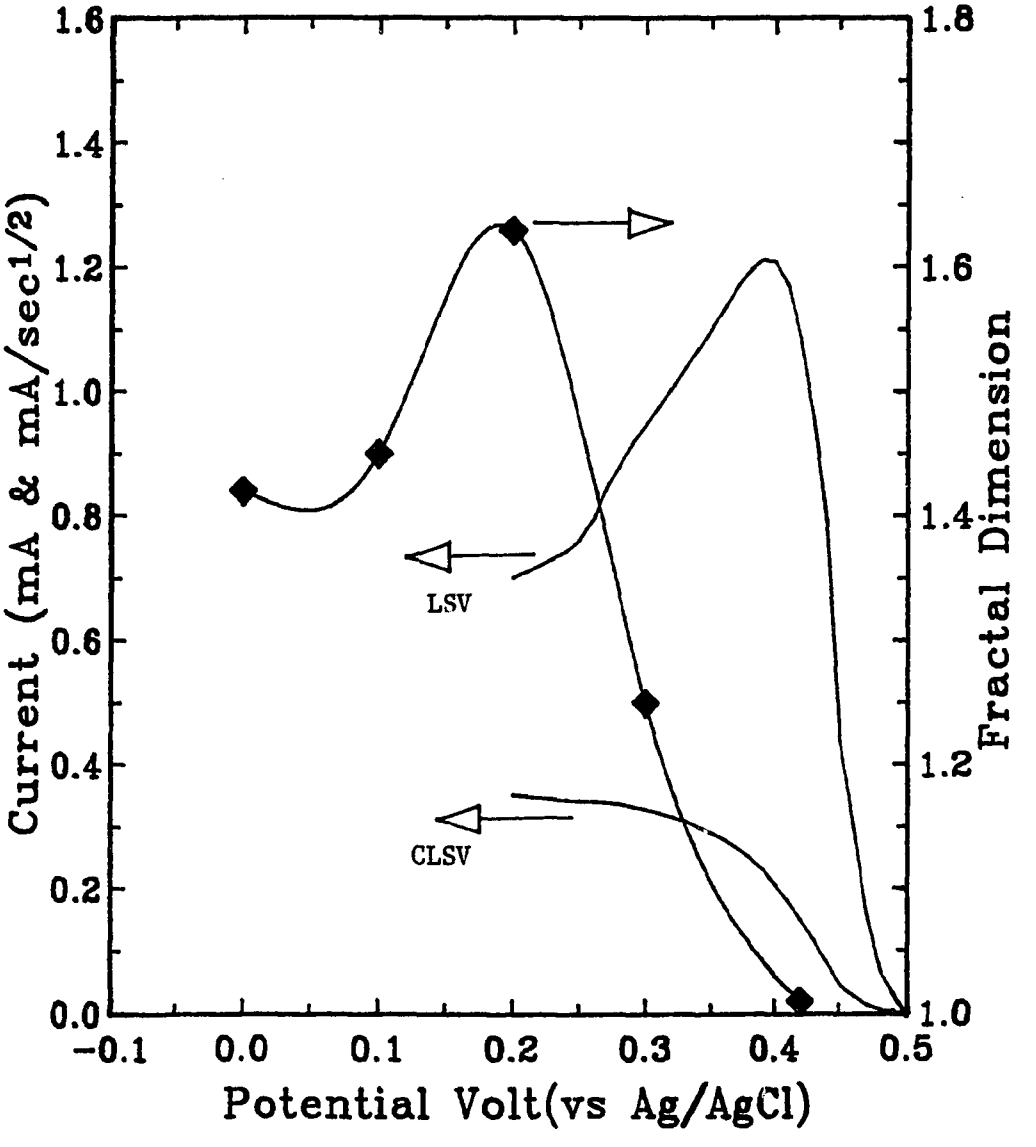

Figure 4.25: Dependence of the semi-integral current, the current and the surface fractal dimension for the system in Fig. 4.24; each curve specified in the figure.

similar to that of 1M Zinc system at higher potentials. As an example, the time evolution of growing structures at different potentials for the system (d) are shown in figure 4.26.

Although the system (c) behaves like a diffusion-limited at higher potentials, but, when the supporting electrolyte is not present, a new kind of growth is observed as shown at three different potentials in figure 4.27. One could assume that this is due to the migration of the Ag ions; therefore we have selected the system 0.01M $AgNO_3$ to study the effect of the diffusion-migration ratio on the growth. Figure 4.28 shows a collection of the time evolution growth patterns from the systems 0.01M $AgNO_3$ in xM NH_4NO_3 at 0.1V vs. Ag/AgCl. The value of x is varied from 0 to 1.

Calculated values of I_m% by both methods as discussed at the beginning of the section are shown in table 4.1. It is evident from the table 4.1, that I_m values from both methods are not significantly different; therefore, one can use either set to interprets the observations.

As we can see from table 4.1 and figure 4.28, at zero supporting electrolyte migration and diffusion each have 50% contribution to the total reaction this results in columnar type growth. However, as we increase the supporting electrolyte concentration, the migration component is reduced and the growth front starts to branch out. Finally, at the 1M supporting electrolyte concentration, the diffusion is the dominating mechanism over the migration where we observe the DLA-like structures.

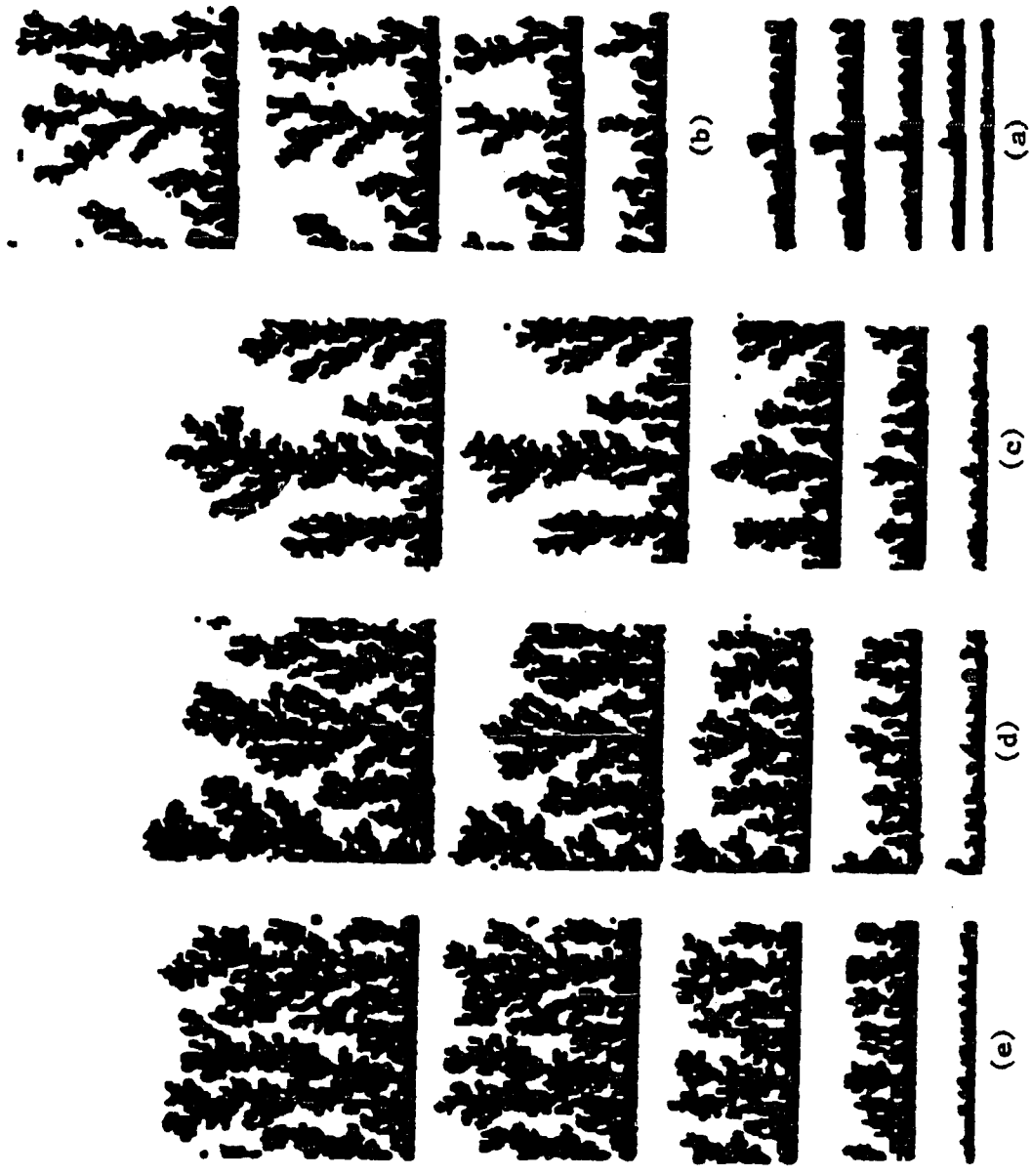

Figure 4.26: Time evolution of the growth patterns of silver deposited from 0.05M $AgNO_3$ in 1M KNO_3 at various potentials: a). 0.42V b). 0.2V c). 0.1V d). 0.0V e) -0.1V vs Ag/AgCl.

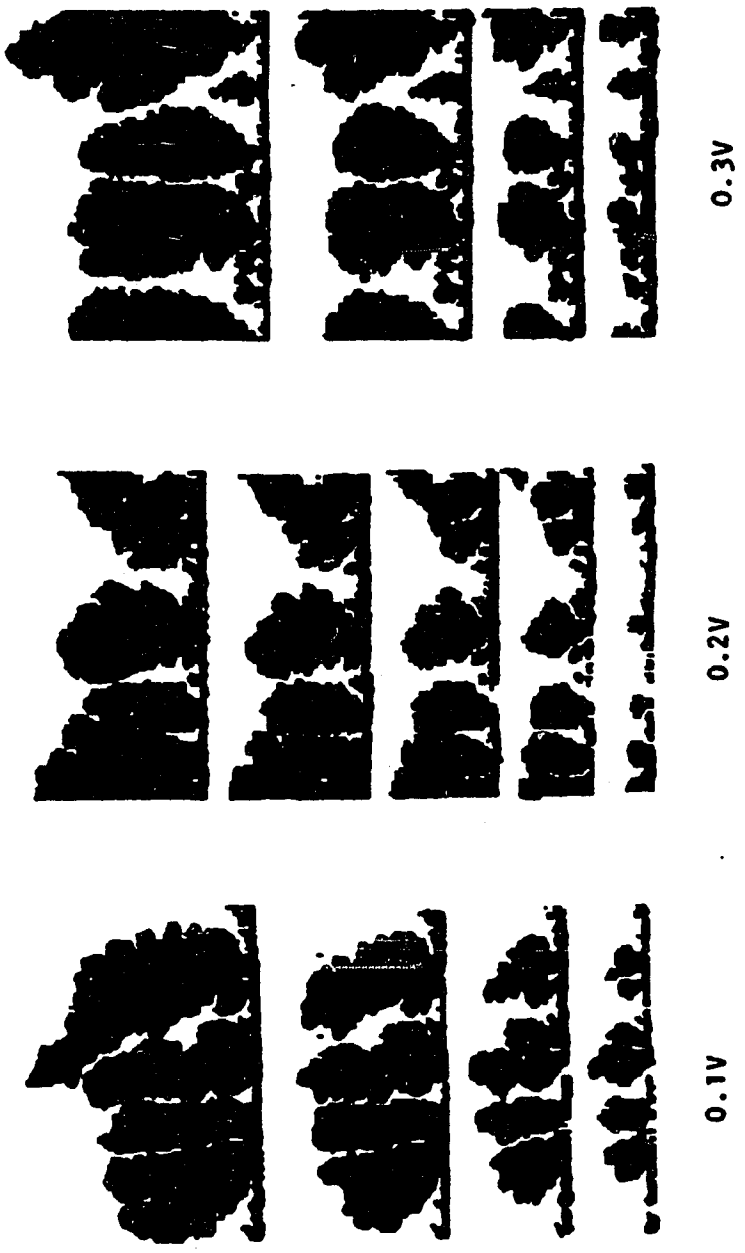

Figure 4.27: Time evolution of the growth patterns of silver deposited from 0.01M $AgNO_3$ at three potentials.(vs Ag/AgCl)

0.01M $AgNO_3$ xM NH_4NO_3	I_m% Eqn(4.4)	I_m% Eqn(4.10)
0.0	47.7	50.0
0.00125	41.7	33.3
0.01	22.7	14.6
0.1	4.0	2.3
1.0	0.4	0.19

Table 4.1

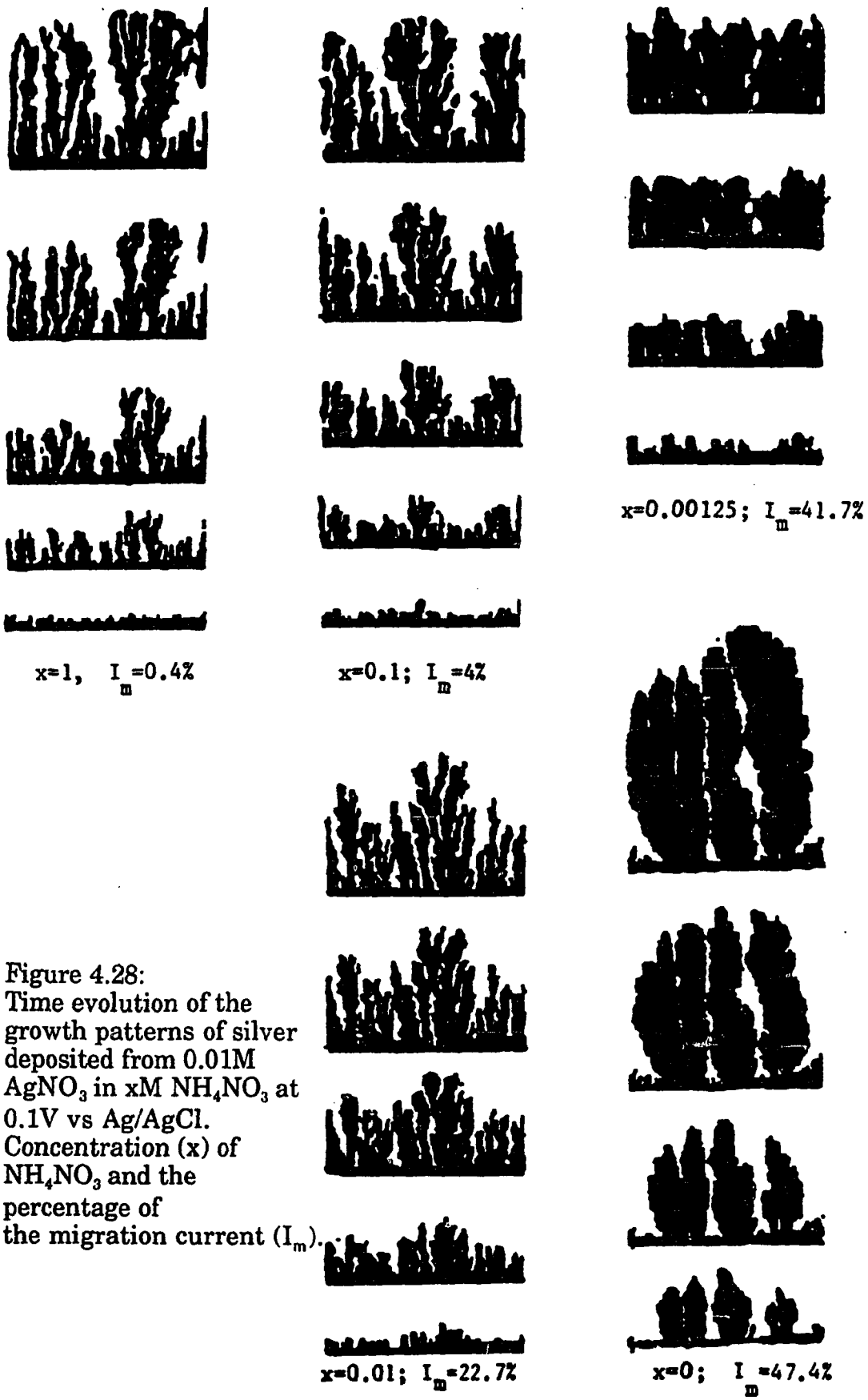

Figure 4.28:
Time evolution of the growth patterns of silver deposited from 0.01M $AgNO_3$ in xM NH_4NO_3 at 0.1V vs Ag/AgCl. Concentration (x) of NH_4NO_3 and the percentage of the migration current (I_m).

4.3. Impedance of Silver deposits.

4.3.1. Sample preparation and outline of procedure:

The pseudo 2D electrochemical cell used for the measurement is the same as the one used for the morphological study. The working electrode is a microstop painted, one edge open, silver foil of 25μm thick with 0.003cm^2 area exposed to the solution. The counter electrode is a gold coil of area of 12.8cm^2 immersed in the solution in the counter electrode compartment. A microstop painted platinum foil, of the same thickness as the silver foil, served as a spacer.

A double junction silver/silver chloride electrode with internal saturated KCl solution and external 1M KNO_3 solution is used as a reference electrode.

An EG&G model 173 potentiostat is used to deposit silver and oxidize it. The impedance measurements are done by using computer controlled Solartron model 1250 in the low frequency range and HP 3525A frequency analyzer with 3575A gain phase meter and DC bias supply at higher frequency range as described section 3.2.4 and shown in figure 3.5.

All the solutions are prepared with deionized water and analytical grade chemicals.

Microstop painted silver foils are polished at one edge with emery polishing paper, then at predetermined potentials, silver deposition is carried out in the 1M $AgNO_3$ for the dendritic structures with higher fractal dimensions. For the structures with low fractal dimension, solutions containing the supporting electrolyte such as 0.5M $AgNO_3$

with 2M NH_4NO_3, are used. The deposition is followed by a slow purge of the electrolyte with water that lasted for at least two to three days, until all the $AgNO_3$ solution is washed away. This step is followed by a slow sip of the KOH solution that also lasted for one to two days. Despite all these precautionary measures, some damage to the ramified structures is often observed. Impedance measurements of the silver deposits without oxide coverage are preformed by keeping the system at the rest potential.

For the oxidized structures, the cell is kept at a predetermined current to deposit the oxides on silver deposits under galvanostatic condition for the desired amount of charge. The impedance is measured at the rest potential of AgO that is determined by the CV characteristic curve of the silver foil in 1M KOH solution.

For the smooth silver foil, the oxides are deposited in the same manner and the impedance measurements followed the same procedure.

The measurement of counter length followed the procedure described in section 2.2. The measurements are performed at the conclusion of the chemical treatments to account for the often observed damage to the structure.

4.3.2. Results:

Figure 4.29 shows the impedance spectra of smooth silver with 151.1C/cm^2 of both oxides. The solid lines are theoretical fits to the equivalent circuit shown figure 4.30(a). It closely resembles the published result on the impedance spectra of the two oxides in a three dimensional cell under similar conditions[25] with the two peaks in the

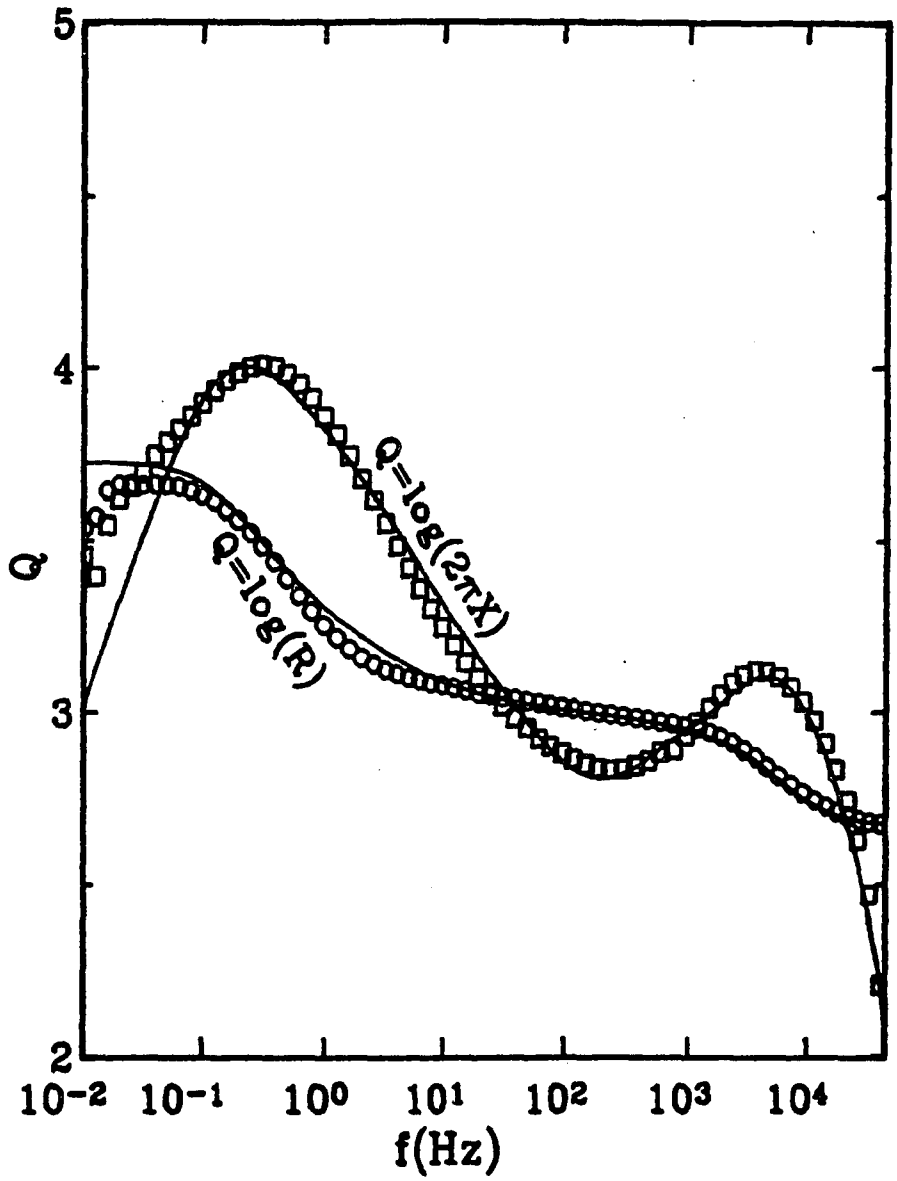

Figure 4.29: Spectra of the real (R) and imaginary (X) parts of the impedance of oxidized smooth silver foil in 1M KOH solution at potential of 0.4V vs Ag/AgCl. Points - Expt., Solid line - fit to the equivalent circuit in figure 4.30(a).

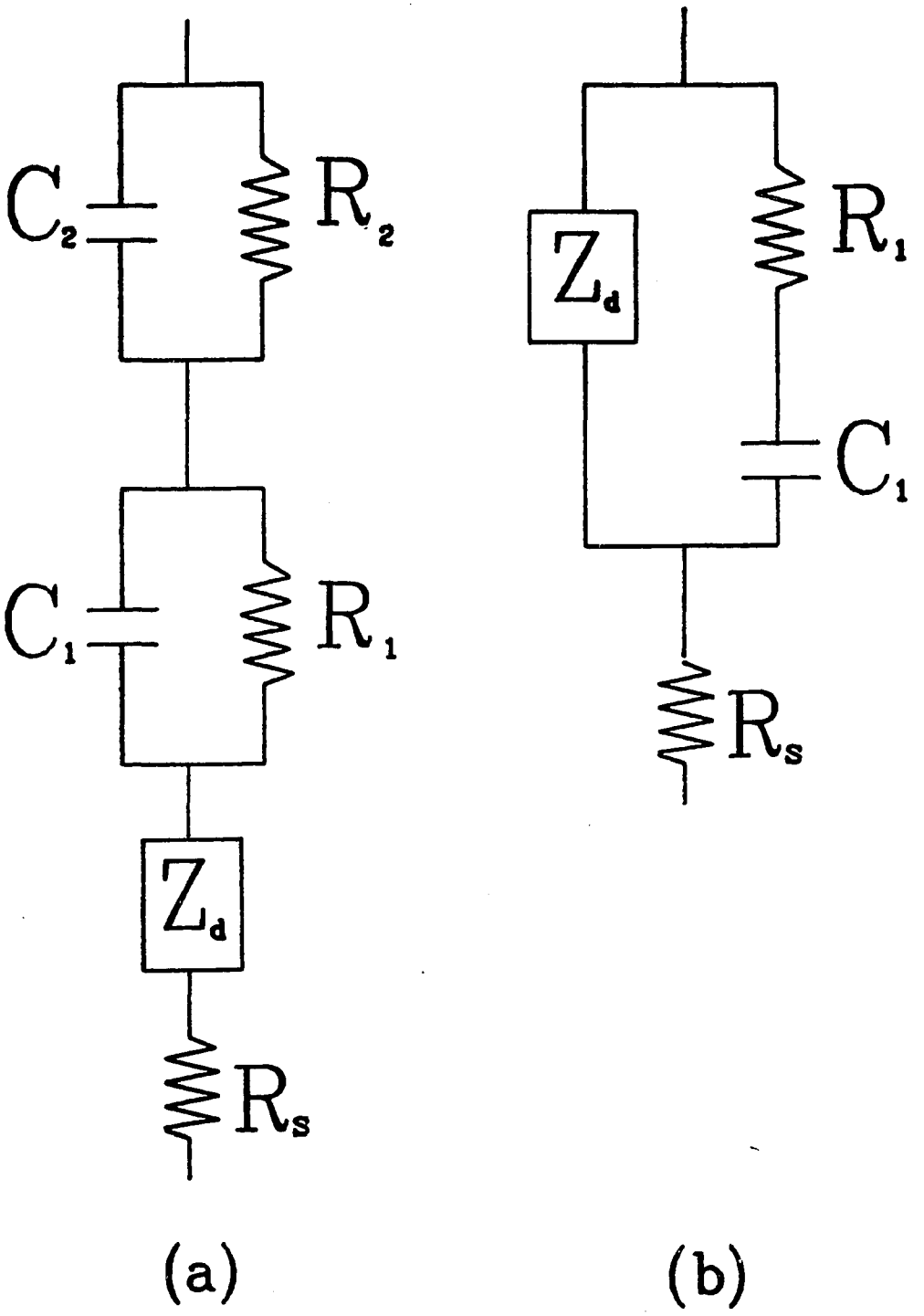

Figure 4.30: Equivalent circuit for the oxidized (a) and unoxidized (b) electrodes.

imaginary part corresponding to the two oxides. The impedance spectra of of the three different ramified structures are shown in figures 4.31, 4.32 and 4.33. The CPA region is evident in figure 4.31 and much less obvious in figure 4.32. The solid lines in both figures are fitted to the equivalent circuit in figure 4.30(a). Figure 4.33 shows an example of a ramified silver structure without any oxides present. The solid lines of the spectra without the oxides are fitted to the equivalent circuit shown in figure 4.30(b). A summary of the fitted parameters and the total charge, for all the oxidized samples, is presented in table 4.2. To gain more information on the origin of the elements in figure 4.30 we have investigated the changes in the corresponding capacitive elements with oxidation charge and in two different electrolyte concentrations, on a smooth silver foil. The results are presented in figure 4.34 and 4.35.

4.3.3. Discussion:

The basic premise that has motivated this work is that, if there is a correlation between the exponent in the CPA element and the fractal dimension of the underlying structure, then it can be best explored in a system in which the interface is almost purely capacitive, and thus, the admittance will scale with the real area through the surface fractal dimension.

The data in table 4.2, and that can also be seen in figure 4.35, clearly shows that the basic premise was incorrect. Although the exponent varies with the fractal dimension, it does so independently of the oxidation state of the surface. These results also put into question the origin of the various charge accumulation modes and whether a single element describes a well defined dielectric contribution under all the experimental conditions that we have investigated here. Since all the

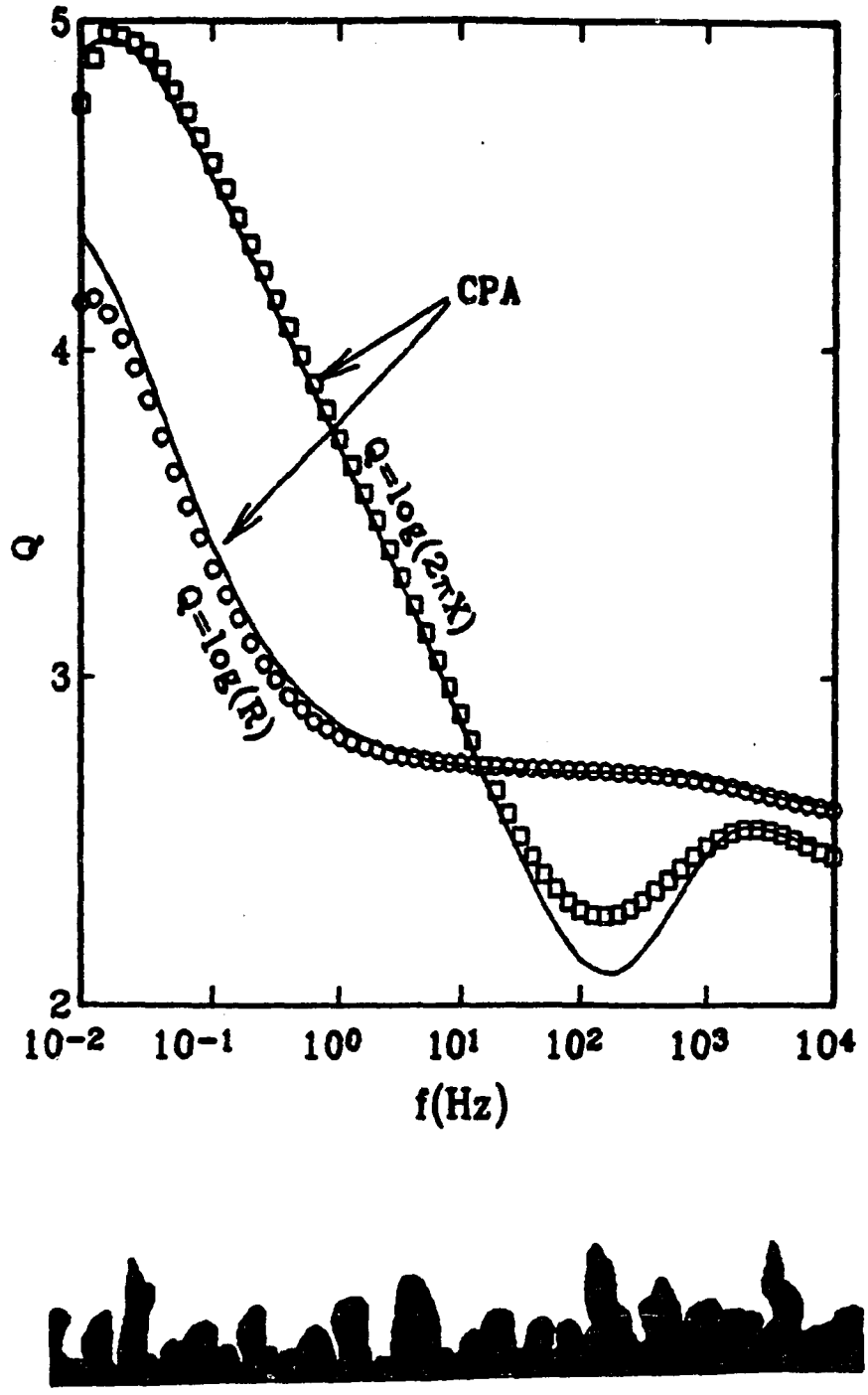

Figure 4.31: The same as Fig. 4.29 but for the pattern shown (sample #2 in table 4.2). The pattern was deposited from 0.5M $AgNO_3$ + 2M NH_4NO_3, oxidized in 1M KOH and measured at 0.4V vs Ag/AgCl. Oxidation charge - 1.30 C; Real area - 0.016 cm^2. Points - experimental, Solid lines - fit to the equivalent circuit in Fig. 4.30(a)

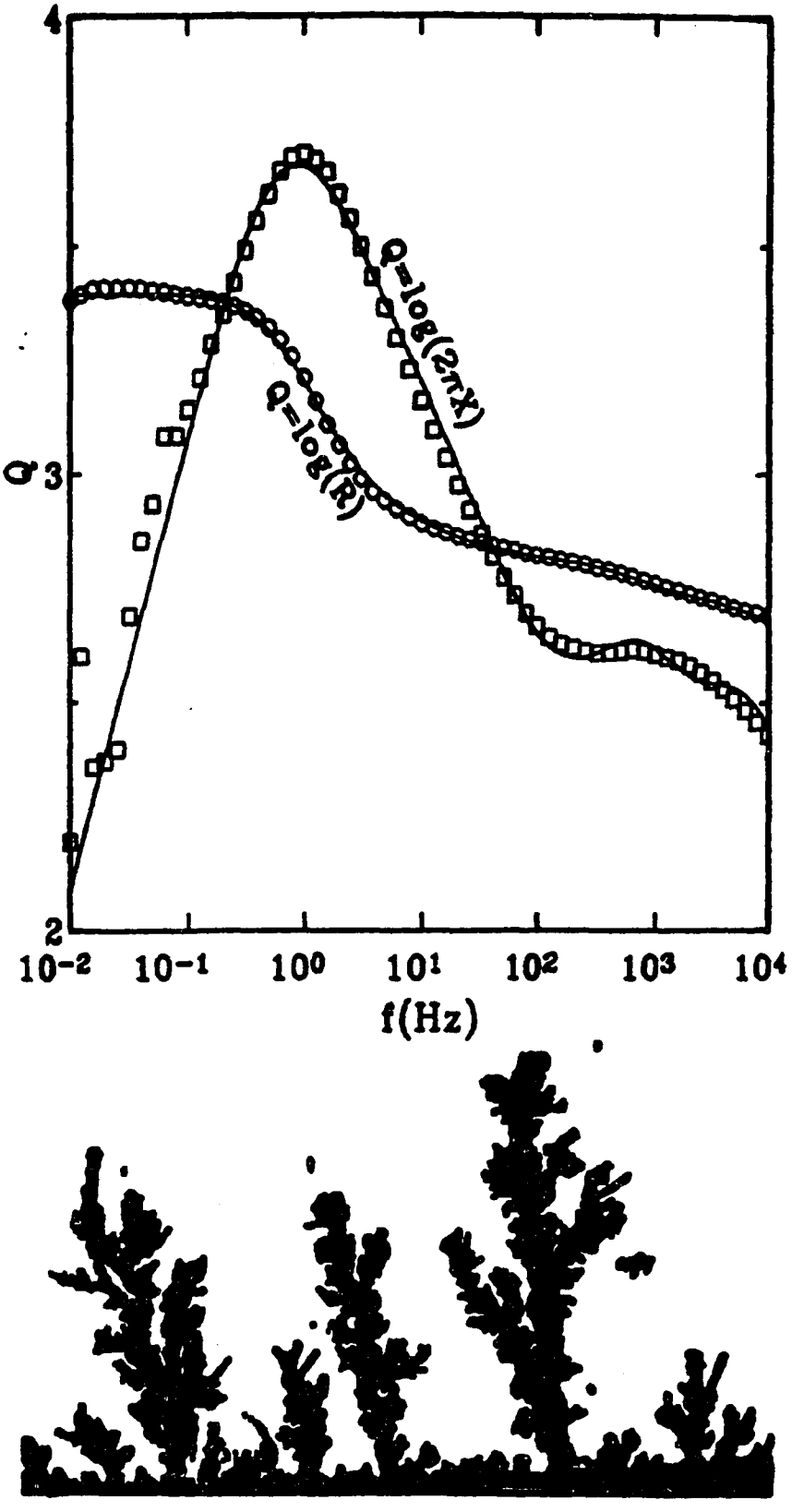

Figure 4.32: The same as Fig. 4.31 (sample # 5 in table 4.2) but the pattern deposited from 1M $AgNO_3$. Oxidation charge-2.0 C; Real area - 0.083 cm^2.

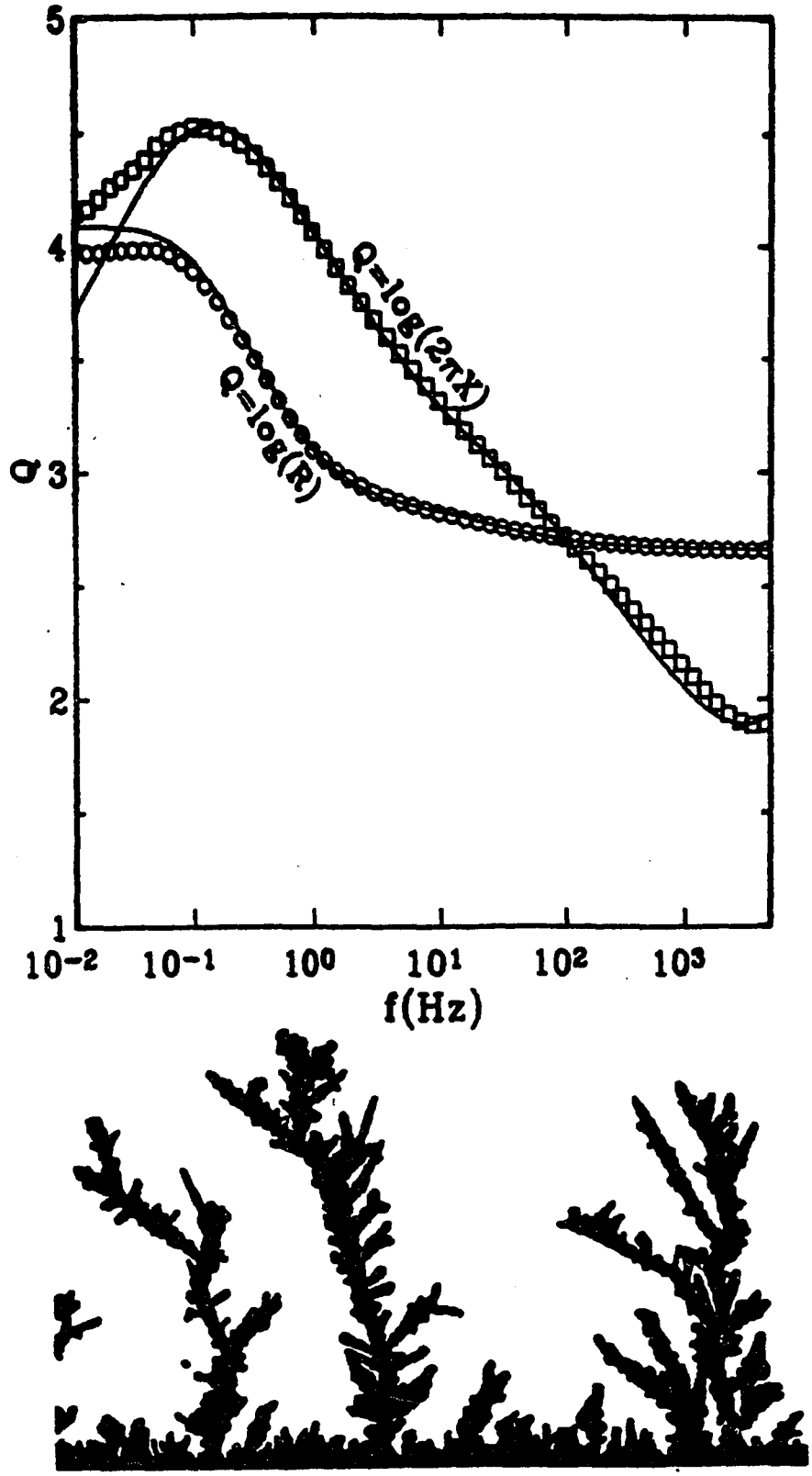

Figure 4.33: The same as Fig. 4.32 (sample #6 in table 4.2). Sample was not oxidized. Spectra taken at a potential of -0.1V vs Ag/AgCl.Solid lines - fit to the equivalent circuit in Fig. 4.30(b).

#	Nature Q C/cm^2	R_1 (Ω)	C_1 (μF)	R_2 (Ω)	C_2 (μF)	N (Ω)	n	τ (sec)	R_s (Ω)	d_f
1	α 151.2	355	0.08	104	1.78	4404	0.53	1.15	469	2.0?
2	151.0	90	0.16	71	0.99	3045	0.84	11.5	445	1.19
3	162.0	150	0.15	75	0.95	4100	0.86	20.95	533	1.10
4	152.0	360	0.42	142	0.11	1285	0.66	0.99	474	1.47
5	93.6	88.6	0.31	79	0.26	1850	0.65	0.25	454	1.51
6	β 0.0	900	24.5	0	0	11900	0.71	1.10	457	1.40
7	τ 0.0	2000	12.5	0	0	10900	0.60	0.67	525	1.51
8	δ 0.0	495	9.4	0	0	125000	0.90	30.0	550	1.0

Table 4.2

α : Smooth Ag foil with oxides in 1M KOH, for circuit in Figure 2(a).
β : Dendritic Ag on Ag foil in 1M KOH, for circuit in Figure 2(b).
τ : Dendritic Ag on Pt foil in 1M KOH, for circuit in Figure 2(b).
δ : Smooth Ag foil in 1M KOH for circuit in Figure 2(b).
All others for Ag deposits on Ag foil in 1M KOH, for circuit in Figure 2(a).

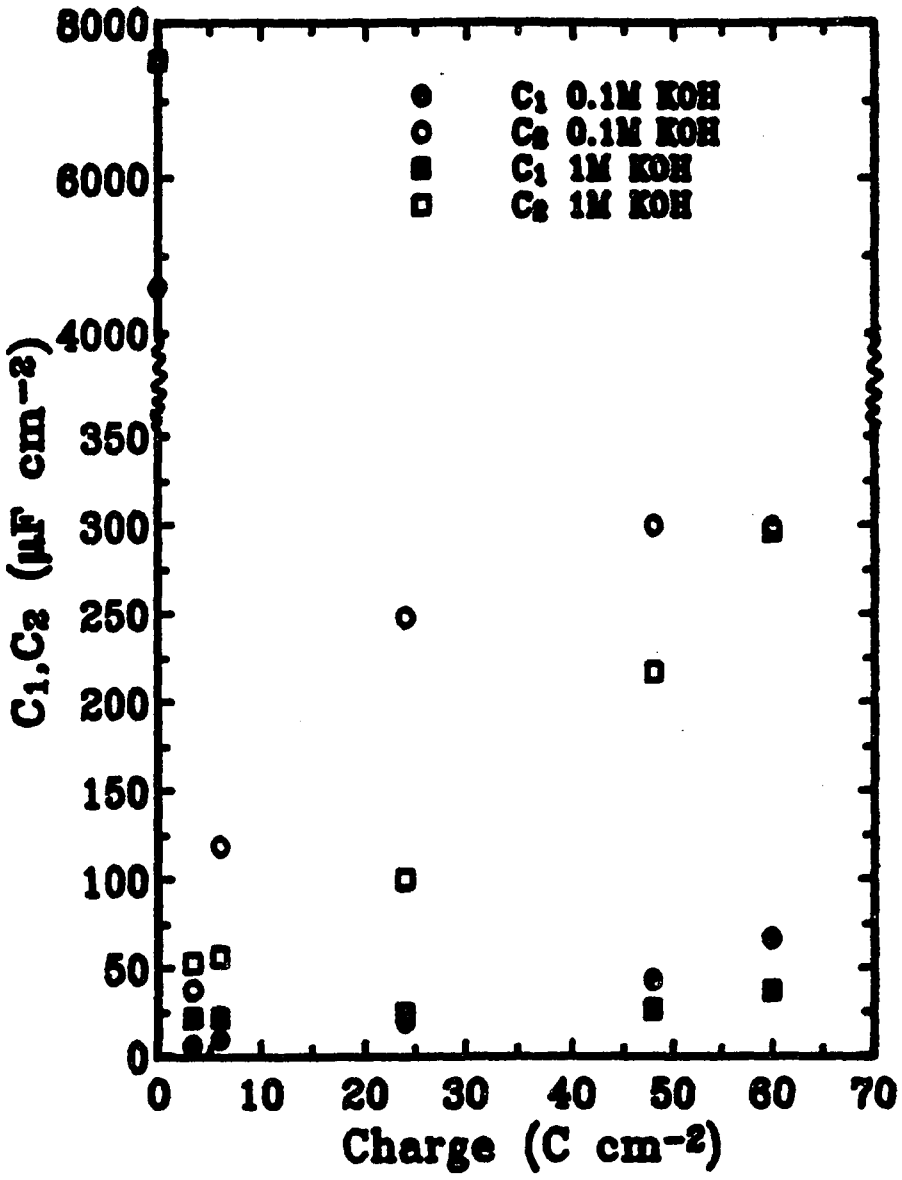

Figure 4.34: C_1 and C_2 as a function of the oxidation charge on a smooth silver foil, in two different electrolyte concentrations. All conditions the same as in Fig. 4.29.

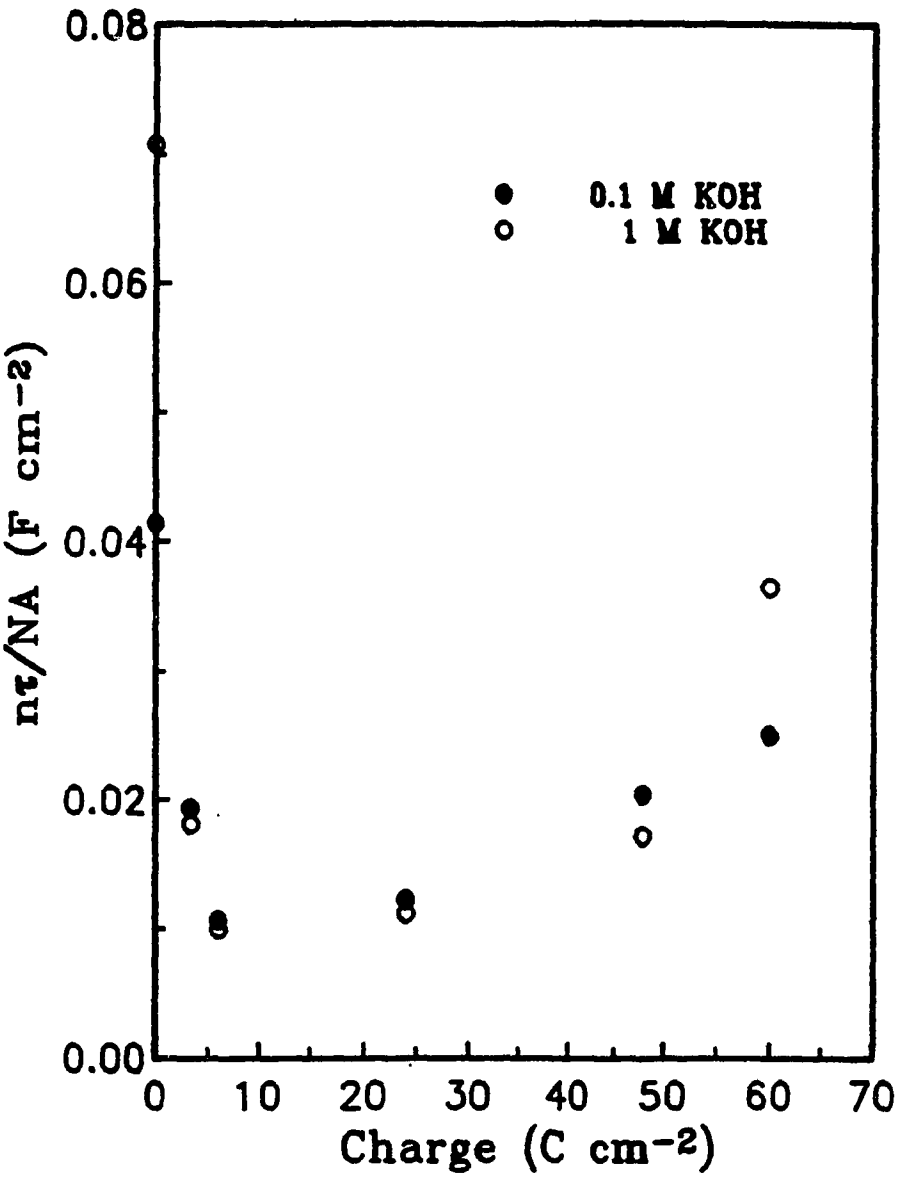

Figure 4.35: The low frequency CPA capacitance, nτ/NA, as a function of oxidation charge. Same conditions as in Fig. 4.34.

results are analyzed using the same two equivalent circuits independent of the ramification of the structures; in the first part we will discuss the dielectric response of the oxidized and unoxidized smooth silver foil in two dimensional cell and try to elucidate the nature of the elements in the equivalent circuits. We will then discuss the ramified structures and try to correlate their morphology with their impedance.

4.3.3(a) The charge accumulation modes on smooth silver:

Figure 4.34 shows the variation of the two capacitive elements in figure 4.30(a) with the oxidation charge and with the concentration of the electrolyte. Let us first discuss the possible origin of the charge accumulation modes of the unoxidized silver (Figure 4.30(b)). The capacitance increases with the electrolyte concentration, and its high value excludes a measurable contribution from the double layer. The only reasonable source that we can suggest for the origin of this element is pseudocapacitance due to adsorption. The variation of $n\tau/N$ of the unoxidized silver (Figure 4.35) with the concentration of the electrolyte follows the same pattern as that of the capacitive element but with higher values. There is no reason to invoke a new process to account for the CPA here. One has to assume that it originates from the contribution of diffusion to the adsorption process.

Except for the CPA, the equivalent of the oxidized silver is the as the one that was postulated earlier[25] in the three dimensional cell. The difference between this work and the previous work originates from the fact that almost all the analysis in [25] was confined to the Ag_2O layer that behaved as a pure dielectric. The peak in the imaginary part that

was associated with AgO did not behave as a pure dielectricum in [24-25] but this aspect was not pursued there. The C_1 here, as in [24-25], is much smaller than C_2, independent of the concentration of the electrolyte and slowly increases with the oxidation charge. All this suggests that it originates from a compact Ag_2O layer. The C_2, on the other hand, depends on the concentration of the electrolyte, not only its value but also its functional dependence on the oxidation charge. For the low electrolyte concentration, it increases rapidly with the oxidation charge and then it saturates. For the high electrolyte concentration, the capacitance values are lower and they increase with the oxidation charge until they reach the values of the low electrolyte concentration. This behavior suggests that C_1, and its associate resistor R_1, behave as an effective medium dielectricum (away from percolation since it is frequency independent) made of hydrated AgO. The $n\tau/N$ shows a smooth transition between the unoxidized and oxidized states. The only major difference is that after a small amount of oxidation charge, it becomes independent of the concentration of the electrolyte. The variation with the oxidation charge is different from the other two elements, passing through some sort of minimum. We also have to account here for the appearance of this element in series with the other two dielectricums. We have tried, without success, to fit the data to an equivalent circuit in which the CPA is in parallel with one of the two capacitive elements. We realize that an increased complexity of the suggested equivalent circuit can result in a possible good fit also for the parallel configuration. Nevertheless, the present model is the simplest one that we could come out with, and all our interpretations are based on this model. Within this model, the simplest interpretation of the CPA

in series for the oxidized electrode is that the hydrous AgO layer, near the interface with the Ag_2O, has a composition which approaches the percolation threshold[48]. This kind of double layer structure of hydrous oxide in series with a thin compact layer is being now invoked for many passivating layers.

4.3.3(b) The ramified structures:

The equivalent circuits in figure 4.30 are found to fit both the smooth and the ramified structures. We will assume that the origin of the charge accumulation modes that was postulated in the previous section holds also for the ramified structures. We are fully aware of the possibility that the oxide coverage of the ramified structure is inhomogeneous, particularly with respect to the portions of the silver substrate that are not branching out. We have used the rest potential of AgO as a probe for a complete coverage. The high concentration of KOH should prevent the appearance of mixed potentials due to porosity. The possibility that mixed potentials due to incomplete coverage and due to porosity will cancel out, is remote.

The resulting impedance parameters and the surface fractal dimensions are summarized in table 4.2 and the correlation between the fractal dimensions and the CPA exponents are plotted in figure 4.36. It is obvious that the dependence is monotonic and the fit to the reciprocal relations is not bad. However, the "fit" looks much better for the reciprocal relationship than for the linear relationship particularly due to the way in which the point for the oxidized smooth surface was plotted. The CPA exponent for the oxidized smooth surface is found to be equal to 0.53. The n=0.5 is the expected value for the impedance of an ideally polarizable bulk porous structure based on classical impedance

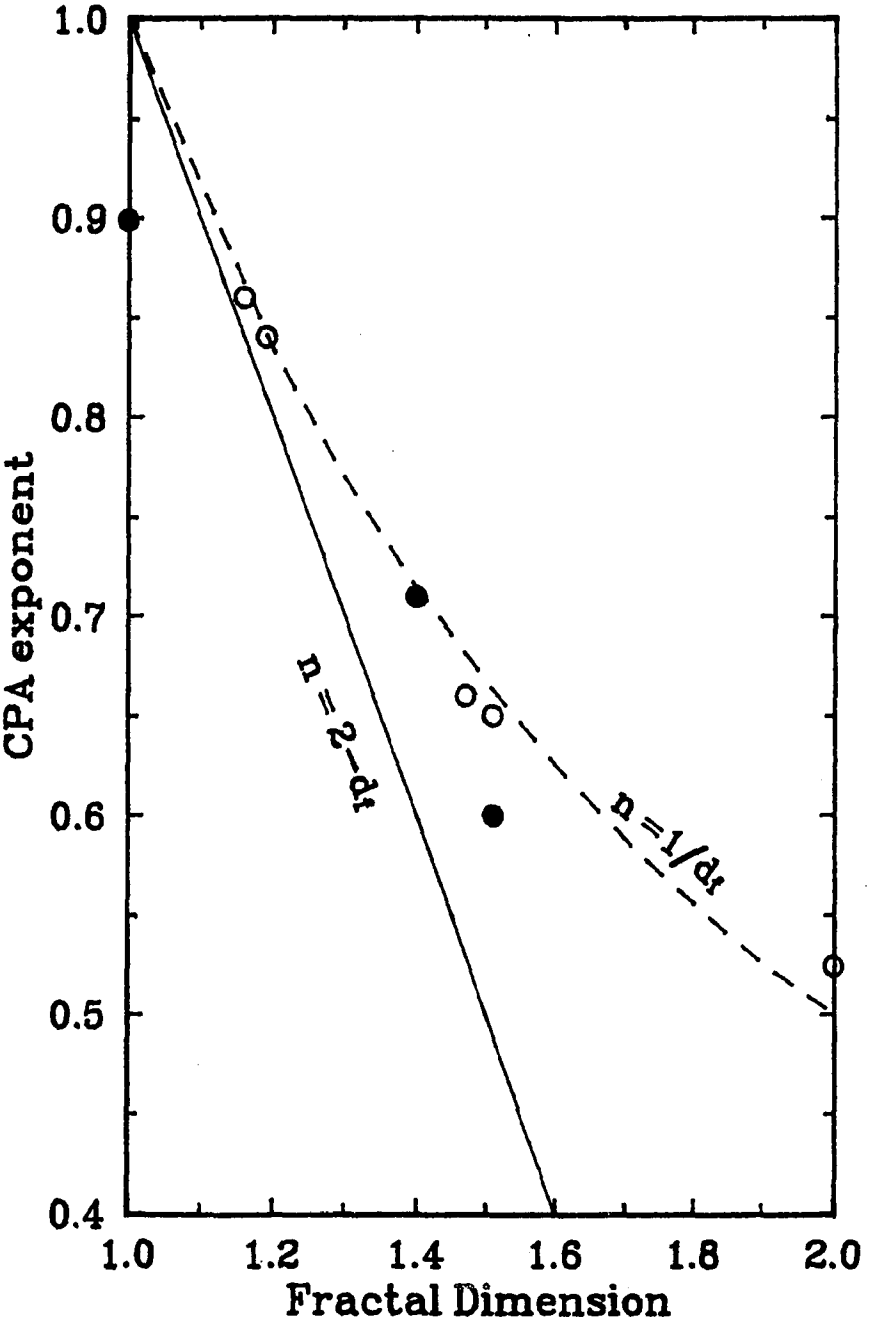

Figure 4.36: Correlation of the CPA exponent with the fractal dimensions. The two lines demonstrate the expected correlations based on the reciprocal and linear models. The filled points are due to unoxidized electrodes.

calculation (section 2.3.2) and measurement of porous structures almost regardless of the specific morphology[46]. Based on this, we have associated the oxidized, smooth, substrate with a bulk porous layer with "surface" fractal dimension of 2. This is an arbitrary lip for which we have no justification.

If, for the reason stated, one neglects this point, the dynamic range of the two models and that of the measurements are small compared to the accuracy, making it very difficult to distinguish between the two models.

Perhaps the clearest result that emerges from these data and the one with greatest importance, is not the distinction between the two models but the fact that there is no difference in the correlation between the oxidized and nonoxidized interface. The observation that the dielectric properties of the interface are irrelevant to the correlation between the scaling properties of the interface and the impedance exponent, nullifies the most fundamental assumption in most of the published work which is based on a capacitive interface that scales linearly with the area. The present results are in agreement with Sapoval's prediction[50], that the correlation is independent of the interfacial impedance and originates from convergence of the high frequency cutoff to the fractal dimension of the system. An alternative to this interpretation is that, at least for the present system, the monotonic correlation originates from a different source than a straightforward geometrical scaling. Since it is argued that the CPA of the unoxidized silver originates from diffusion of the electrolyte to the interface, we need to examine the possibility that the correlation between d_f and n originates from restricted diffusion on fractal substrate[75]. Under these

conditions we expect $n = \mu/d_w$ where μ is the conductivity exponent and d_w is the diffusion exponent. For loopless DLA patterns it was shown that $\mu \sim 1$ and $d_w = d_f$ [76], will bring us back to the reciprocal relationship without the requirement of a purely capacitive interface. However, some of the structures, particularly those with low fractal dimension, are not DLA and the relationship is probably not a universal one.

It might be instructive to look for a correlation of the CPA exponent with the higher order fractal dimensions D_q[77] and examine the singularity spectrum $f(\alpha)$[78] of the higher order moments q that are associated with the growth probability distribution. The analysis has followed the method of Chabra et. al.[79]. Figure 4.37 shows the $f(\alpha)$ spectra for three samples, and in figure 4.38 we present the D(q) for these structures. Figure 4.39 is similar to figure 4.36 except that now we present the possible correlations with n of some higher order of D(q) for these structures. It is evident that the statistic here is even worse than in figure 4.36; however, the general trend remains identical to that of $D(0)$ ($=d_f$ or D_0).

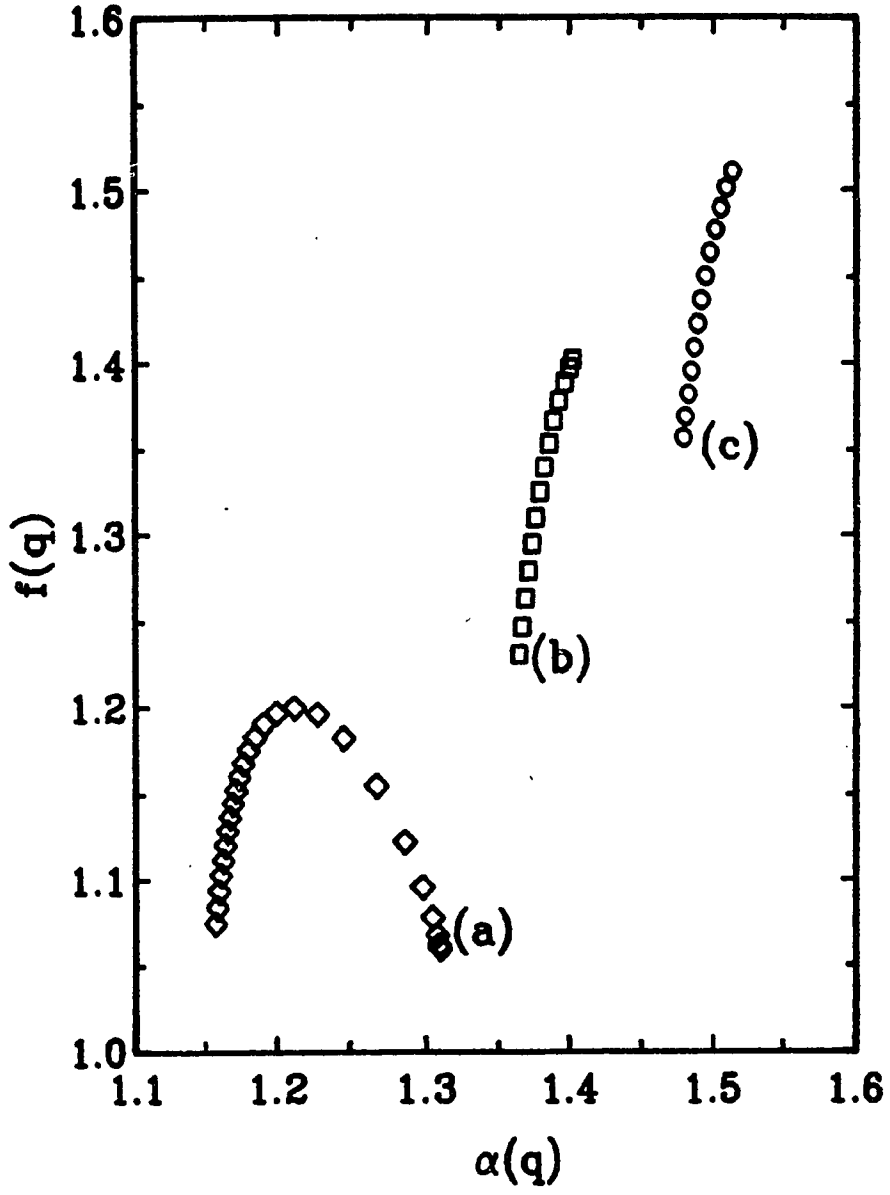

Figure 4.37: f(α), singularity spectra of the structures for samples (a). #2, (b). #5, and (c). #4

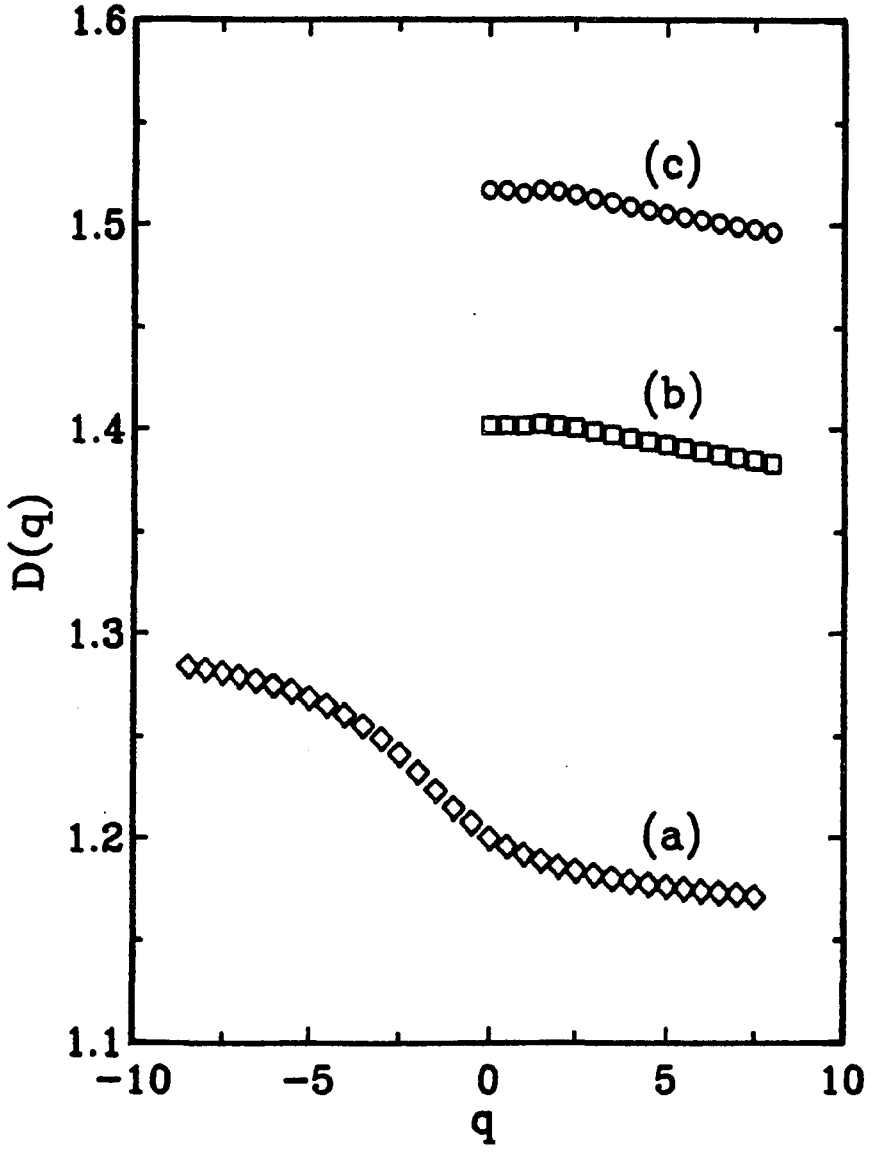

Figure 4.38: Spectra of the generalized dimensions D_q from Fig. 4.37.

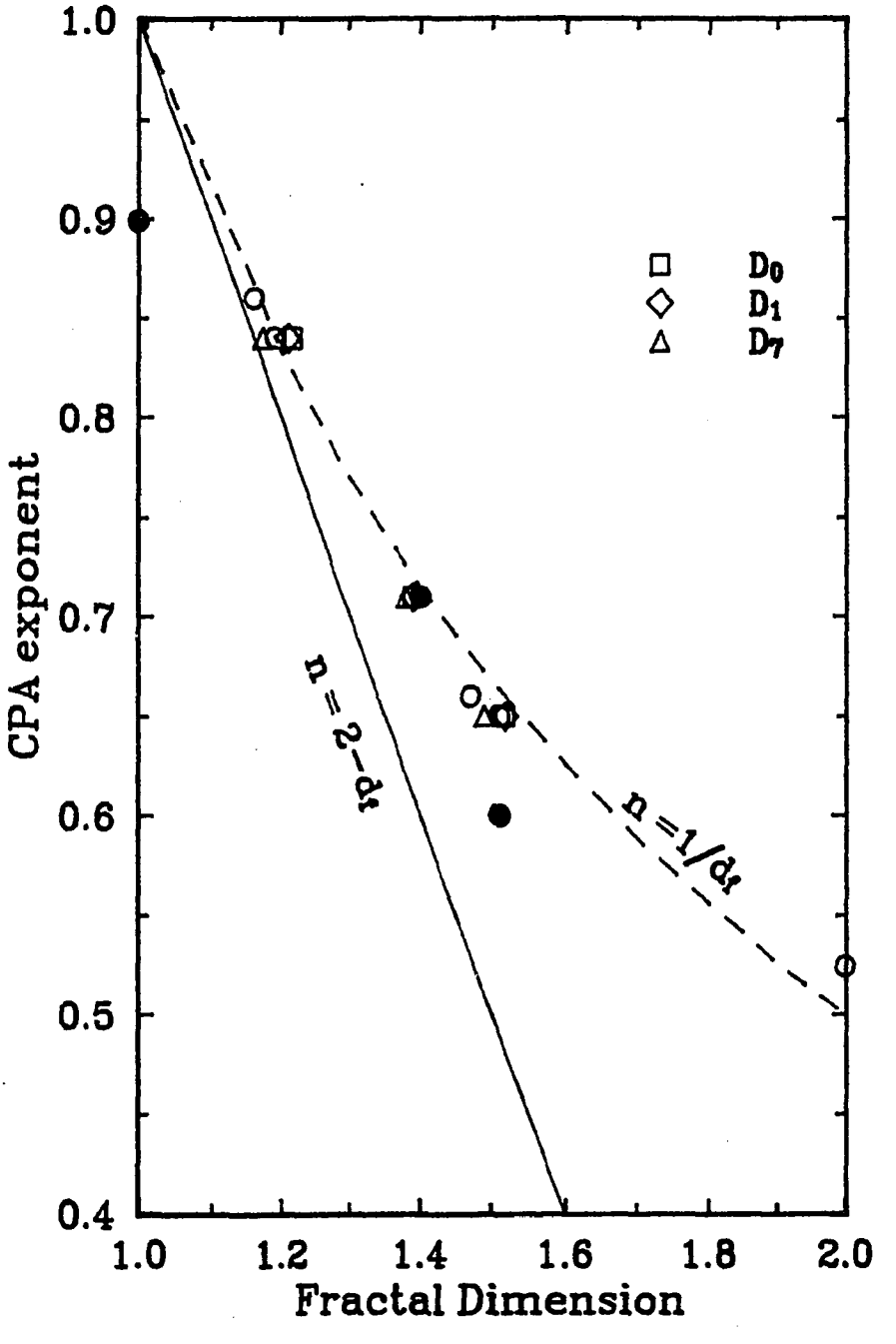

Figure 4.39: The same as Fig. 4.36 but for two of the higher fractal dimensions.

5. Conclusions and Suggestions for future work

5.1 Morphology:

In order to gain deep insight into the pattern formation in an electrochemical system and to narrow the gap between the recent advances in mophogenesis and the electrochemistry of the growth, we have employed the fractal characterization as a geometrical parameter and the chemical kinetic parameters to observed possible correlations.

Two computer simulation models: diffusion limited aggregation and multiparticle diffusion limited deposition were used to compare the experimentally observed growth patterns.

Electrochemical techniques, such as linear sweep voltammetry (LSV) and chronoamperometry, were employed to understand the growth in the different potential regions of the reaction and to evaluate the chemical parameters. The parameters obtained from the chronoamperometry should be taken only as an empirical fit. The theory is based on the evolution of the surface of hemispherical nuclei which is obviously different from the present morphology.

The LSV is employed to obtained the different potential regions of the reaction which are then used to deposit the metals under the potentiostatic condition. In general, transition from activation controlled kinetics to mass transfer limited kinetics takes place at the same potential range as the DLA formation for all the systems that are driven by the diffusion or in the system in which the diffusion is the dominating mechanism over the migration. Here we assume that in the present cell configuration convection is at a minimum or zero. The system which has the equal migration component as the diffusion,

tend to produce columnar type structures with a coherent growth front. The drift diffusion simulation can only reproduce the coherent nature of the growth but not the columnar structures.

The fractal dimension is proven to be useful in characterizing these morphologies. However, two structures with different appearances (different spatial distributions) can have the same fractal dimension; therefore, in that sense, one needs another parameter to described those morphologies in a unique way. We have tried without success to obtain the Fourier spectrum of two dimensional structures, hence to find the characteristic frequency.

To put these observations in prospective order, the existing chemical kinetic relations and the chronoamperometric formula must be reformalized, using the moving boundary conditions as well as the evolution of the surface area.

We fully realize that this work is rich in empirical data but lacks a comprehensive framework in which most of the data can securely fit. If one takes the general patterns of the results and does not pay too much attention to "details", the evolution of the morphologies, when the growth is govern by the diffusion, is in good agreement with the computer simulations which took into account only competition between the "sticking" and diffusion (MPDLD).

Although, the zinc system in the supporting electrolytes solutions produced some problems in observing the growth in the entire potential range, the silver system allows us to demonstrate the effect of the supporting electrolyte on the growth morphology hence to study the effect of the diffusion-migration ratio.

5.2 Impedance:

Direct evidence from this study shows it is difficult to distinguish experimentally, the correlation of n and d_f, between the two models, namely Liu and Le Mehaute.

The clearest result that emerges from these observations and one with the greatest importance, is not the distinction between the two models but the fact that there is no difference in the correlation between the oxidized and non-oxidized interfaces. The observation that the dielectric properties of the interface are irrelevant to the correlation between the scaling properties of the interface and the impedance exponent nullifies the most fundamental assumption in most of the published work which was based on capacitive interface that sales linearly with the area and thus provides the link between the dynamic and static scaling properties.

The present results are in good agreement with Sapoval's prediction that the correlation is independent of the interfacial impedance and originates from convergence of high frequency cutoff to the fractal dimension of the system. An alternative to this interpretation is that at least for the present system, the monotonic correlation originates from a different source than a straight forward geometrical scaling.

5.3 Suggestions for Future work:

In the present work we have investigated the growth under the potentiostatic (constant potential) condition in which we incorporate the potential with the sticking coefficient of the simulations. It may be interesting to see what impact on the growth patterns would occur, if we use the galvanostatic (constant current) conditions to deposit the

structures. In this situation, potential varies with time till it reaches the deposition value while the number of particles attached to the deposit per unit time is constant.

It might be instructive to study the single or the multiparticle simulation not starting on a smooth substrate, but on a real structure, say, which is taken at time t_1 from a real deposit and then by varying the fraction, f, and the sticking coefficient, s, try to reproduced the real structure at a time t_2 ($>t_1$). This type of simulation may be used to find a direct correlation between f and s with the concentration and the applied potential. A preliminary result of such a simulation using MPDLD model is shown figure 5.1, which is started on the structure shown in Fig.4.26, grown at -0.1V vs Ag/AgCl and at time (t_1) 30 sec. Here we used f=0.15, s=1 and the simulation carried on the 256x256 grid (the real deposit which is on 512x512 grid is shrink to a 256x256), up to 2000 particles attached to the deposit. The simulated structure (dark) on the original real deposit at 30 sec. (light-dots) is compared with the real structure at 60 sec. (only the boundary of the real structure is shown).

Although, we were unable to reproduce the columnar structures using the drift-diffusion model, one can further investigate these by using other models such as random rain model[80] with diffusion or dielectric breakdown model[4] with different probability exponent (η) than the DLA (η=1 for the DLA process).

Experimentally, the solution with low concentrations, that led to a columnar type growth can be further investigated by varying the cell dimensions, such as length of the cathode, separation between the electrodes and the thickness of the cathode, for a possible correlation between these and the column separation.

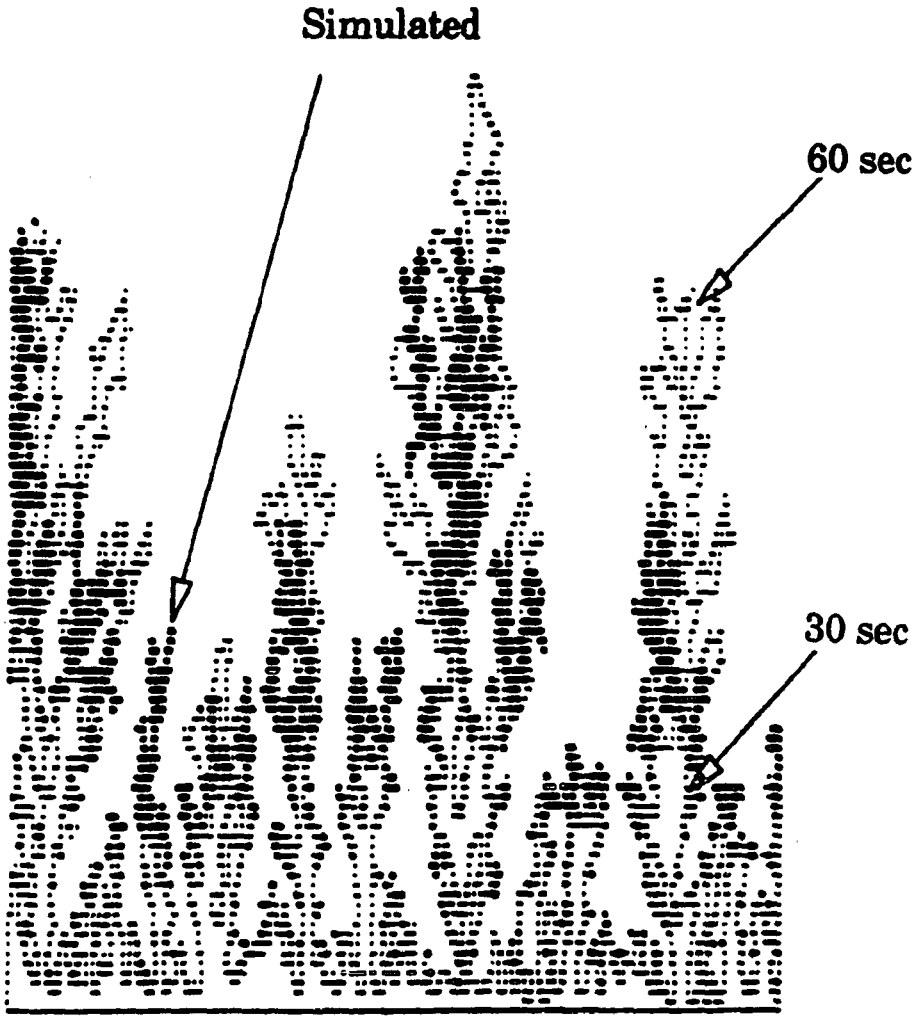

Figure 5.1: Simulation of the deposition using MPDLD model starting on a real structure (A suggestion for future work)

Appendix (A).

The current-overpotential equation:

Consider the reaction;

$$O + ne \underset{k_b}{\overset{k_f}{\rightleftarrows}} R \qquad (A.1)$$

where O is the Oxidized species, R is the reduced species, k_f, k_b are the forward and backward reaction rates, and n is the number of electrons represents in the reaction.

The reaction rate (V) can write as;

$$V = k\,C \qquad (A.2)$$

Therefore,

$$V_f = k_f C_O(0,t) \qquad (A.3)$$

$$V_b = k_b C_R(0,t) \qquad (A.4)$$

where $C_O(0,t)$ and $C_R(0,t)$ are the concentration of oxidized and reduced species at the electrode (x=0) at time t.

We also can write the number of moles electrolyze;

$$N = Q/nF \qquad (A.5)$$

where Q is the total charge and F is the Faraday constant.

Then reaction rate,

$$\frac{dN}{dt} = \frac{1}{nF}\frac{dQ}{dt} = \frac{i}{nF} \qquad (A.6)$$

and the reaction rate per unit area;

$$v = \frac{1}{A}\frac{dN}{dt} = \frac{i}{nAF} \qquad (A.7)$$

Using (A.3) and (A.4) with (A.7);

$$v_f = \frac{i_c}{nAF} = k_f C_O(0,t) \qquad (A.8)$$

$$v_b = \frac{i_a}{nAF} = k_b C_R(0,t) \qquad (A.9)$$

where i_c and i_a are the cathodic (reduction) and anodic (oxidation) current of the reaction.

The total current of the reaction,

$$i = i_c - i_a = nFA[k_f C_O(0,t) - k_b C_R(0,t)] \qquad (A.10)$$

We can write the general form of k_f and k_b by considering either Activation complex theory [ref.35 pg 89] or based on free energy curve [ref 35 pg 92] as;

$$k_f = k^0 e^{-\alpha_c n f(E - E_0')} \qquad (A.11)$$

$$k_b = k^0 e^{-\alpha_a n f(E - E_0')} \qquad (A.12)$$

where k^0 is the standard rate constant, α_c, α_a are the cathodic and anodic transfer coefficient, E_0' is the standed electrode potential, E is the applied potential and f=F/RT.

The equation (A.10) with (A.11) and (A.12) gets the form,

$$i = nAFk^0[C_O(0,t)\, e^{-\alpha_c n f(E-E_0')} - C_R(0,t)\, e^{-\alpha_a n f(E-E_0')}] \qquad (A.13)$$

The exchange current i_0 is defined as

$$i_0 = i_c^{eql.} = i_a^{eql.} \text{ at } E = E_0 \text{ and } C_O(0,t) = C_O^*,\ C_R(0,t) = C_R^*,$$

Therefore from (A.8) and (A.11):

$$i_0 = k^0 C_o^* e^{-\alpha_c n f(E_0 - E_0')} = i_c^{eql} \qquad (A.14)$$

and from (A.9) and (A.12) give us;

$$i_0 = k^0 C_R^* e^{-\alpha_a n f(E_0 - E_0')} = i_a^{eq} \quad (A.15)$$

Dividing (A.13) by i_0 we can write,

$$\frac{i}{i_0} = \left[\frac{C_O(0,t)}{C_O^*} e^{-\alpha_c n f(E-E_0)} - \frac{C_R(0,t)}{C_R^*} e^{-\alpha_a n f(E-E_0)}\right] \quad (A.16)$$

Now if we consider the same reaction (A.1) and then at the steady state and diffusion control, the mass transfer rate v_{mt} is given by,

$$v_{mt} \alpha \left(\frac{\partial C}{\partial x}\right)_{x=0} \quad (A.17)$$

Therefore $$v_{mt} = m_j \left[C_j^* - C_j(0,t)\right] \quad (A.18)$$

where j= O or R.

and $$\frac{i}{nAF} = m_j \left[C_j^* - C_j(0,t)\right] \quad (A.19)$$

At the limiting stage of the reaction $C_j(0,t) = 0$ and,

then (A.19) => $i_{l,j} = nAFm_j C_j^*$ is the limiting current of the j^{th} species.

Therefore $$i_{l,c} = nAFm_O C_O^* \quad (A.20)$$

$$i_{l,a} = nAFm_R C_R^* \quad (A.21)$$

If the total current (i) is either due to the cathodic or the anodic reaction, equation (A.19) can write with (A.20) or (A.21) as,

$$\frac{C_O(0,t)}{C_O^*} = \left(\frac{i_{l,c} - i}{i_{l,c}}\right) \quad (A.22)$$

$$\frac{C_R(0,t)}{C_R^*} = \left(\frac{i_{l,a} - i}{i_{l,a}}\right) \quad (A.23)$$

Now If we plug (A.22) and (A.23) into (A.16) we arrived at, equation (2.11),

$$i = \left(\frac{i_{l,c} - i}{i_{l,c}}\right) e^{-\alpha_c n f \eta} - \left(\frac{i_{l,a} - i}{i_{l,a}}\right) e^{-\alpha_a n f \eta} \qquad (2.11)$$

with $\eta = E - E_0$.

Appendix (B)

Convolution or Semi-integral techniques:

Consider the Fick's second law of diffusion for O-species:

$$\frac{\partial C_O(x,t)}{\partial t} = D\frac{\partial^2 C_O(x,t)}{\partial x^2} \qquad (B.1)$$

and the boundary condition for a semi-infinite diffusion,

$$C_O(x,0) = C_O^* \text{ and } C_O(x,t)=C_O^* \text{ as } x \to \infty \qquad (B.2)$$

If we use the Laplace transformation

$$L\left\{\frac{dF(t)}{dt}\right\} = sf(s) - F(s)$$

then the equation (B.1) becomes,

$$s\overline{C}_O(x,s) - C_O^* = D\frac{\partial^2 \overline{C}_O(x,s)}{\partial x^2}$$

or

$$\frac{\partial^2 \overline{C}_O(x,s)}{\partial x^2} - \frac{s}{D}\overline{C}_O(x,s) = -\frac{C_O^*}{D} \qquad (B.3)$$

Solution of the equation (B.3) with the transformed boundary condition can be written as,

$$\overline{C}_O(x,s) = \frac{C_O^*}{s} + A(s)\, e^{-\sqrt{\frac{s}{D}}\,x} \qquad (B.4)$$

Now consider the Fick's first low,

$$-J_O(x,t) = D\frac{\partial C_O(x,t)}{\partial x} \tag{B.5}$$

where $J_O(x,t)$ is the number of moles) that passes a given location per second per cm^2 of area normal to the axis of diffusion.

Then the current i(t) is given by,

$$\frac{i(t)}{nFA} = -J_O(0,t) = D\left(\frac{\partial C_O(x,t)}{\partial x}\right)_{x=0} \tag{B.6}$$

Laplace transformation of the above equation can write as follows,

$$\bar{i}(t) = nFAD\left(\frac{\partial \bar{C}_O(x,s)}{\partial x}\right)_{x=0} \tag{B.7}$$

By substituting the derivative part from equation (B.4) into equation (B.7) we get,

$$\frac{\bar{i}(t)}{nFAD} = A(s)\left(-\sqrt{\frac{s}{D}}\right) \tag{B.8}$$

then (B.8) into (B.4) give us the following,

$$\bar{C}_O(x,s) = \frac{C_O^*}{s} - \frac{\bar{i}(s)}{[nFAD]^{-1/2}} s^{-1/2} e^{-\sqrt{s/D}\,x} \tag{B.9}$$

at x = 0,

$$\bar{C}_O(x,s) = \frac{C_O^*}{s} - \frac{\bar{i}(s)\, s^{-1/2}}{[nFAD]^{-1/2}} \tag{B.10}$$

Inverse Laplace transform of (B.10) is,

$$C_O(x,t) = C_O^* - [nAF\sqrt{(\pi D)}]^{-1} \int_0^t \frac{i(u)}{(t - u)^{1/2}}\, du \qquad (B.11)$$

Here we have used,

$$L^{-1}\{f(s)\, g(s)\} = \int_0^t F(t - u)\, G(u)\, du$$

with

$$f(s) = \frac{1}{\sqrt{s}}\,,\ g(s) = \bar{i}(s) \text{ and } L^{-1}\left\{\frac{1}{\sqrt{s}}\right\} = \frac{1}{\sqrt{(\pi t)}}\,.$$

If we use the notation, called semi-integral current,

$$I(t) = \frac{1}{\sqrt{\pi}} \int_0^t \frac{i(u)}{(t - u)^{1/2}}\, du$$

then (B.11) takes the form,

$$C_O(0,t) = C_O^* - [nAFD^{1/2}]^{-1}\, I(t) \qquad (B.12)$$

when $C_O(0,t) = 0$, $I(t) = I_l$, is the limiting semi-integral current, which is of the form,

$$I_l = nAFD^{1/2}C_O^* \qquad (B.13)$$

then the equation (B.12) and (B.13) =>

$$C_O(0,t) = \frac{I_l - I(t)}{nAFD^{1/2}} = \left(\frac{I_l - I(t)}{I_l}\right) C_O^{*\cdot 1} \qquad (B.14)$$

From equation (A.13); If we take the cathodic branch and substituting from (B.14) we get,

$$i = \frac{nAFk^0}{C_O^*}\left(\frac{I_l - I(t)}{I_l}\right) f(\eta) \qquad (B.15)$$

If we take the equation (3.5.6) in Ref.[35],

$$i_0 = nAFk^0 C_o^{*(1-\alpha)}$$

with $C = C_O^*$, we get the equation (2.15):

$$i = i_0 C^{\alpha}\left(\frac{I_l - I(t)}{I_l}\right) f(\eta) \qquad (2.15)$$

Appendix (C)

The Warburg Impedance:

Consider the same reaction as in (A.1), Appendix A and two diffusion equations for O and R according to the Fick's second law,

$$\frac{\partial C_O}{\partial t} = D_O \frac{\partial^2 C_O}{\partial z^2} \qquad (C.1)$$

$$\frac{\partial C_R}{\partial t} = D_R \frac{\partial^2 C_R}{\partial z^2} \qquad (C.2)$$

If the species O and R are assumed to diffuse linearly in the direction z perpendicular to the electrode surface, with coefficient D_O and D_R, then the following initial and boundary condition can imposed:

i) Initial condition: the solution is homogeneous before establishing current,

$$t = 0; \quad z \geq 0; \quad C_O = C_O^*; \quad C_R = C_R^*$$

ii) boundary conditions at an infinite distance from the electrode at a sufficiently large distance from the electrode the concentration of the species attain the concentration of the bulk;

$$t \geq 0; \quad z \to \infty; \quad C_O(z,t) \to C_O^*; \quad C_R(z,t) \to C_R^*$$

iii) boundary conditions at the electrode surface; since there is no adsorption, the flux of O and R are the same and equal to the Faradic current because of mass and charge balances (First Fick's low);

$$t \geq 0; \quad z = 0; \quad D_O \frac{\partial C_O(z,t)}{\partial z} = - D_R \frac{\partial C_R(z,t)}{\partial z} = \frac{I_F(t)}{nFA} \tag{C.3}$$

In addition, the current I_F is given by equation (A.10);

$$I_F(t) = nFA[\, k_f C_O(0,t) - k_b C_R(0,t)\,] \tag{C.4}$$

with k_f and k_b given by ;

$$k_f = k_f^0 \exp\left(-\frac{\alpha nFE}{RT}\right)$$

$$k_b = k_b^0 \exp\left(\frac{(1-\alpha)nFE}{RT}\right)$$

Supposing a small perturbation $\Delta E \exp(j\omega t)$ is applied to the system, the corresponding current change $\Delta I_F \exp(j\omega t)$ is obtained by differentiating equation (C.4) and substituting equation (C.1) and (C.2);

$$\frac{\Delta I_F}{nFA} = \frac{-\alpha nF}{RT} k_f \overline{C_O(0)}\, \Delta E + k_f C_O(0) - \frac{(1-\alpha)nF}{RT} k_b \overline{C_R(0)}\, \Delta E - k_b C_R(0) \tag{C.5}$$

$$j\omega \Delta C_j(z) = D_i \frac{\partial^2 C_j(z)}{\partial z^2} \tag{C.6}$$

where ΔC_i is small variation in C_i and i represents the suffices O and R. $\overline{C}_i(z)$ is the concentration of species for dc polarization, such that ,

$$C_i(z,t) = \overline{C_i(z)} + \Delta C_i(z) \exp(j\omega t) \tag{C.7}$$

The solution of the equation (C.6);

$$\Delta C_i(z) = M \exp\left(z\sqrt{\frac{j\omega}{D_i}}\right) + N \exp\left(-z\sqrt{\frac{j\omega}{D_i}}\right) \quad (C.8)$$

where M and N are the integral constant. If we consider the diffusion layer of infinite thickness; M = 0;

Therefore

$$\Delta C_i(z) = N \exp\left(-z\sqrt{\frac{j\omega}{D_i}}\right) \quad (C.9)$$

and by equation (C.3);

$$\Delta I_F(t) = -NnFD_O\sqrt{\frac{j\omega}{D_O}}\exp(j\omega t) = NnFD_R\sqrt{\frac{j\omega}{D_R}}\exp(j\omega t) \quad (C.10)$$

Using (C.9) we can rewrite equation (C.10)

$$\frac{\Delta C_O(0)}{\Delta I_F} = \frac{1}{nFA\sqrt{j\omega D_O}} \quad (C.11)$$

$$\frac{\Delta C_R(0)}{\Delta I_F} = \frac{1}{nFA\sqrt{j\omega D_R}} \quad (C.11)$$

combining equations (C.11), (C.12) and (C.5) we get;

$$\Delta I_F = \frac{1}{R_{ct}}\Delta E - \left(\frac{k_f}{\sqrt{D_O}} + \frac{k_b}{\sqrt{D_R}}\right)\frac{\Delta I_F}{\sqrt{j\omega}} \quad (C.13)$$

where

$$\frac{1}{R_{ct}} = \left(\frac{\partial I_F}{\partial E}\right)_{C_i} = \frac{nF}{RT}(-\alpha k_f\overline{C_O} - (1-\alpha)k_b\overline{C_R})\,nFA$$

is called the charge transfer resistance under non-equilibrium

conditions. For the equilibrium conditions [substituting I_0 from equation A.14]

$$\frac{1}{R_{ct}} = \left(\frac{nF}{RT}\right)\left(\frac{1}{I_0}\right) \tag{C.14}$$

using the equation (C.14), one obtains the impedance

$$Z(\omega) = \frac{\Delta E}{\Delta I_F} = R_{ct}\left(1 + \frac{\lambda}{\sqrt{j\omega}}\right) \tag{C.15}$$

where

$$\lambda = \frac{k_f}{\sqrt{D_O}} + \frac{k_b}{\sqrt{D_R}} \tag{C.16}$$

In equation (C.15), $R_{ct}\lambda/\sqrt{j\omega}$ is usually called the Warburg impedance. It can be seen that the high frequency limit of $Z(\omega)$ is equal to R_{ct}.

References.

1. B. B. Mandelbrot, "Fractal: Form, Chance, and Dimension.": . Freeman, San Francisco (1977).

2. T. Witten and L. M. Sander: Phy. Rev. Lett., 47, 1408 (1981).

3. T. Witten and L. M. Sander: Phy. Rev. B27, 5686 (1983).

4. L. Niemeyer, L. Pietronero and H. J. Weismann: Phy. Rev. Lett., 52, 1033, (1984).

5. J. Nittmann, G. Daccord and H.E. Stanley: Nature 314, 141 (1985).

6. J. O'M Bockris and A. Diamjanovic in "Modern Aspect of Electrochemistry", vol 3, pg 224, ed. by Bockris and Conway.

7. Wranglen: Electrochim. Acta. 2, 130 (1960).

8. J. P. Eakmann, P. Meakin, I. Procaccia, R. Zeilak: Phy. Rve. A30, 3185 (1989).

9. R. M. Brady and R. C. Ball: Nature, 309, 225 (1984).

10. M. Matsushita, M. Sano, Y. Hayakawa, H. Honjo and Y. Sawada: Phy. Rev. Lett., 53, 286 (1984).

11. J. H. Kaufman, C. K. Baker, A. I. Nazzal, M. Flickner, O. R. Melroy and A. Kapitulnic: Phy. Rev. Lett., 56, 1932 (1986).

12 Y. Sawada, A. Dougherty and J. P. Gollub: Phy. Rev. Lett., 56, 1260 (1986).

13. D. Grier, E. Ben-Jacob, R. Clarke and L. M. Sander: Phy. Rev. Lett. 56, 1264 (1986).

14. D. Grier, D. A. Kessler and L. M. Sander: Phy. Rev. Lett., 59, 2315 (1987).

15 R. F. Voss: J. Stat. Phy., 36, 61 (1984).

16. R. F. Voss and M. Tomkiewicz: J. Electrochem. Soc., 132, 371(1985).

17. A. Le Mehaute and G. Crepy: Solid State Ionics, 9/10, 17 (1983).

18. H. Liu: Phy. Rev. Lett., 55, 529 (1985).

19. L. Nyikos and T. Pajkossy: Electrochim. Acta., 30, 1533 (1985).

20. B. Sapoval: Solid State Ionics, 23, 253 (1987).

21. T. Pajkossy and L. Nyikos: J. Electrochem. Soc. 133, 2061 (1986).

22. J. B. Bates, Y. T. Chu, W.T. Stribling: Phy. Rev. Lett., 60, 627 (1988).

23. M. Hepel and M. Tomkiewicz: J. Electrochem. Soc., 132, 32 (1985).

24. M. Hepel and M. Tomkiewicz: J. Electrochem. Soc., 133, 468 (1986).

25. M. Hepel and M. Tomkiewicz: J. Electrochem. Soc., 133, 1625(1986)

26. M. Eisenberge in "Power system for electric vehicles", US. Department of Health, Education and Welfare, Cincinnati (1967).

27. P. Baue: "Batteries for space power system" NASA, Washington. D.C., (1968).

28. J. McBreen: J. Electrochem. Soc., 119, 1620 (1972).

29. I. Epelboin, M. Ksouri and R. Wiart: J. Electronal. Chem., 58, 433 (1975) and J. Electrochem. Soc., 122, 1206 (1975).

30. S. P. Poa and C. H. Wu: J. Appl. Electrochem., 8, 427 (1978).

31. M. Eden: Proc. of the fourth Berkeley Symposium on Mathematical Statistics and Probability , ed. by F. Newman (Uni. of California, Berkeley, 1961) vol. 4, 223 (1961).

32. B. B. Mandelbrot: "The Fractal Geometry of Nature", Freeman, San Francisco (1983).

33. S. R. Forrest and T. A. Witten: J. Phy. A. 12, L109 (1979).

34. J. O'M. Bockris and A. R. Despic' in " Physical chemistry and Advanced Treatise", Vol. IX B, ch. 7, Academic Press (1970).

35. See for example: A. J. Bard and L. R. Faulkner, "Electrochemical Methods", Wiley & Sons, New York (1980).

36. M. Tomkiewicz: "Lecture notes at the summer school", Brazil, 1989.

37. E. Warburg: Ann. Phy. Chem., 67, 493 (1899).

38. H. Fricke: Philes. Mag., 14, 310 (1932).

39. K. S. Cole and R. H. Cole: J. Chem. Phys., 9, 341 (1941).

40. P. H. Bottelberghs and G. H. J. Broers: J. Electroanl. Chem., 67, 155 (1976).

41. G. J. Brug, A. L. G. Van Den Eeden, M. Sluyters-Rehbach and J. H. Sluyters: J. Electroanal. Chem. 176, 275 (1984).

42. J. R. MacDonald: "Impedance Spectroscopy", John Wiley, (1987).

43. D. W. Davidson and R. H. Cole: J. Chem. Phys., 19, 1484 (1951).

44. R. de Levie: Electrochemica. Acta., 8, 751 (1963).

45. R. de Levie: Electrochemica. Acta., 10, 113 (1985)

46. R. de Levie: J. Electroanal. Chem., 9, 117 (1965).

47. M. Kramer and M. Tomkiewicz: J. Electrochem. Soc., 131, 1283 (1984).

48. M. Tomkiewicz and B. Aurian-Blajeni: J. Electrochem. Soc., 135, 2743 (1988).

49. T. Kaplan and L. J. Gray: Phys. Rev., B32, 1360 (1985).

50. B. Sapoval, J. -N. Chazalviel and J. Peyriere: Solid State Ionics, 28-30, 1441 (1989).

51. Von Smoluchvski: M.Phys. Z., 17, 557 (1916).

52. Von Smoluchvski: Z. Phys. Chem., 92, 129 (1917).

53. J. M. Deutch and P. Meakin: J. Chem. Phys., 78, 2093 (1983).

54. P. Meakin: Phys. Rev., A27, 694, 1496 (1983).

55. M. Matsushita, Y. Hayakawa and Y. Sawada: Phys. Rev. Lett., 32, 3814 (1985)..

56. M. Takuyama and K. Kawasaki: Phys. . Lett., 100A, 337 (1984).

57. P. Meakin: Phys. Rev., A27, 2616 (1984).

58 P. Meakin: Physica A, pg 1-9, 153 (1988).

59. P. Meakin: Phys. Rev., B , 4207 (1984).

60. Z. Racz and T. Vicsek: Phys. Rev. Lett., 51, 2382 (1983).

61. J. H. Kaufman, O. R. Melroy, F. F. Abraham and A. I. Nazzal: Solid State Commun., 60, 757 (1986).

62. J. H. Kaufman, A. I . Nazzal, O. R. Melroy, and A. Kapitulnik: Phys. Rev. B35, 1881 (1987).

63. P. Meakin, I. Majid, S. Havlin and S. E. Stanley: J. Phys. A17, L975 (1984).

64. P. T. Kissinger and W. R. Heinemann: J. Chem. Ed., 60, 702 (1983).

65. M. Tomkiewicz: J. Electrochem. Soc., 126, 2220 (1979).

66. M. Tomkiewicz in " Semiconductor Liquid-Junction Solar Cells", Proceedings of the Electrochemical Society, 77-392 (1977).

67. B. Aurian-Blajeni, M.Kramer and M. Tomkiewicz: J. Phys. Chem., 91, 600 (1987).

68. P. Ramanlal and L.M. Sander: Phys. Rev. Lett., 54, 1828 (1985).

69. J. McBreen and E. Gannon: J. Electrochem. Soc., 130, 1667 (1983).

70. J. Hendrikx, W. Visscher and E. Barendrech: Electrochim. Acta., 30, 999 (1985).

71. J. S. Langer in "Le Hasard et la Matiere", J. Souletie, Vannimenus and R. Stora Editors, pp 629-711, North Holland Pub., Co., Amsterdam (1987).

72. M. Y. Abyaneh and M. Fleischmann: J. Electronal. Chem., 119, 197 (1981).

73. J. St.-Piere and P. L. Piron: J. Electrochem. Soc., 134, 1685 (1987).

74. L. Hsueh and J. Newman: Ind. Eng. Chem. Funda., 10, 651 (1971).

75. Y. Gefen, A. Ahorony and A. Alexander: Phys. Rev. Lett., 50, 77 (1983).

76. See for example S. Havlin and B. Ben-Avaraham: Adv. in Phys., 36 695 (1987).

77. H. G. E. Hentshal and I Procaccia: Physica(Amsterdam) 8D, 435 (1985).

78. T. C. Halsey, M.H. Jensen, L. P. Kadanoff, I. Procaccia and B. I. Sharaiman: Phy. Rev. A33, 1141 (1986).

79. A. Chabra and R. V. Jensen: Phys. Rev. Lett., 62, 1327 (1989).

80. C. Caprile, A. C. Levi, and L. Liggieri; in "Fractal in Physics", L. Pietronero, E. Tosatti, editors, Elsevier Science, 1986.